学位論文

Study on External-Field-Induced Novel Fabrication Processes of Organic Field-Effect Transistors

（外場印加による有機トランジスタ作製の新規プロセスに関する研究）

平成 27 年 12 月博士（理学）申請

東京大学大学院理学系研究科

化学専攻

小槻 賢志

Abstract

Organic field-effect transistors (OFETs) have attracted much attention for plastic electronics. On the basis of recent development of fabrication techniques, OFETs with high mobility over 10 cm^2/Vs have been reported. Application of external field is a fascinating technique for OFET fabrication. So far, applications of light, electric field, magnetic field and mechanical vibration have been investigated during OFET fabrication processes. If external fields are combined with conventional fabrication techniques, it will be another potential way for OFET fabrication. In this dissertation, I fabricated OFETs with external fields in three kinds of studies.

In the first study, electric field was applied after drop-casting of pentacene solution. I found the pentacene single crystals responded to the electric field. The crystals behaved as if they were positively charged and they could be placed between the FET electrodes under the optimized alternating-current (ac) electric field. In addition to such placement control, this study also proved the possibility of electric-field-induced orientation control of single crystals.

In the second study, electric field was applied on the dioctyl-benzothieno-benzothiophene (C8-BTBT) single crystals during solvent vapor annealing (SVA). In this process, the crystals responded to the field and behaved like negatively charged substances. Unlike the first study where the electric field was applied on the *grown* crystals, the electric field worked on the *growing* crystals. Thus, the C8-BTBT crystals were highly aligned along the field between two electrodes and the fabricated FETs showed good performance.

In the third study, light was irradiated on the C8-BTBT FETs after fabrication. The irradiation was performed in the ambient atmosphere, which improved the field-effect mobility by 4 times up to 10 cm^2/Vs. The investigation on the enhancement condition revealed that this phenomenon occurred only in the case of irradiation in the ambient or oxygen atmospheres.

Application of external field proved a promising way for facile OFET fabrication which is applicable for various kinds of organic semiconductor molecules. These fundamental findings will provide new insights for practical OFET fabrication.

Table of Contents

Chapter 1. General Introduction

1.1 Brief overview of organic field-effect transistor (OFET)

Organic field-effect transistor (OFET), a kind of field-effect transistor consisting of organic semiconductor as shown in Figure 1.1, has attracted much attention since the first fabrication in 1980s.[1–5] Although the initial value of field-effect mobility was as low as 10^{-5} cm^2/Vs, they have been improved further for more than three decades.[6–12] As a result, the excellently high-performance OFETs with field-effect mobility of higher than 10 cm^2/Vs have been reported,[13–28] which exceeds amorphous silicon (α-Si) FETs of 0.1-1 cm^2/Vs and is comparable to poly-crystalline silicon (c-Si) FETs of >10 cm^2/Vs. In recent years, higher-performance OFETs have also been reported on the basis of the electric-field-induced Mott transition[29–33] or superconductive phase transition.[34] OFETs have fascinating possibility for next-generation devices.

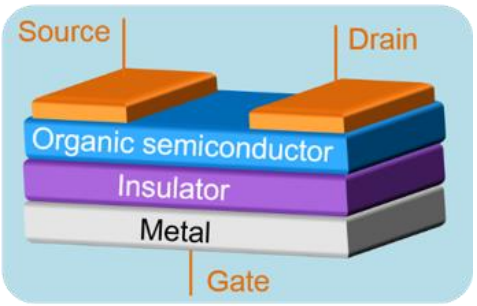

Figure 1.1 Schematic illustration of typical structure of OFET in top-contact/bottom-gate configuration.

As compared with the conventional inorganic FETs, OFETs have various unique characteristics. Among them, major characteristics are their flexibility and lightness. Molecules in an organic crystal condense together not with covalent bonds but with van der Waals bonds. Such van-der-Waals-bonded molecules have room to modulate their distances, realizing the macroscopic flexibility of the crystal. In addition, since organic molecules are mostly composed of light elements such as carbon and hydrogen, the weight of OFET is much smaller than that of inorganic FET. On the basis of these flexibility and lightness, OFETs are expected to be applied for various species of flexible and wearable devices such as flexible displays, wearable sensors, radio-frequency identification (RFID) tags, electronic skins, pressure-/temperature-

/chemical-/bio-sensors and so on.[35–44]

In addition to the above two characteristics, solubility of organic molecules also characterizes OFET from inorganic FET. In the earlier stage of their history, OFETs were mainly fabricated through vacuum deposition. However, this fabrication method was not applicable for low-cost and fast manufacturing. In recent years, on the basis of development of molecular design and synthesis, various kinds of solution-processable organic semiconductor molecules have been reported: soluble oligothiophenes, substituted acenes, alkylated aromatic molecules, and so on. Such development realized solution-processed OFETs and noticed that the solution process was compatible not only with the low-cost and fast fabrication but with the wide-area and high-throughput fabrication. Indeed, the solution-processed high-mobility OFET arrays with higher than 30 cm^2/Vs have been fabricated through ink-jet printing.[18] However, there still remains several requirements to realize practical manufacturing of OFET array. Solution of such requirements is crucial to promote practical OFET application.

1.2 Requirements for practical OFET array

As shown in Figure 1.1, an OFET basically consists of three layers: a gate metal layer, a dielectric layer, and an organic semiconductor layer. Three terminals are connected to these layers: source and drain electrodes connected to the organic semiconductor layer, and a gate electrode connected to the gate metal layer. In this configuration, the organic semiconductor layer works as an active channel and the fabrication of the semiconductor layer is a key step for OFET performance. To fabricate high-performance OFETs, the use of single crystals is preferable for the semiconductor layer. Single crystal has no (or few) grain boundaries, molecular disorders and chemical impurities, which usually disturb the transport of charge carriers. Thus, the absence of them leads to high-mobility OFET. Indeed, most of high-performance OFETs exceeding 10 cm^2/Vs were composed of single crystals or single crystalline films.[13–18,20,22–24] Among these previous reports, it was also achieved to fabricate single-crystal OFETs through solution process for low-cost and manufacturing.[17,18,20,22–24] However, there still remains two major requirements to apply the current solution process for practical manufacturing of single-crystal OFET array.

One requirement is placement control of each single crystal with submillimeter length into a patterned array. In conventional silicon FET, a depletion region is formed around the active channel, which prohibits the cross-talk current between neighboring channels. In OFETs, on the other hand, there is no depletion region around the channel. If a non-patterned array is fabricated on one crystal, there will appear large leak current (Figure 1.2a). This leak current can be suppressed by patterning each crystal into each channel (Figure 1.2b). Thus, precise placement of crystals is essential for practical OFET array.

Another requirement is orientation control of the crystallographic axis of each crystal. In organic semiconductor film, organic molecules laterally stack each other by π-π interactions. As organic semiconductor molecules have anisotropic π-molecular orbitals (Figure 1.3b,c: pentacene molecule), π-π interaction produces an anisotropic

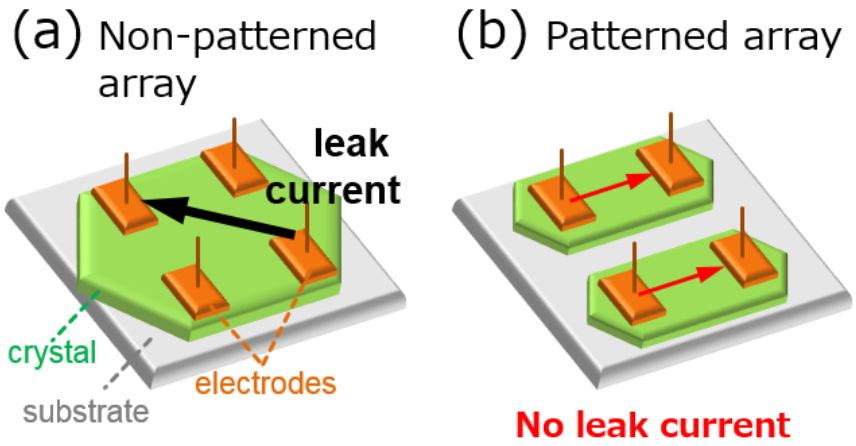

Figure 1.2 (a,b) Schematic illustration of non-patterned array (a) and precisely patterned array (b), showing necessity of patterning for suppression of leak current.

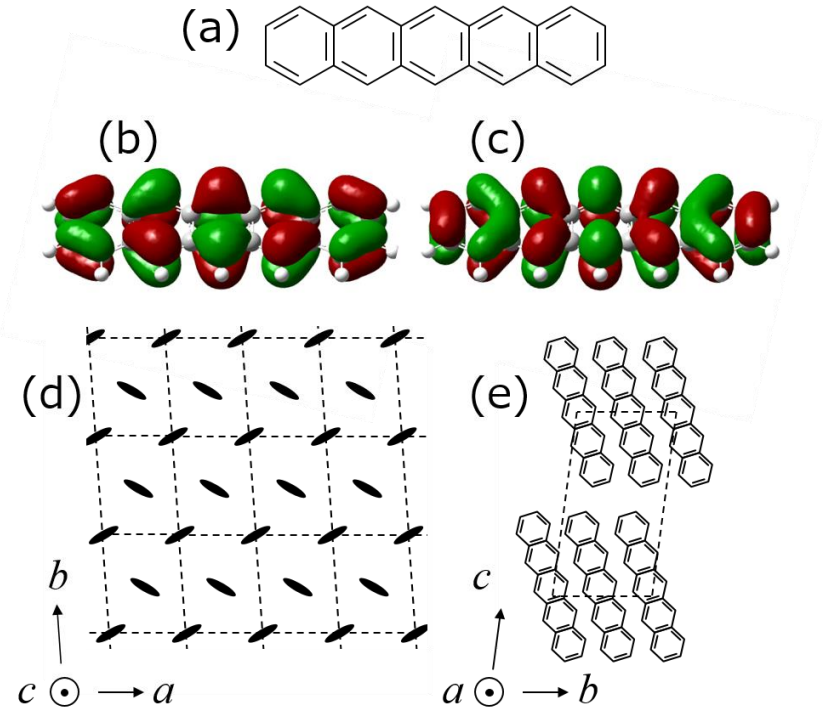

Figure 1.3 Fundamental information on pentacene crystal. (a) Chemical structure of pentacene molecule. (b,c) HOMO (b) and LUMO (c) of pentacene molecule by density functional theory (DFT) calculation (RB3LYP, 6-31G(*d*,*p*)). (d,e) Schematic illustrations of bulk-phase pentacene crystal structure of lateral *a*-*b* plane showing herring-bone arrangement (d), and longitudinal *b*-*c* plane (e).

crystal structure. Most of high-mobility organic semiconductor molecules have an anisotropic herring-bone arrangement in a lateral *a-b* plane (Figure 1.3d: bulk-phase pentacene crystal[45]). In this herring-bone arrangement, carrier mobility also becomes anisotropic. For example, the ratio of maximum mobility to minimum mobility in the angular dependence is two in the rubrene crystal[14] and as large as three in the pentacene crystal.[46] To keep the performance uniform in all devices, the crystallographic axis of each crystal should be aligned to fabricate uniform single-crystal OFET array (Figure 1.4).

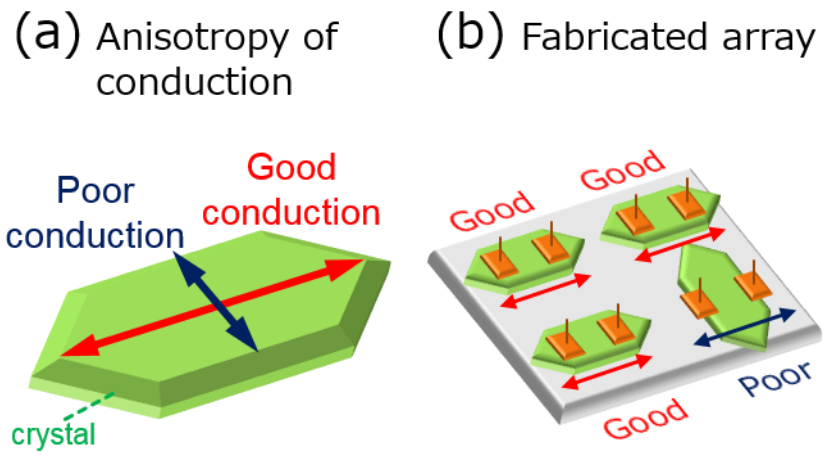

Figure 1.4 (a,b) Schematic illustrations of supposed anisotropy of conduction (a) and supposed performance of non-uniform array (b), showing necessity of orientation control to fabricate uniform-performance OFET array.

So far, many researchers have reported on the placement control[18,47–49] and orientation control[17,20,22,24,48,50–56] of organic single crystals during solution process. Typical fabrication methods are summarized in Figure 1.5. In the placement control, there have been widely performed ink-jet printing, stamp patterning and template-assisted drying (Figure 1.5a). The orientation control were realized during drop-casting, solution-shearing, dip-coating, blade-coating, and so on (Figure 1.5b). In those schemes, however, it is difficult to control the crystal placement and orientation simultaneously. For example, the directional drying method cannot be performed in a submillimeter-scale-patterned narrow regions, while the orientation control cannot be

performed in ink-jet printing. Thus, the fabrication process should be improved to form uniform OFET array.

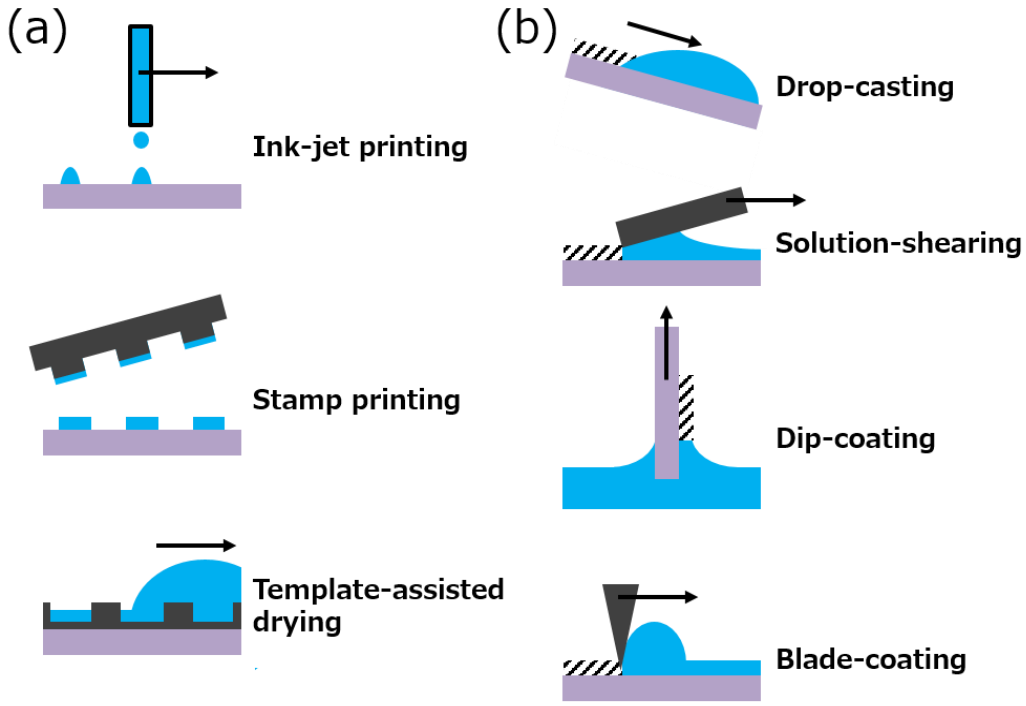

Figure 1.5 (a,b) Schematic illustrations of typical methods for placement control (a) and orientation control (b).

1.3 External-field-assisted OFET fabrication

Application of external field, the main topic of this dissertation, is a fascinating technique for the further improvement of OFET fabrication. It has a possibility to solve the current requirements of the placement and orientation control. So far, it was found effective to apply magnetic field[57,58], electric field[59–63], light[64,65], and mechanical vibration[66] for control of molecular orientation. For example, the electro-magnetic field interacts with the molecular dipole moment of polar molecules such as metal-phthalocyanine, which aligns molecules along the field.[59] Polymorphism control by light irradiation can be performed based on wavelength-dependent light absorption of crystal phase.[65] The mechanical vibration during crystallization induced the transition from a quasi-stable state to the most stable state.[66] If these external fields can be combined with conventional fabrication techniques, it will be another potential way for OFET fabrication.

Recent external-field-assisted OFET fabrication as indicated above has been mainly performed during vapor growth. In vapor growth, however, the interaction between molecules and the underlying substrate is often larger than that between molecules and the external field. In addition, the diffusion length of vapor-deposited molecules is so short (< 10 μm) that the molecules form only small grains. Thus, the effect of external field in vapor growth is too small to produce high-performance FETs with channel length of several tens of micrometers. Application of external field during solution process, on the other hand, seems preferable to control crystal growth in a macroscopic scale. In solution process, the molecules have long diffusion length and the grown crystals can move with support of surrounding solvent. Thus the effect of external field on large crystallite is expected.

Among various phenomena caused by external field in solution, I focused on a dielectrophoretic (DEP) force in Chapter 2 and 3 in this dissertation. The DEP force is known to work on the colloidal suspension by application of electric field and the DEP force attracts the colloids toward the applying electrodes. In the effective dipole moment (EDM) theory, the DEP force is given as follows[67–70]:

$$\langle \vec{F}_{\mathrm{DEP}} \rangle = \Gamma \varepsilon_{\mathrm{m}} \mathrm{Re}\{K_{\mathrm{f}}\} \nabla (\vec{E}^2) \qquad (1\text{-}1)$$

where Γ is a geometric parameter relating to the particle shape and size; ε_{m} is the real part of the dielectric permittivity of the medium; K_{f} is the polarization factor known as the Clausius-Mossotti factor; $\vec{E}$ is the local electric field.

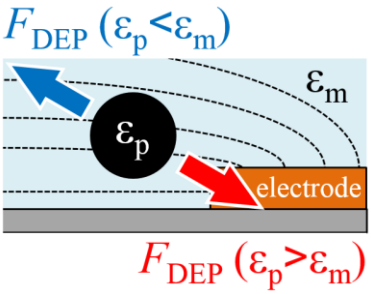

Figure 1.6 Schematic illustration of colloidal solution under electric field.

For a spherical particle with radius *r*, Γ and K_{f} are given as follows:

$$\Gamma = 2\pi r^3 \qquad (1\text{-}2)$$

$$K_{\mathrm{f}} = \frac{\varepsilon^*_{\mathrm{p}} - \varepsilon^*_{\mathrm{m}}}{\varepsilon^*_{\mathrm{p}} + 2\varepsilon^*_{\mathrm{m}}} \qquad (1\text{-}3)$$

where $\varepsilon^*_{\mathrm{p}}$ and $\varepsilon^*_{\mathrm{m}}$ are the complex permittivity of the particle and medium, respectively. When the dielectric constant of the particle is larger (smaller) than that of the medium, the real part of the K_{f} becomes positive (negative) and the DEP force works as an attractive (repulsive) force along the gradient of electric field (Figure 1.6). In the case of inorganic nanowire suspension, the attractive DEP force allows the nanowires to place between the edges of two electrodes where the gradient of electric field is the highest. In addition, the DEP torque, arising from the interaction between the electric-field-induced polarization and electric field, can make the nanowires align parallel to the applying field. As a consequence, the nanowires can bridge the two electrodes.[69,70] In Chapter 2 and 3, I applied this fabrication scheme for OFET fabrication, intending to control the placement and orientation of organic crystals by external electric field.

In addition to the above application of external field *during* OFET fabrication, FET performance can be modulated by the external field *after* fabrication. In this dissertation, I also focused on the light-irradiation-induced modulation of FET performance in Chapter 4. So far, the modulation of current by light irradiation has

been achieved based on photochromism[71–79] or photo-induced charge excitation.[80-88] In photochromism, which means photo-induced molecular isomerization, the current can be modulated by photo-induced doping, improvement of charge-injection efficiency, and change of dielectric capacitance. On the other hand, the modulation without photochromism has been performed by excitation of charge-carriers or excitation of semiconductor/dielectric interfacial traps. In most cases, the photo-induced modulation resulted in threshold-voltage shift or off-current increase in FET performance. However, field-effect mobility, which is a key parameter for OFET performance, has hardly ever been modulated by light irradiation. In Chapter 4, I investigated on the modulation of field-effect mobility of OFETs by light irradiation after fabrication.

1.4 Principal findings in this dissertation

In this dissertation, I chose electric field and light irradiation as external fields, because they are easily controllable fields for facile fabrication process. I investigated on the application of these fields during/after OFET fabrication in the following three kinds of studies.

In the first study (Chapter 2), electric field was applied after drop-casting of pentacene solution. Pentacene is a benchmark organic semiconductor molecule in OFET research.[89] I found the pentacene single crystals responding to the electric field. The crystals behaved as if they were positively charged and they could be placed between the FET electrodes under the optimized alternating-current electric field. This study also proved the possibility of electric-field-induced orientation control of single crystals.

In the second study (Chapter 3), electric field was applied on the dioctyl-benzothieno-benzothiophene (C8-BTBT) single crystals during solvent vapor annealing (SVA). C8-BTBT is known to show high mobility exceeding 1 cm^2/Vs.[90] In this process, the crystals responded to the field and behaved like negatively charged substances. Unlike the first study where the electric field was applied on *grown* crystals, the field in this study was applied on *growing* crystals. The C8-BTBT crystals were highly aligned along the field between two electrodes and the fabricated FETs showed good performance.

In the third study (Chapter 4), light was irradiated on the C8-BTBT FETs after fabrication. The irradiation was performed in the ambient atmosphere and I found that field-effect mobility was improved by 4 times up to 10 cm^2/Vs during the irradiation. The investigation on the device configuration and enhancement condition revealed that this phenomenon occurred only in the case of a pre-annealed C8-BTBT/PMMA double-layered FET in the ambient or oxygen atmospheres.

1.5 Equipment used in this dissertation

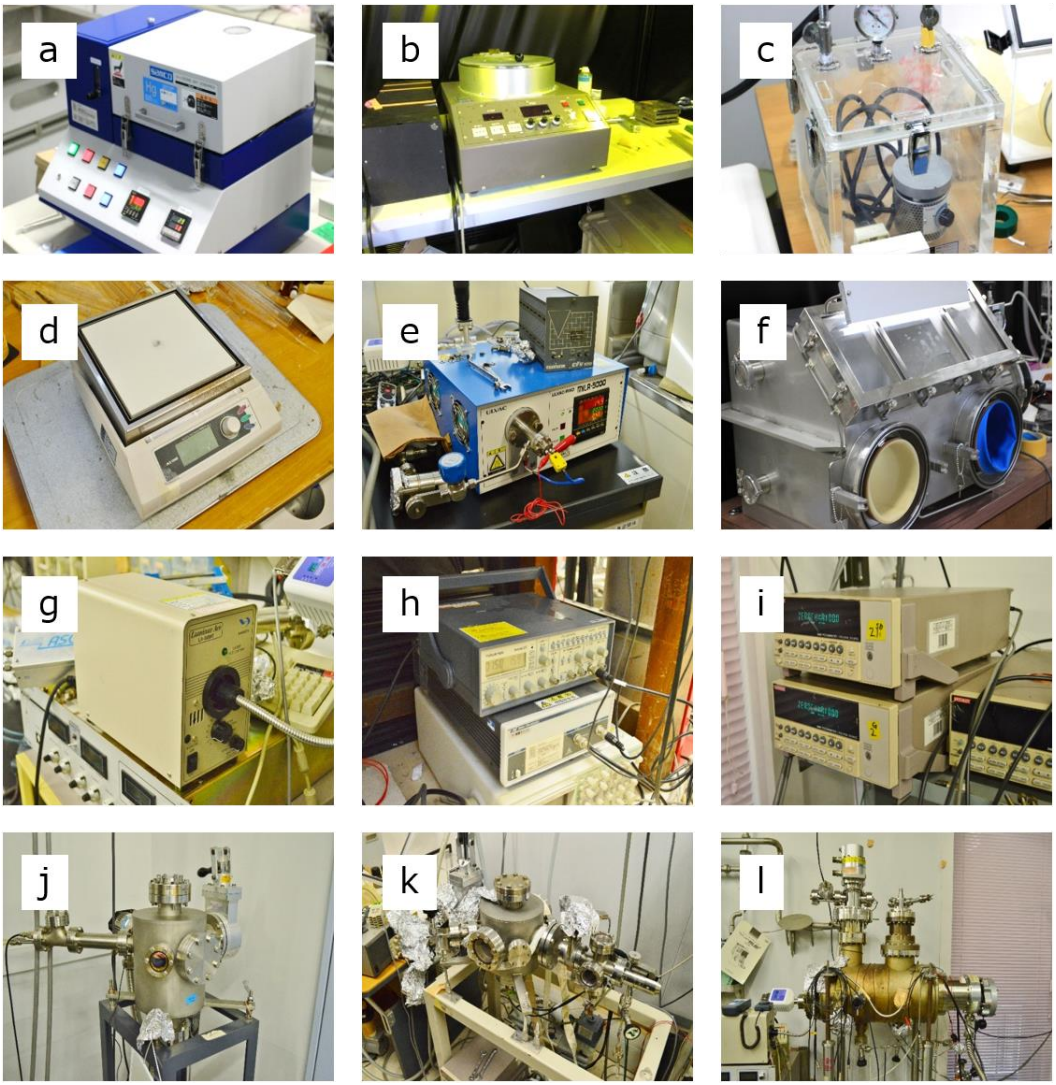

Figure 1.7 Photographs of equipment used in this dissertation: (a) UV/ozonizer (UV-1, Samco); (b) spin-coater (K-359SD-1, Kyowariken); (c) desiccator and heater to reduce GO with hydrazine vapor; (d) hot plate (ND-1, Ninos); (e) heating furnace (MILA-5000HV, Ulvac) to reduce GO; (f) glove box; (g) metal-halide lamp (LA-80MT, Hayashi Watch-Works); (h) function generator (model 25, Wavetek: upper) and amplifier (9100-15-G, Tabor Electronics: lower); (i) a couple of picoammeter/voltage sources (model 6487, Keythley); (j) vacuum chamber to deposit gold electrodes; (k,l) vacuum chambers for FET measurement.

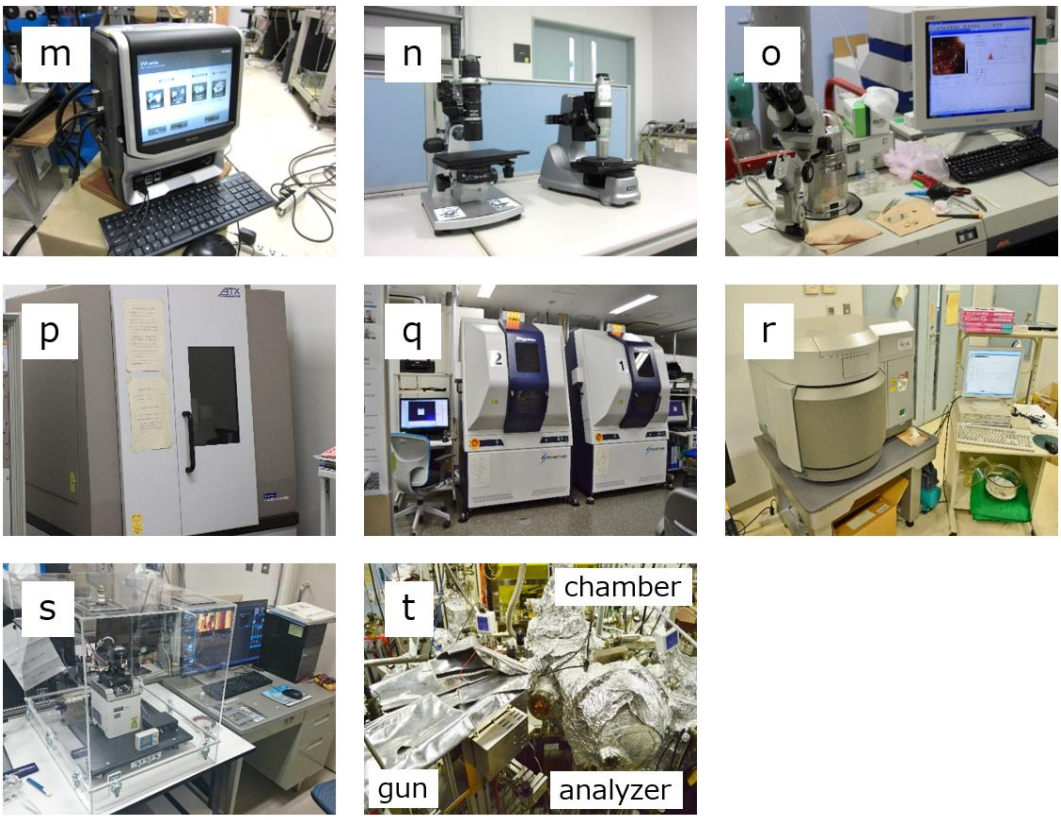

(m) high-speed microscope (high-speed camera and microscope) (VW-9000, Keyence); (n) optical lenses of ×50-500 (VH-Z50L, Keyence: left) and ×500-5000 (VH-Z500R, Keyence: right), which are combined with high-speed microscope (two polarizers can be inserted into these lenses for polarized optical microscopy); (o) atomic force microscopy (JSPM-4210, JEOL); (p) X-ray diffractometer in Terashima lab. in the Univ. of Tokyo (ATX-G, Rigaku); (q) X-ray diffractometers in AIMR in Tohoku Univ. (SmartLab 9MTP, Rigaku: right; SmartLab 9KAB, Rigaku: left); (r) Micro-Raman-spectrometer (NRS-3000, Jasco); (s) Kelvin-probe force microscopy in Ueno lab. in Saitama Univ. (AFM5100N, Hitachi); (t) ultra-violet photoelectron spectroscopy measurement system.

Chapter 2.
Application of Electric Field after Drop-Casting

2.1 Introduction

In this chapter, external electric field was applied after drop-casting of pentacene solution. As mentioned in General Introduction (Chapter 1), application of external electric field for organic semiconductor fabrication have been mainly performed during vacuum deposition. In vapor growth, an electric field interacts with molecular dipole moment and controls the molecular orientation. However, the interaction between molecules and the substrate is often larger than that of molecules and electric field, which limited the effects of electric field within small crystallites. To control placement and orientation of crystals in a macroscopic scale, application of electric field during solution process is desirable.

The drop-casting process investigated in this study is one of the most common methods among various solution processes. I investigated on the pentacene single crystals formed via drop-casting and I found that the grown pentacene crystals in solution responded to the electric field. As compared with the inorganic substances, there have been several similar works on the electric-field-assisted assembly.[69,70,91,92] In those reports, the electric field was applied to a colloidal suspension of nanowires and the field induced a dielectrophoretic (DEP) force in the nanowires. The mechanism of DEP force is mentioned in Chapter 1. According to the effective dipole moment (EDM) theory, when the dielectric constant of the particle is larger (smaller) than that of the medium, the real part of Clausius-Mossotti factor becomes positive (negative) and the DEP force acts as attractive (repulsive) force along the gradient of the electric field.[69] In the case of inorganic nanowires, the attractive DEP force made the nanowires place between two electrodes. In addition to such attractive force, a DEP torque, arising from the interaction between the electric-field-induced polarization and electric field, could make the nanowires align parallel to the applying field. As a

consequence, the nanowires could bridge the two electrodes by the external electric field.

In this study, I have fabricated pentacene single-crystal FETs through electric-field-assisted drop-casting process. Pentacene is a benchmark material for OFET. Although there have been many reports on the fabrication of thin films and single crystals of pentacene, there have been no works on the placement and orientation control of pentacene single crystals. I used 1,2,4-trichlorobenzene as solvent which has small dielectric constant and I found that the pentacene single crystals in the solvent hovered and landed on the channel between electrodes with the use of the alternating-current electric field. Furthermore, I also found that the crystals with large aspect ratio (length per width) tended to align parallel to the electric field. FET measurement revealed that this orientation was suitable for the charge transport in pentacene single crystals. Then, a facile top-down solution-processed fabrication of single-crystal OFETs could be achieved by application of external electric field.

2.2 Experimental

The fabrication process is schematically illustrated in Figure 2.1. Firstly, Au or reduced graphene oxide (RGO) electrodes were formed on an SiO_2/Si wafer (*n*-type, the oxide layer has 300 nm thickness). In both cases, the channel length was 50 μm. In the case of Au electrodes, the SiO_2/Si substrate was cleaned by ozone gas at 50 °C for 10 min in a UV/ozonizer (UV-1, Samco). Then, the Au electrodes of 35 nm thickness were formed on the substrate with a mask on through vacuum deposition.

In the case of RGO electrodes, on the other hand, graphene oxide (GO) solution was firstly prepared from graphite powder (supplied from Nippon Graphite Industries and SEC Carbon) through a modified Hummers' method.[93] The prepared GO solution was sonicated for 30 min to crack the GO sheets into small flakes with the size of several micrometers. Then, the SiO_2/Si substrate with a mask on was exposed to ozone gas at 50 °C for 10 min in a UV/ozonizer. During this process, the area covered with the mask remained hydrophobic, while the non-covered area turned hydrophilic. On this substrate, a GO thin film with thickness of about 10 nm was formed by spin-coating of GO solution in methanol at 3000 rpm. This GO film was reduced into reduced graphene oxide (RGO) film by exposure to hydrazine vapor at 100 °C for 1 h in a desiccator and by annealing at 500 °C for 30 min in a heating furnace. The fabricated RGO sheets showed high conductivity of about 10^3 S/m.[94] Finally, this substrate was exposed to ozone gas at 50 °C for 1 min in a UV/ozonizer to turn the channel solvophilic against 1,2,4-trichlorobenzene which was used in the following.

Pentacene solution was drop-cast on this substrate. Pentacene powder is known to be soluble in heated 1,2,4-trichlorobenzene.[95–97] I dispersed pentacene powder (purchased from Sigma-Aldrich and used after purification) in 1,2,4-trichlorobenzene (purchased from Tokyo Chemical Industry Co.) at the concentration of 0.025 wt.% at 200 °C. This solution was prepared under an N_2 atmosphere in a glove box, because pentacene can be easily oxidized into 6,13-pentacenequinone under the ambient atmosphere (Figure 2.1e). This solution was drop-cast on the substrate which was pre-

heated at 130 °C (Figure 2.1a). Immediately after drop-casting, pentacene molecules recrystallized into single crystals at the liquid/vapor interface via rapid cooling. Then the crystals continued to grow for 20 s (Figure 2.1b). After 20 s from drop-casting, electric field was applied through the Au or RGO electrodes (Figure 2.1c). Finally, solvent evaporated in 300 s and formed an FET structure (Figure 2.1d). During this process, the real-time optical microscope observation was performed using a high-speed camera (Figure 2.2m,n).

FET measurement was performed in vacuum of less than 1×10^{-2} Pa at room temperature using a couple of picoammeter/voltage sources (model 6487, Keithley). Source and drain terminals were connected to the Au or RGO electrodes, and a gate terminal was connected to the underlying silicon substrate. Field-effect mobility and threshold voltage were evaluated in the saturation region. In transfer characteristics in the saturation region, the source-drain current $I_{\mathrm{D,sat}}$ and saturation-mobility μ_{sat} are given as follows:

$$I_{\mathrm{D,sat}} = \frac{\mu_{\mathrm{sat}} W \mathrm{C}_i}{2L} (V_{\mathrm{G}} - V_{\mathrm{T}})^2 \tag{2-1}$$

$$\mu_{sat} = \left| \frac{\mathrm{d} I_{\mathrm{D}}^{\frac{1}{2}}}{\mathrm{d} V_{\mathrm{G}}} \right|^2 \frac{2L}{W \mathrm{C}_{\mathrm{i}}} \tag{2-2}$$

where W is the channel width; L is the channel length; $\mathrm{C_i}$ is the capacitance of gate insulator which was evaluated as 11.5 nF/cm^2 from that of SiO_2 capacitance (ε_{SiO2} = 3.9, d = 300 nm); V_{G} is the gate voltage; V_{T} is the threshold voltage. The values of μ_{sat} and V_{T} were extracted by fitting to the above formulas.

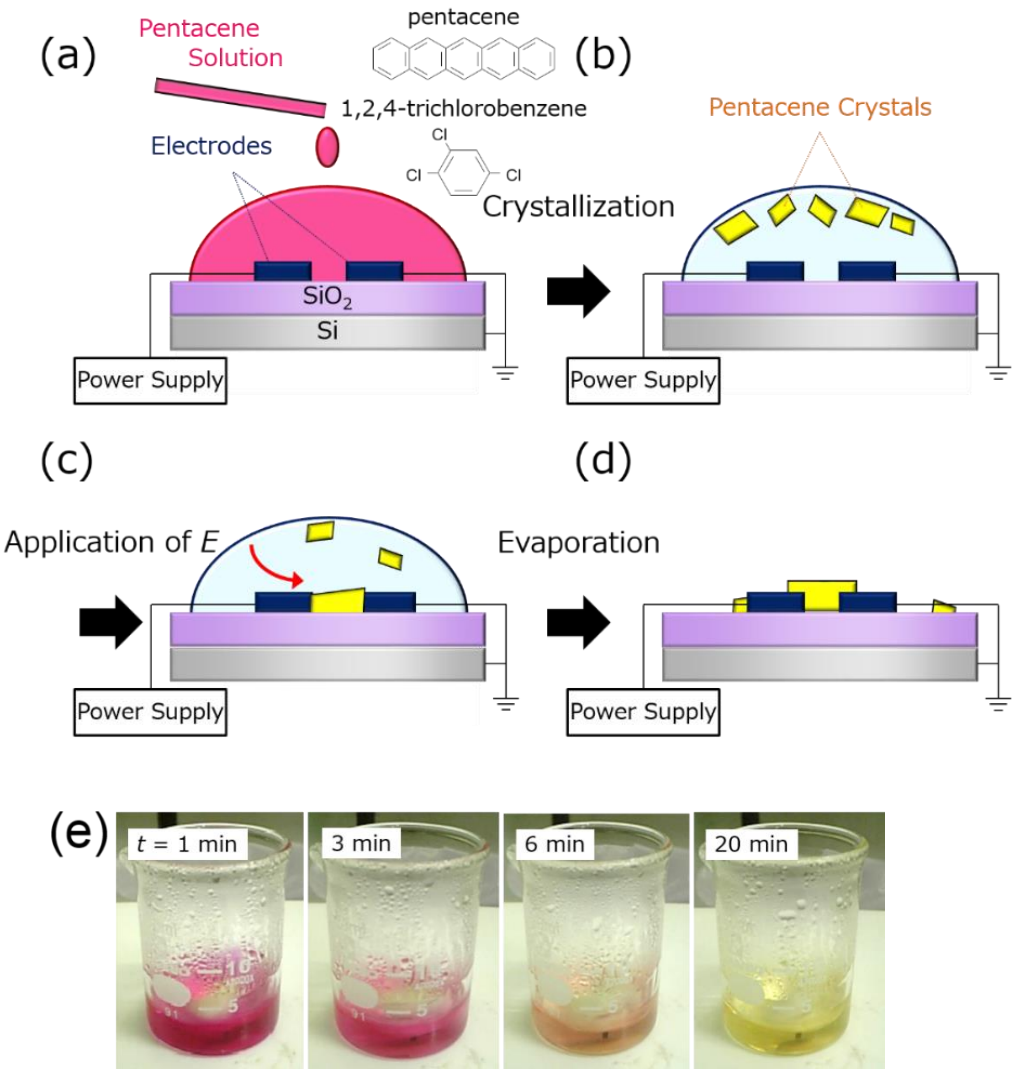

Figure 2.1 (a-d) Schematic illustration of the process. (e) Photographs of pentacene solution heated in the ambient atmosphere, showing oxidization.

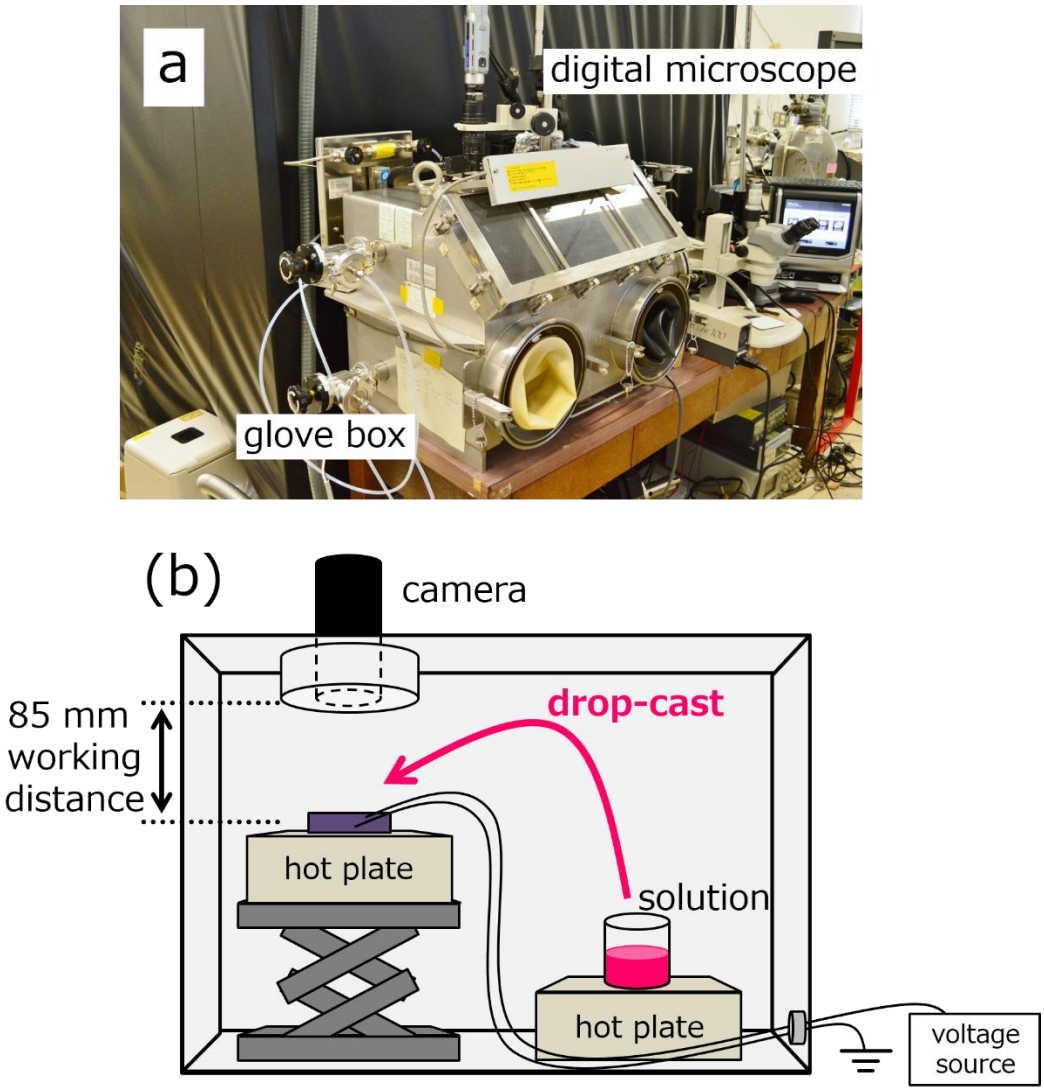

Figure 2.2 (a,b) Photograph (a) and corresponding schematic illustration (b) of real-time observation system in glove box.

2.3 Results and discussion

2.3.1 Pentacene crystal structure

Firstly, crystal structure of pentacene single crystals through the drop-casting process will be discussed. In this study, I developed a new recrystallization process of pentacene single crystals. In previous reports, the pentacene solution which was pre-heated around 200 °C was drop-cast on a substrate which was heated at higher than 180 °C. Then, rapid evaporation occurred and pentacene molecules recrystallized into a thin-film structure at the vapor/liquid/substrate interface, where the evaporation rate of solvent was the largest.[95–97] In this study, on the other hand, the solution at 200 °C was drop-cast on a substrate which was heated at 130-140 °C. Then, the solution was rapidly cooled down and pentacene molecules recrystallized into single-crystal grains at the vapor/liquid interface, where the cooling rate of solution was the largest. Then, temperature of the solution and substrate was optimized as 200 °C and 130 °C, respectively.

Figure 2.3a-e show the typical pentacene single crystals which were grown after recrystallization. As shown in the images, pentacene single crystals of 50-300 μm in lateral length and several hundreds of nanometers in thickness were formed. They had two parallel sides and their apexes of an acute angle were truncated slightly. The acute angle between two sides ranged from 72° to 75°, which was close to that of a bulk-phase crystal (75°) rather than that of a single-crystal-phase crystal (77°).[45] On the basis of a structure of the bulk phase, the longer and shorter sides were ascribed to the (110) and $(\bar{1}10)$ facets, respectively. An example of ascription of crystal axes is shown in Figure 2.3f.

In general, the pentacene crystal is known to have various polymorphs. Typical three kinds of polymorphs are the bulk phase, the single-crystal phase and the thin-film phase.[45] If pentacene crystal is prepared through recrystallization, its polymorph is usually the bulk phase or the single-crystal phase. In general, the phase transition from the bulk phase (high-temperature phase) to the single-crystal phase (low-

temperature phase) is known to occur at 190 °C.[98] On the basis of this fact, recrystallization of the bulk-phase single crystals in this study seemed to occur above 190 °C.

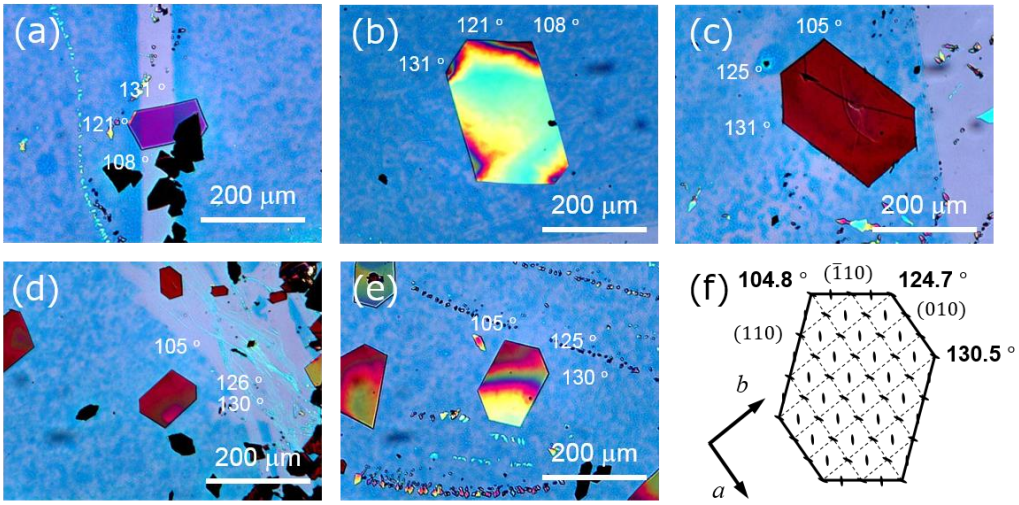

Figure 2.3 (a-e) Typical pentacene crystals grown in this study. (f) Schematic illustration of ascribed bulk-phase crystal structure.

2.3.2 Application of direct-current (dc) electric field

Figure 2.4 shows the results of application of electrostatic direct-current (dc) electric field. When electric field of 1.0×10^5 V/m was applied, a part of the pentacene crystals moved toward the cathode and were captured mainly at the edge of the cathode (Figure 2.4a). The other crystals were not captured at the cathode and dispersed over the substrate. When the electric field strength was increased twice (2.0×10^5 V/m), most of pentacene crystals were captured at the cathode and covered the channel (Figure 2.4b). When the electric field strength was increased up to 1.4×10^6 V/m, the similar capturing and covering features were observed (Figure 2.4c).

The crystal movement from the anode to the cathode indicates the electrophoresis under an electrostatic field. That is, the positive electrification occurs in the inside of the pentacene crystals, although pentacene molecule itself is intrinsically neutral. Such electrification is also known in the case of rubrene crystal surrounded by *m*-xylene solvent.[62] In contact electrification, it is empirically known as Coehn's rule that the intrinsically neutral substances will be charged when they contact with another material which has different dielectric constant.[99] This rule states that the substance with larger dielectric constant will be positively charged, while that with smaller dielectric constant will be negatively charged.[99] In the present case, the dielectric constant of pentacene (4.0)[100] is larger than that of 1,2,4-trichlorobenzene (3.95)[101], which seems to cause positive charge in the pentacene crystals. In addition, the previous report on positive electrification of rubrene crystals ($\varepsilon_{\text{rubrene}}$=2.55-3.12)[102] in *m*-xylene ($\varepsilon_{m\text{-xylene}}$=2.36)[103] could be also explained by the difference of dielectric constants.

In this way, the pentacene crystals responded to the applied external electric field. As these crystals were positively charged in solution, more crystals gathered under the stronger electric field. However, in the present case, these crystals were captured mainly on the cathode and they did not form FET structure under the dc electric field. To place pentacene crystals just between the two electrodes, the

application of an alternating-current (ac) electric field was examined in the following section.

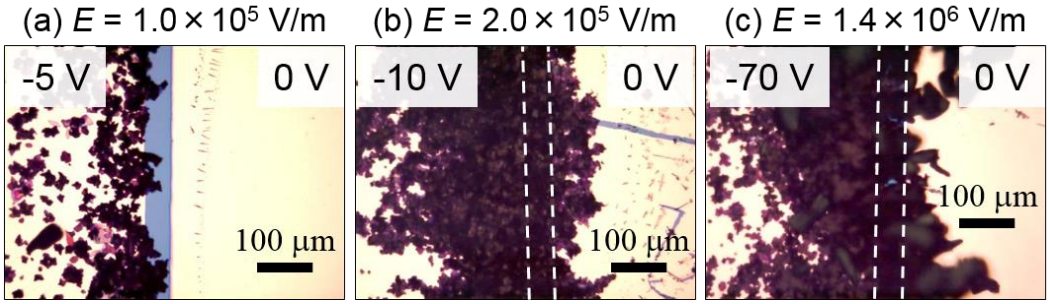

Figure 2.4 Pentacene single crystals captured around the channel under various dc electric fields: 1.0×10^5 V/m (a), 2.0×10^5 V/m (b), and 1.4×10^6 V/m (c). Dashed lines in (b) and (c) indicate the position of electrode edges.

2.3.3 Application of alternating-current (ac) electric field

Figures 2.5 and 2.6 are the sequential polarized optical microscope images under alternating-current (ac) electric field of square wave (6.0×10^5 V/m at 10 Hz in Figure 2.5, 3.0×10^5 V/m at 0.5 Hz in Figure 2.6). Pictures (i)-(iv) in Figure 2.5 show the movement of a pentacene crystal within 0.2 s (two cycles of the square wave) and those in Figure 2.6 show within 2 s (one cycle). In Figure 2.5, pictures (i) and (iii) show the state at which the moving direction of the pentacene crystal was just reversed to the right, while pictures (ii) and (iv) show that was just reversed to the left. Along the reversal of moving direction, the pentacene crystal rotated slightly, where their color was changed in the polarized optical microscope observation. The similar

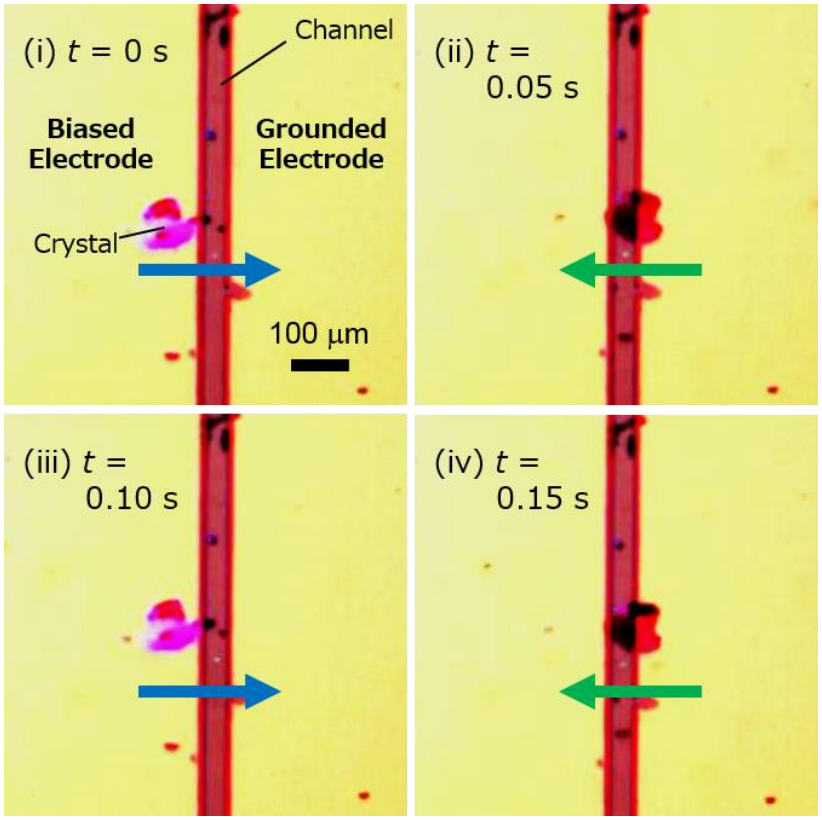

Figure 2.5 Polarized optical microscope images of pentacene single crystal between Au electrodes under ac electric field (6.0×10^5 V/m, 10 Hz) of square wave for 0.2 s. Arrows in each image indicates direction of crystal movement.

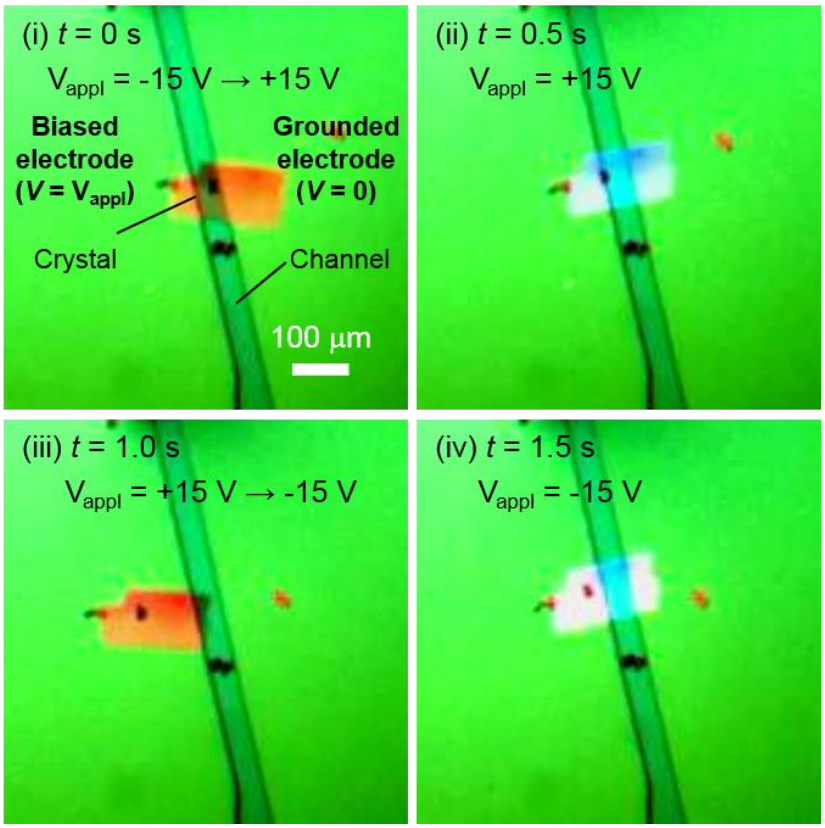

Figure 2.6 Polarized optical microscope images of pentacene single crystal between Au electrodes under ac electric field (3.0×10^5 V/m, 0.5 Hz) of square wave for 2 s.

movement was also shown in Figure 2.6. In these images, uniform color over the crystal and its sensitive response to the crystal direction indicated single crystallinity of pentacene crystals.

As shown in the above images, the pentacene crystals under ac electric field swung between two electrodes. To find the optimal conditions to place the crystal just bridging over the channel, I investigated the dependence of crystal movement on the field strength and frequency. Firstly, the frequency was changed from 1 to 1000 Hz, where the field strength was set at 6.0×10^5 V/m. The swing amplitude was found to become smaller with increasing frequency. At 1000 Hz, crystals could not follow the alternating field probably because of the viscous damping. At 1 Hz, on the other hand, the swing amplitude was so large that the crystals moved over the electrodes' surface.

The crystals could move over the electrode because the solution covers the whole substrate and the electric field also exists on the surface of the electrodes. Throughout this investigation, the medium frequencies of 10-100 Hz were best for crystals to swing mostly on the channel.

Next, the electric field strength was changed from 2.0×10^4 V/m to 6.0×10^5 V/m, where the frequency was set at 10 Hz. In this investigation, the stronger the applied electric field was, the larger the swing amplitude became. Too low electric field could capture few crystals: most of the crystals were still floating in solution and dropped down at the outside of the channel after evaporation. On the other hand, too strong field induced too large amplitude, where the crystals were trapped on the electrode's surface, that is, outside of the channel. The medium electric field was found best for crystals to swing around the channel.

The above results of dependence on various electric field strength and frequency were summarized in Figure 2.7. For the channel length of 50 μm, the electric field strength and frequency were optimized as 1.5×10^5 V/m and 100 Hz, respectively. Under this condition, pentacene single crystals with submillimeter length and submicrometer thickness could be placed between two electrodes automatically in both cases of Au electrodes and RGO electrodes. In the following section, characterization of pentacene crystals was performed after growth under this optimized condition.

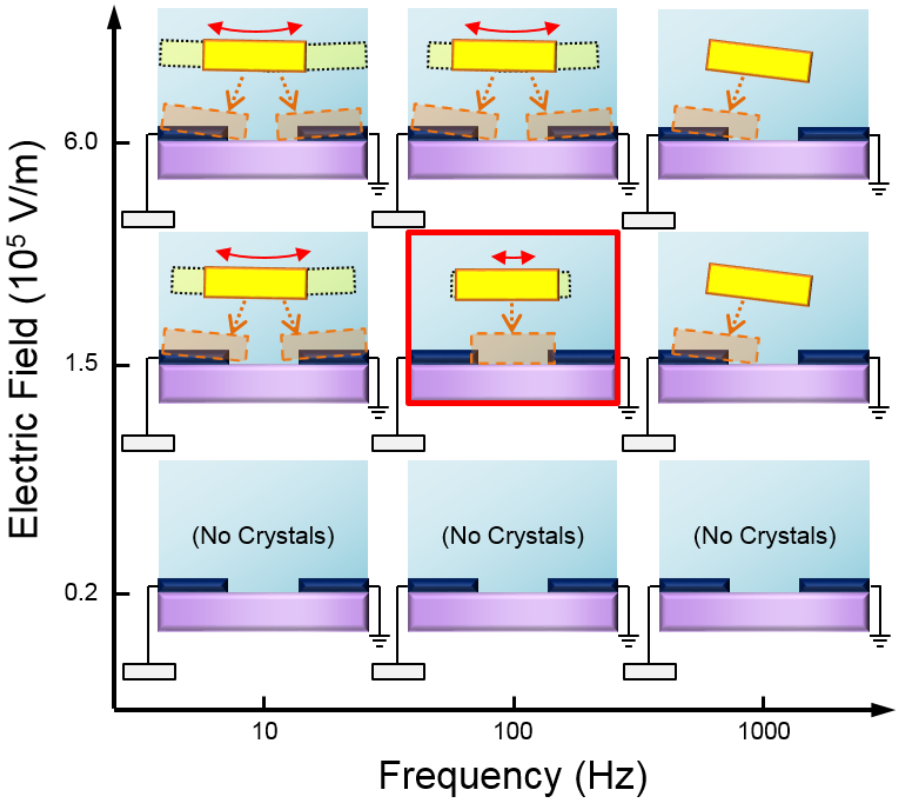

Figure 2.7 Schematic illustration of crystal movement under various electric field and frequency observed in real-time optical microscopy. Red arrows indicate the amplitude of each crystal, and the rectangles surrounded by dashed line indicate the results.

2.3.4 Characterization of crystal orientation

After the crystals could be placed on the channel, I characterized the orientation of these crystals. Figure 2.8a shows an optical image of a typical pentacene single crystal between RGO electrodes. As mentioned in section 2.3.1, the crystal phase could be assigned to the bulk phase. The crystals had two parallel sides, where longer side and shorter side were ascribed to the (110) facet and $(\bar{1}10)$ facet respectively (Figure 2.3f). On the basis of these crystallographic ascription, crystal axes were determined as Figure 2.8b. To analyze the distribution of crystal orientation, I determined orientation angle θ, which was defined as an angle of the $[\bar{1}10]$ axis measured from the electrode edge as shown in Figure 4a. θ was 0° when the $[\bar{1}10]$ axis was parallel to the electrode edge, and θ was 104.8° when the $[110]$ axis was parallel to the electrode edge. In addition to θ, I also determined aspect ratio A, which was defined as the ratio of the length along the (110) facet (longer side) to that along the $(\bar{1}10)$ facet (shorter side) as shown in Figure 2.9. In the case of the crystal in Figure 2.8a, θ was 82° and A was 2.2.

I evaluated θ and A for various pentacene crystals placed on the channel. Figure 2.10 shows the relation between θ and A. For the pentacene crystals with A smaller than 1.5, θ seems to have no relation with A. With increasing A, on the other hand, θ becomes close to 90° and the variation of θ decreases. This result suggested possibility of control of crystal orientation. Such orientation control is known to originate from the DEP torque which has been reported on the alignment of inorganic nanowire[69,70] and rubrene crystal[62]. This DEP torque is caused by the interaction between electric-field-induced dipole moment and electric field. Thus, stronger DEP torque will work on the crystal with larger A, while weaker torque will work on that with smaller A. In the present case, the torque works more effectively for the pentacene crystals with A of larger than 1.5.

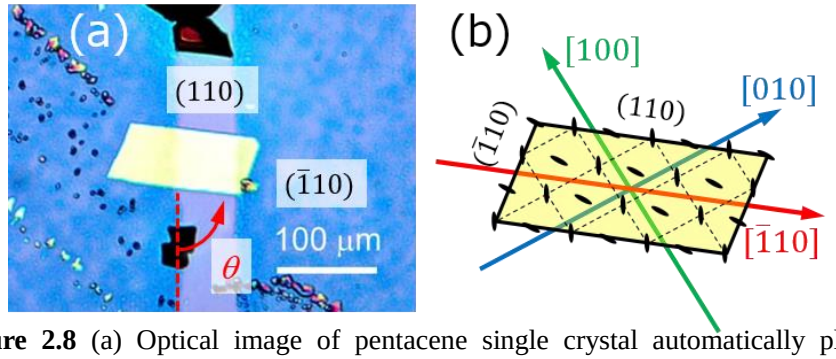

Figure 2.8 (a) Optical image of pentacene single crystal automatically placed between RGO electrodes. (b) Corresponding crystal structure of (a).

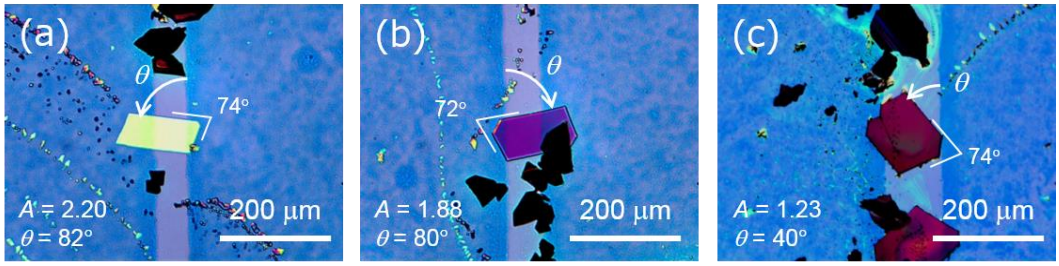

Figure 2.9 (a)-(c) Typical examples of pentacene single crystals captured on the channel. Orientation θ and aspect ratio A are described in each figure. Crystal (a) is same with Figure 2.8a.

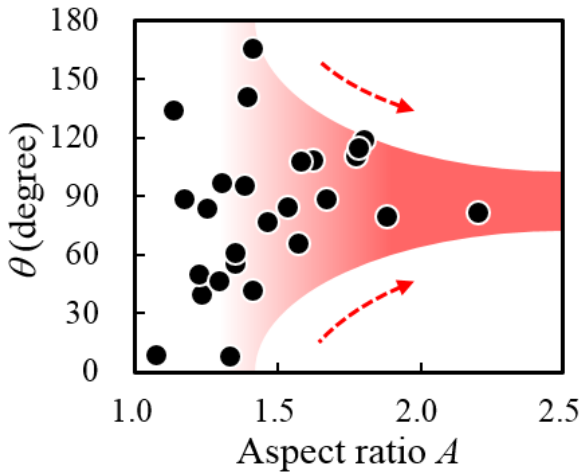

Figure 2.10 Crystallographic orientation of pentacene crystals as a function of aspect ratio A for crystals formed on channel between RGO electrodes. For the pentacene crystals with A larger than 1.5, θ became close to 90° and the variation of θ decreased.

2.3.5 Characterization of FET performance

Finally, the FET performance of the fabricated pentacene crystals will be discussed. As mentioned in section 2.3.3, pentacene single crystals could be captured on the channel at the electric field of 1.5×10^5 V/m and 100 Hz. Under this condition, these crystals kept bridging over the channel after the solvent evaporation. FETs with RGO electrodes showed higher mobility than those with Au electrodes. This improvement of mobility could be ascribed to the good affinity of pentacene to RGO with respect to the charge injection.[104] In the following, the evaluation of FET measurement was performed for the FETs with RGO electrodes.

Typical output characteristic and transfer characteristic were shown in Figure 2.11, which was measured on the device in Figure 2.8a. In the output curve, the absence of nonlinear nature in small V_D region and the high pinch-off voltage seemed to originate from a small contact resistance and a small threshold voltage. Indeed, the threshold voltage was close to zero as shown in the transfer curve in Figure 2.11b. An average threshold voltage of whole devices was as small as -0.8±4.2 V. Field-effect mobility was evaluated in the saturation region. The measured values as a function of orientation angles θ were plotted in Figure 2.12a. Most of the fabricated FETs showed a mobility higher than 0.2 cm^2/Vs, although these FETs were fabricated in a

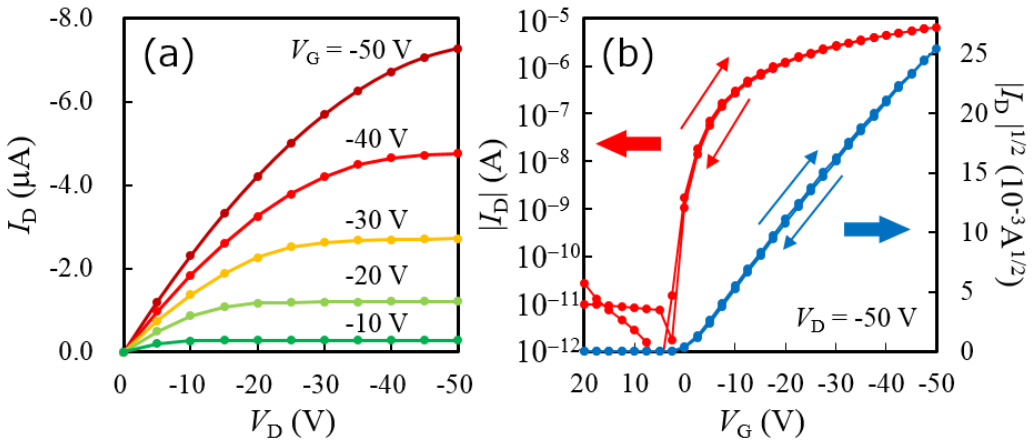

Figure 2.11 Output (a) and transfer (b) characteristics of pentacene single-crystal FET shown in Figure 2.8a.

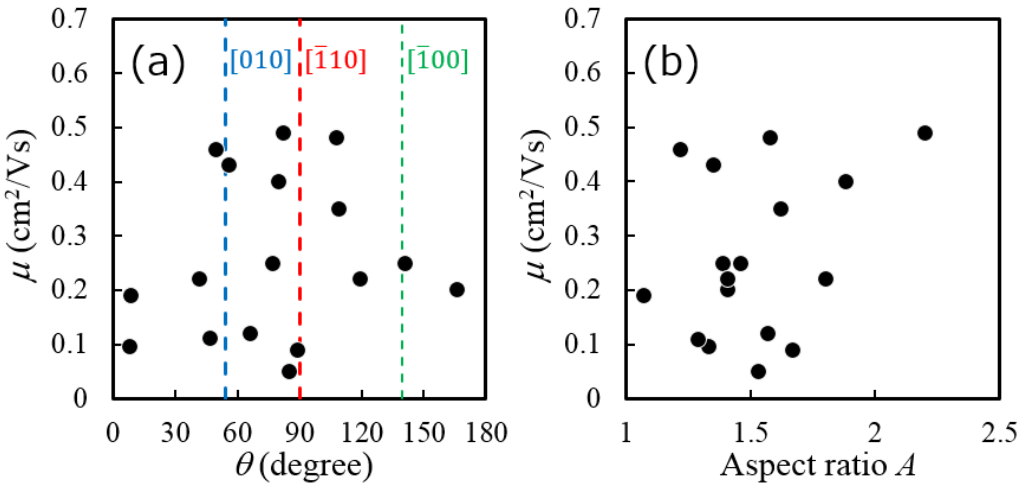

Figure 2.12 (a) Field-effect mobility μ of pentacene FETs as a function of the angle θ. (b) Field-effect mobility μ of pentacene FETs as a function of the angle A.

fast and simple way. Among these FETs, higher mobility was observed at the angles from 50° to 110°, where the conduction direction (perpendicular to the electrode edge) was parallel to the [010] or [$\bar{1}$10] crystallographic axis as the blue and red dashed lines in Figure 2.12a. With respect to the relation of the mobility and aspect ratio A, there seemed to be no dependence (Figure 2.12b), which suggested that the mobility of the crystals were sensitive not to the aspect ratio but to the crystal orientation.

So far, the anisotropy of mobility of pentacene single-crystal FETs has been studied experimentally and threoretically.[46,105,106] Liu *et al.* first observed the mobility anisotropy of a vapor-transported pentacene single crystal, although they did not investigate the relation of anisotropy and crystallographic axes.[13] Soeda *et al.* fabricated single crystals from ionic liquid and observed higher mobility along the [010] axis, while the mobility decreased by an order of magnitude along the [100] axis.[105] Their result was consistent with the present one, where higher mobility was observed along the [010] axis than along the [100] axis (in Figure 2.12a). In addition to this tendency, in the present study, the increase in mobility was also observed from 80° to 108°. Recent first principle calculation showed that the mobility in a pentacene crystal becomes higher around the [$\bar{1}$10] axis.[31] Since the angle

parallel to the $[\bar{1}10]$ axis was ascribed to the 90° in this study, the increase around 90° might be explained in terms of highest coupling of molecular orbitals. However, it is too premature to discuss the anisotropy further, because the apparent anisotropy might be affected by another factor such as the contact between the crystals and electrodes.

Finally, the values of mobility will be mentioned. In the present study, the highest mobility was measured as 0.49 cm^2/Vs. The value is smaller than that of the previous reports (2-5 cm^2/Vs), which were fabricate in vacuum or ionic liquid.[46,105,107] In the case of vapor-transported crystals, the mixing of impurities was suppressed during growth. In ionic-liquid-assisted growth, the impurities would be excluded from the crystals due to the immiscibility of pentacene in fluorine based ionic liquids.[107] On the other hand, in the case of recrystallization from 1,2,-trichlorobenzene solution, the fabricated single crystals is known to have poor mobility.[108] 1,2,4-Trichlorobenzene, which has a high boiling point and good affinity with pentacene, is likely to remain in the crystals. Moreover, in the previous report, pressure was applied to ensure the contact between the crystals and electrodes on a bottom-contact configuration,[46] or an F4-TCNQ layer was inserted between the crystals and electrodes to improve the charge injection.[105] In the present work, the key point was that the position and orientation control of growing pentacene single crystals were achieved by electric field and thus the as-deposited crystals from solution could work as field-effect transistors. There seems to be room to increase of mobility by optimizing the fabrication process, such as removal of the remaining solvent or improvement of the insufficient contact between the crystals and electrodes.

2.4 Conclusion

In this chapter, I achieved the placement and orientation control of pentacene single crystals with the use of an external electric field. In the real-time observation, pentacene single crystals were revealed to respond to the electric field as if they were positively charged in the solution. These crystals could be placed between two electrodes by applying the optimized ac electric field thanks to the dielectrophoresis. In characterization of crystal orientation, the crystals with larger aspect ratio were found more likely to align the $[\bar{1}10]$ crystallographic axis parallel to the applied electric field, which will be suitable from a viewpoint of the mobility anisotropy. Throughout this study, it was found possible to control the position and orientation of organic single crystal by the electric field. This result will lead to high-performance and low-cost industrial manufacturing of single-crystal OFET arrays through solution process.

Chapter 3.
Application of Electric Field during Solvent Vapor Annealing

3.1 Introduction

In Chapter 3, electric field was applied during a solvent vapor annealing (SVA) process. As mentioned in General Introduction (Chapter 1), the application of electric field during solution process is desirable to control crystal growth in a larger scale than the application during vacuum deposition. In Chapter 2, I applied electric field after drop-casting of pentacene solution. In that study, electric field was found to have possibility to align crystals along the electric field. Although it was a simple fabrication process, pentacene molecules had already crystallized before the application of electric field. Then, the obtained pentacene crystals have wide distribution in shapes and sizes. To solve these problems, it is necessary to simultaneously perform the application of field and the crystallization.

Application of electric field during SVA is one possible solution to achieve the above problem. The SVA process is known as a facile process to yield highly crystalline single crystals.[48,60,109–116] In the SVA process, an organic semiconductor film was exposed to solvent vapor. Then, the adsorbed solvent vapor formed a thin solvent layer on its surface.[112] Simultaneously organic semiconductor molecules once dissolves into the solvent layer and recrystallizes into a single-crystal form. Recently, a polymer-assisted solvent vapor annealing (PASVA) process was developed by Liu and Kumatani *et al.*, where the SVA process was performed on the semiconductor/polymer double layer.[48,114,115] They found that the underlying polymer layer could assist molecules' mobility during recrystallization and they fabricated large crystals with the size of several hundred micrometers with high mobility up to 9.1 cm^2/Vs.[114] Through this process, nucleation will occur near the substrate and the electric field will work on the *growing* crystals unlike the *grown* crystals in Chapter 2.

Then, self-assembly of single crystals with uniform size and orientation will be expected.

In this study, I applied electric field to the growing crystals via SVA of dioctyl-benzothienobenzothiophene (C8-BTBT) on poly-(methyl methacrylate) (PMMA). The C8-BTBT single crystals formed via SVA are known to show high field-effect mobility larger than 1 cm^2/Vs.[48,114] I performed the SVA process on an SiO_2/Si substrate on which Au electrodes had been prepared beforehand. Electric field was applied through these electrodes during the SVA process. I performed real-time optical microscope observation and revealed that the electric field could induce the displacement and rotation of the C8-BTBT rod-like crystals. On the basis of these crystal movement, the crystals could bridge over two electrodes.

3.2 Experimental

Two kinds of devices were prepared for the SVA process: PMMA-on-Au configuration and Au-on-PMMA configuration. The schemes of these fabrication processes are schematically illustrated in Figure 3.1b,c. In both configurations, an SiO_2/Si wafer (*n*-type, the oxide layer has 300 nm thickness) was used as a substrate. In the case of PMMA-on-Au configuration, the SiO_2/Si substrate was cleaned by ozone gas at 50 °C for 10 min in a UV/ozonizer (UV-1, Samco). Then, an Au film with 35 nm thickness and 50 μm channel length was deposited through a shadow mask in vacuum. On this substrate, a double layer of 2,7-dioctyl[1]benzothieno[3,2-b][1]benzothiophene (C8-BTBT; Figure 3.1a) and poly-(methylmethacrylate) (PMMA) was formed. C8-BTBT powder was supplied from Nippon Kayaku Co. and PMMA powder was purchased from Tokyo Chemical Industry (M0088; M_w = 13500-14000), and they were dissolved in chlorobenzene with each concentration of 0.5 wt.%. The double layer was automatically formed by spin-coating of this mixed solution at 2000 rpm for 40 s. The difference in surface energy solidifies PMMA faster than C8-BTBT, forming a double-layered structure on the substrate until the completion of spin-coating.[117] Finally, in an SVA process, this substrate was exposed to chloroform vapor in a Petri dish at room temperature for 40 min. During this SVA process, electric field was applied and an *in-situ* real-time optical microscope observation was simultaneously performed (Figure 3.2j,k).

In the case of Au-on-PMMA configuration, Au electrodes were placed between the PMMA and C8-BTBT layer. Firstly, the SiO_2/Si substrate was cleaned by ozone gas at 50 °C for 10 min in a UV/ozonizer. Then, only PMMA layer was formed by spin-coating of PMMA solution in chlorobenzene with concentration of 1.0 wt.% at 2000 rpm for 40 s. On this PMMA layer, Au electrodes with 35 nm thickness and 50 μm channel length were formed by vacuum deposition. Then, a C8-BTBT layer was formed by spin-coating of 1.0 wt.% C8-BTBT solution in toluene at 2000 rpm for 10 s. To prevent PMMA from dissolving, toluene instead of chlorobenzene was used as solvent and the solution was drop-cast during rotation. Finally, the SVA process was

performed by exposing this substrate to chloroform vapor in a Petri dish at room temperature for 60 min. The parameters of the concentration and the SVA time were optimized so as to provide C8-BTBT crystal longer than the channel length of 50 μm.

FET measurement of all fabricated devices was performed in vacuum of less than 1×10^{-2} Pa at room temperature using a couple of picoammeter/voltage sources (model 6487, Keithley). In all devices source and drain terminals were connected to the Au electrodes, and a gate terminal was connected to the silicon substrate. Field-effect mobility and threshold voltage were evaluated in the saturation region in the similar way as Chapter 2, where gate insulator capacitance of the Au-on-PMMA configuration was evaluated as 10.7 nF/cm^2 by combining SiO_2 capacitance (ε_{SiO2} = 3.9, d = 300 nm) and PMMA capacitance (ε_{PMMA} = 2.3[118], d = 15 nm (AFM)).

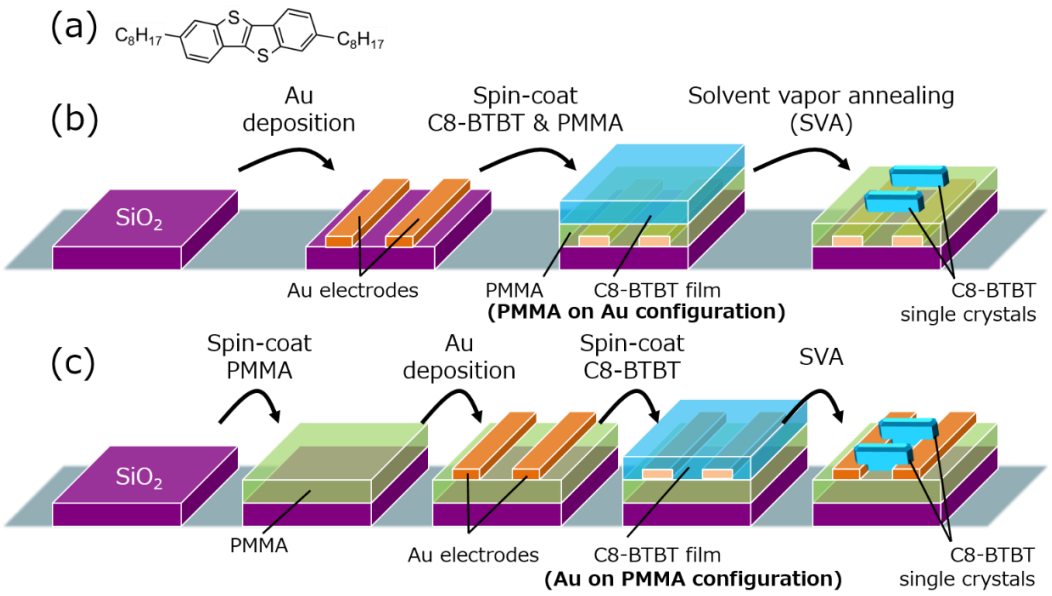

Figure 3.1 (a) Chemical structure of C8-BTBT. (b,c) Schematic illustration of the process on the PMMA-on-Au configuration (b) and Au-on-PMMA configuration (c).

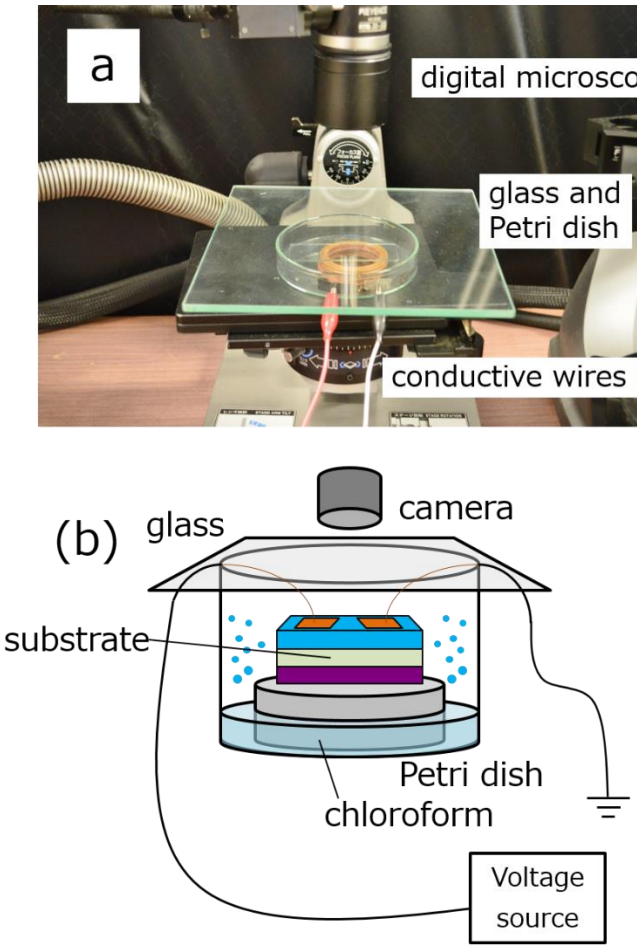

Figure 3.2 (a,b) Photograph (a) and corresponding schematic illustration (b) of real-time observation system during SVA.

3.3 Results and discussion

3.3.1 SVA-processed single crystals

Firstly, a crystal structure of the fabricated C8-BTBT single crystals will be discussed. In solvent vapor annealing (SVA), the double layer of C8-BTBT and PMMA was exposed to saturated chloroform vapor in a Petri dish at room temperature. Then, the PMMA adsorb chloroform vapor on its surface and a thin chloroform liquid layer was formed.[112] C8-BTBT molecules were once dissolved into this liquid layer and recrystallized (Figure 3.3a).[115] During this recrystallization, the PMMA layer assisted C8-BTBT molecules' movement. If there is no PMMA layer, C8-BTBT does not recrystallize into large crystals.[115] In the present work, the SVA process was performed at room temperature and nucleation occurred in 1-2 min. After that, crystal growth via Ostwald ripening started and continued in several tens of hours, in which larger crystals grew further and smaller crystals disappeared.[115]

In the case of the SVA process on C8-BTBT and PMMA, C8-BTBT is known

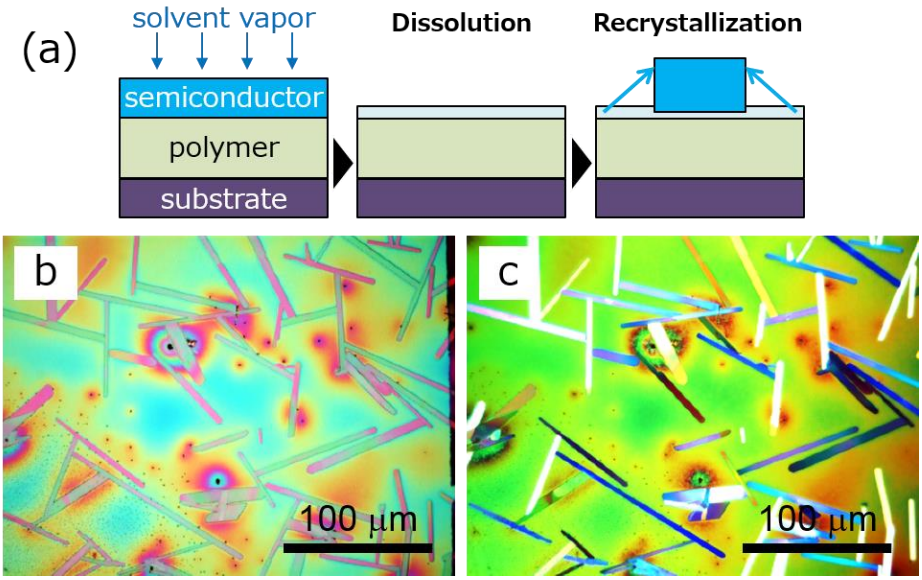

Figure 3.3 (a) Schematic illustration of supposed SVA mechanism. (b,c) Optical (b) and polarized optical (c) images of C8-BTBT single crystals after SVA for 15 h and 20 min, where concentrations of C8-BTBT and PMMA in mixed solution are 1 wt.% and 1 wt.% respectively.

to recrystallize into single crystals with a rod-like shape.[48,114,115] Figure 3.3b,c shows optical microscope (OM) and polarized optical microscope (POM) images of typical C8-BTBT crystals after SVA for 15 h. As shown in the optical image, C8-BTBT formed single crystals with several tens to several hundreds of micrometers in lateral length and several hundreds of nanometers in thickness. In the OM image, the difference of crystal color means that of crystal thickness by interference. In the POM image, on the other hand, the difference of crystal color means that of molecular orientation direction. In Figure 3.3c, crystal colors were uniform within each crystal. In addition, the color of each crystal with the same direction was the same: crystals along a longitudinal direction were bright white-colored, while those along a lateral direction were extinct blue-colored. These results suggested that each crystal was single-crystalline and had the same orientation. Liu and Kumatani *et al.* found these crystal rods were [100]-directed on the basis of an angle of 106° in one end.[48,114] Thus, [100]-directed C8-BTBT single crystals could be fabricated via SVA.

In this study, I also investigated on the SVA processes of C6-BTBT, C10-BTBT and C12-BTBT, where the length of alkyl chains (C6-, C10-, and C12-) was different from C8-BTBT. Figure 3.4 shows optical images of three cases on a PMMA layer after SVA for one night. The shapes and sizes of grown crystals were different in each scheme. In the case of C6-BTBT, there occurred no recrystallization during SVA because of high solubility of C6-BTBT in chloroform. On the other hand, C10-BTBT molecules and C12-BTBT molecules recrystallized into single crystals with several tens of micrometers. Their crystal shapes were different from that of C8-BTBT, reflecting different molecular packing structures of C8-BTBT, C10-BTBT and C12-BTBT. In those cases, however, crystals were too small to bridge over the channel of 50 μm. Therefore, I examined application of electric field only in the case of C8-BTBT in the following section.

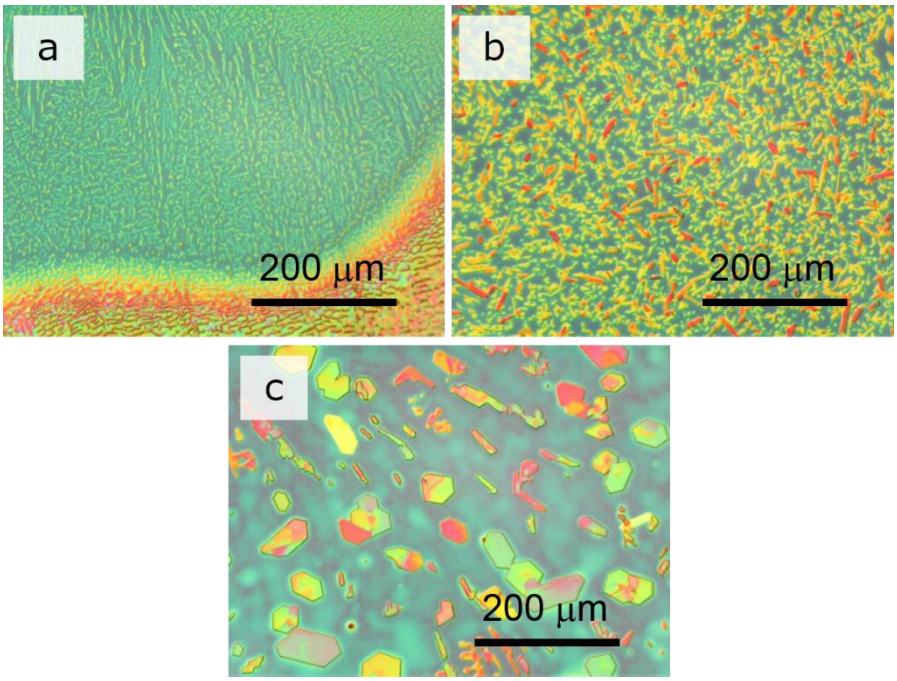

Figure 3.4 Optical images after SVA for one night in three different processes. These films were fabricated before SVA by spin-coating of mixed solution of 1 wt.% C6-BTBT and 1 wt.% PMMA (a), 1 wt.% C10-BTBT and 1 wt.% PMMA (b), and saturated (<1 wt.%) C12-BTBT and 1 wt.% PMMA (c).

3.3.2 Application of electric field on PMMA-on-Au configuration

Next, I will discuss effects of application of electric field on the first configuration: PMMA-on-Au configuration. The schematic illustration and results are summarized in Figure 3.5. In this process, the C8-BTBT/PMMA double layer was fabricated on the substrate on which Au electrodes had been deposited beforehand. Then, this double layer was exposed to saturated chloroform vapor in a Petri dish at room temperature in an SVA procedure (Figure 3.5a). After 40 min many rod-like crystals with a length of about 50 μm were formed via Ostwald ripening as shown in Figure 3.5b. The grown crystals on the channel have longer length than those formed on the electrodes. The large surface energy density of the electrodes attracted a lot of amount of chloroform. Therefore, the concentration of C8-BTBT in a chloroform liquid layer was decreased and the growth on the electrodes decelerated. Figure 3.5c shows the angular distribution of crystal orientation of crystals in the channel as a

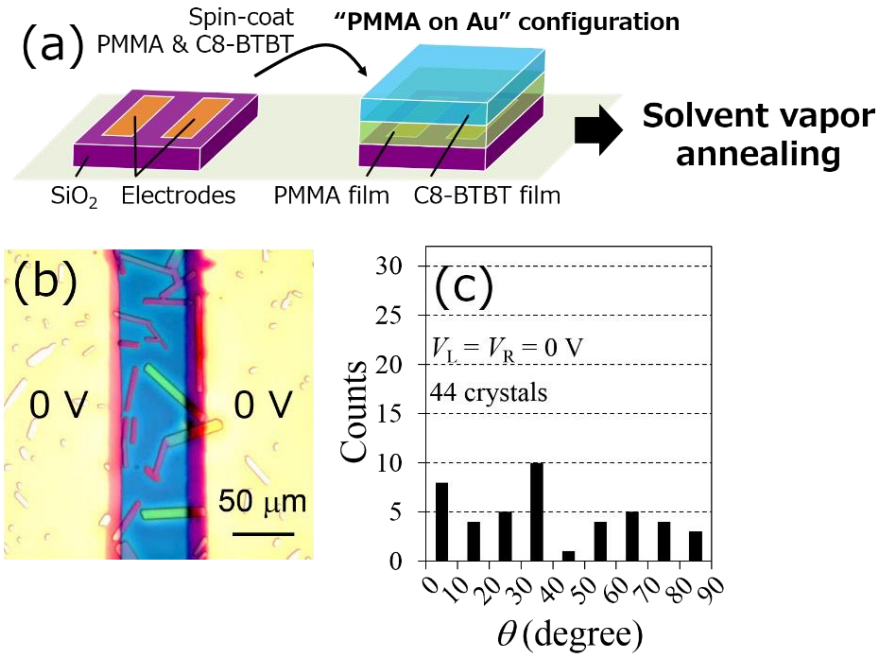

Figure 3.5 (a) Schematic illustration of the PMMA-on-Au configuration process. (b) Optical microscope images of C8-BTBT single crystals after 40 min SVA under no electric field. (c) Distribution of crystal-alignment as a function of θ after 40 min SVA under no electric field.

function of θ, the angle between the C8-BTBT rod-crystal and the electrode edge. On this PMMA-on-Au configuration, the surface of the PMMA layer was smooth between the channel and electrodes, where the topographical steps of electrode's edge had no influence on the crystal orientation. As a result, the histogram for 44 crystals revealed random orientation under the absence of electric field.

On the other hand, in the case of application of dc electric field crystals showed a different behavior. The electric field was applied 3 min after the SVA process started. Figure 3.6 shows the results of application of electric field, where the left and right electrodes were set at -60 V and 0 V so that the direct-current (dc) electric field intensity was 1.2×10^6 V/m (channel length was 50 μm). The electric-field-assisted SVA process was performed for 40 min just like the case of no field. Figure 3.6a was an optical image taken after the completion of the SVA process. The crystals had the same rod-like form as those grown under the absence of electric field. However, crystal orientation in a channel region aligned approximately along the direction of electric field. The polarized microscope image in Figure 3.6b shows the same color of all crystals in the channel. In the histogram shown in Figure 3.6c, more than 70% crystals were revealed to exist in the range of θ from 80° to 90°. This result indicated clearly that the electric field worked on the growing crystals to align their orientation in the

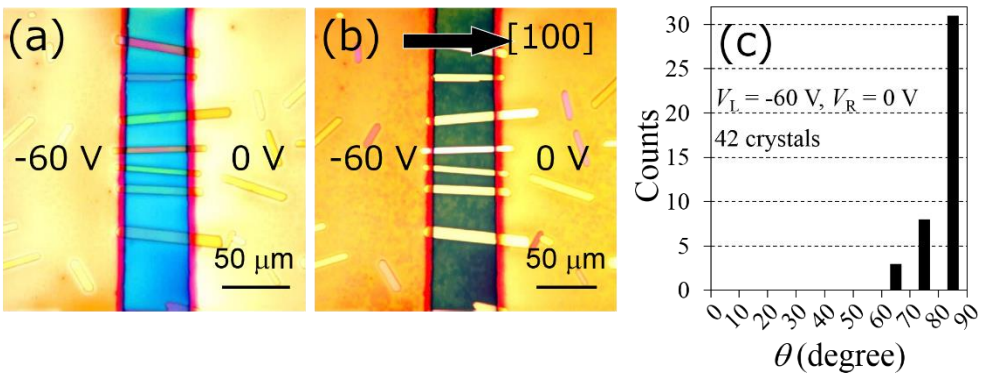

Figure 3.6 (a,b) Optical (a) and polarized optical (b) microscope images of C8-BTBT single crystals after 40 min SVA under 1.2×10^6 V/m dc electric field. (c) Distribution of crystal-alignment as a function of θ after 40 min SVA under 1.2×10^6 V/m dc electric field.

channel.

To elucidate the effect of electric field, we observed the growth process by real-time optical microscopy. Figure 3.7 shows the sequential *in-situ* optical microscope images during the electric-field-assisted SVA process, which were cut from the movie which was recorded during the SVA process under 1.2×10^6 V/m (60 V/50 μm). In 1-2 min after exposing chloroform vapor to the C8-BTBT/PMMA double layer, C8-BTBT nuclei as white dots appeared throughout on the substrate (Figure 3.7a). Electric field was applied 3 min after the SVA process began: the left and right electrodes were set at 0 and +60 V respectively. After the application, the crystals in the channel moved from the cathode (left) to the anode (right) in approximately 30 s (Figure 3.7b). Then the larger crystals grew further and the smaller crystals shrank via Ostwald ripening. During this ripening process, crystals simultaneously rotated their directions along the field (Figure 3.7c-f). In these figures, the color contrast around the crystals means interference fringe of the solvent which was more likely to stick to the larger crystals.

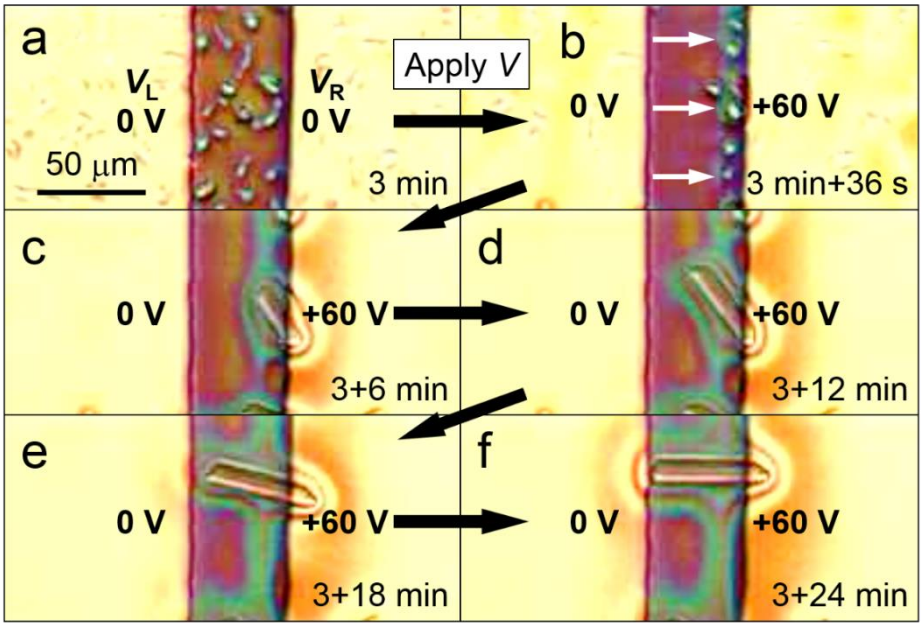

Figure 3.7 *In-situ* optical microscope images during electric-field-assisted SVA process. In initial 3 min, no electric field was applied (a). Then 1.2×10^6 V/m dc field was applied (b-f).

In this way, real-time observation revealed two kinds of effects of electric field: movement from the cathode to the anode (in 30 s) and rotation along the applied field (in 30 min or further). A similar movement was also observed for applied voltages ranging from 30 to 90 V (electric field from 6×10^5 to 18×10^6 V/m; Figure 3.8). Decrease of the applied voltage, however, needed longer time to complete the crystal alignment. Thus the applied voltage was set at 60 V in the following experiment. In this study, I also performed the case of alternating-current (ac) electric field. In that case, C8-BTBT crystals swung between the two electrodes according to the frequency of electric field during the SVA growth. In this process, the longer crystals tended to keep their orientation parallel to the field, while the shorter crystals rotated randomly probably because of the fluid resistance.

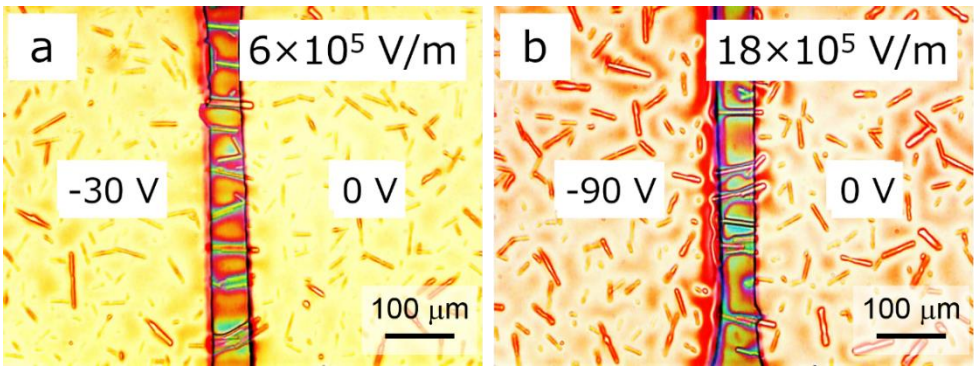

Figure 3.8 *In-situ* optical microscope images of C8-BTBT crystals under electric field of 6×10^5 V/m (a) and 18×10^5 V/m (b).

On the basis of the above results, I will discuss the mechanism of the movement under electric field. The crystals seemed to feel two kinds of forces causing displacement (lateral movement) and rotation.

With respect to the displacement, I observed that the growing crystals moved from the cathode to the anode when the electric field was applied (Figure 3.7a,b). They behaved as if the negatively-charged crystals, although the intrinsic C8-BTBT itself was neutral. As mentioned in Chapter 2, a similar electrification of organic crystals in solution was observed in some kinds of organic crystals such as pentacene (Chapter 2) and rubrene.[62] Such electrification would be explained by contact electrification between substances and surrounding solvent. It is empirically known as Coehn's rule that the intrinsically neutral substances are charged when they contact with another materials, including solvents, with different dielectric constant.[99] This rule states the material with larger (smaller) dielectric constant would be positively (negatively) charged. Although the dielectric constant of C8-BTBT was yet to be reported, those of organic semiconductors (4.0 of pentacene[100] and 4.4 of C_{60}[119]) lie between that of PMMA (2.3)[118] and that of chloroform (4.8)[103]. This fact suggests the negative-charge electrification of C8-BTBT crystals was driven by the interaction between C8-BTBT and chloroform rather than that between C8-BTBT and PMMA.

Next, the rotation of the growing crystals will be discussed. As shown in Figure 3.7b-f, the growing crystals in the channel gradually rotated toward the direction of electric field. Such orientation alignment by electric field has been observed in inorganic nanowires[69,70] and organic crystals.[62,120] In Chapter 2, the degree of orientation of pentacene crystals was revealed to have a strong dependence on their aspect ratio (length ratio of long axis to short one). In that study, the torque effectively worked on the crystals with the aspect ratio rather than 1.5. In the present study, SVA-processed C8-BTBT single crystals grew into a rod shape with the direction of the [100] axis, increasing its aspect ratio up to 10. The large aspect ratio helped much the rotation of crystals toward the direction of electric field.

There seemed to be one assumption that anisotropy of the dielectric constant might also align the crystal orientation. Although the dielectric constant of C8-BTBT has not been known yet, it is expected not to be large from the case of rubrene crystal with a similar herring-bone crystal structure: dielectric constants of 2.55, 2.83 and 3.12 along the *a*, *b* and *c* axis, respectively.[102] Judging from the facts that the degrees of orientation depended strongly on the aspect ratio for the pentacene case and the dielectric-polarization-induced alignment has also been observed in isotropic silicon nanowires[70], the interaction between the electric field and the dielectric polarization was dominantly contributed to the crystal rotation.

The static electrophoresis and the electric-field-induced dipole moment thus contributed to the displacement and rotation of C8-BTBT crystals. On the basis of these two forces, crystals could be aligned and bridged two Au electrodes. These electrodes for the generation of electric field could be also utilized for FET measurement. FET performance of the as-grown crystals were investigated by using these two electrodes as source/ drain electrodes. Figure 3.9 are an output characteristic and a transfer characteristic of grown crystals in the channel, showing a successful FET behavior with applied gate voltage. Thus, single-crystal FETs could be fabricated through the above procedure.

Field-effect mobility on the present PMMA-on-Au configuration was, however, as small as about 0.01 cm^2/Vs. So far, the high mobility of more than 1 cm^2/Vs was already reported in the SVA-grown C8-BTBT crystals along the rod direction. The direction of the grown rods was parallel to the [100] axis of C8-BTBT crystal, which would be good for charge transport. In this study non-ohmic feature in a small-drain-voltage region in the output characteristics suggested a large contact resistance at the C8-BTBT/electrode interface (Figure 3.9a), probably arising from the remaining PMMA layer between the C8-BTBT crystal and the Au electrodes. Therefore, the device configuration should be improved further as the following section.

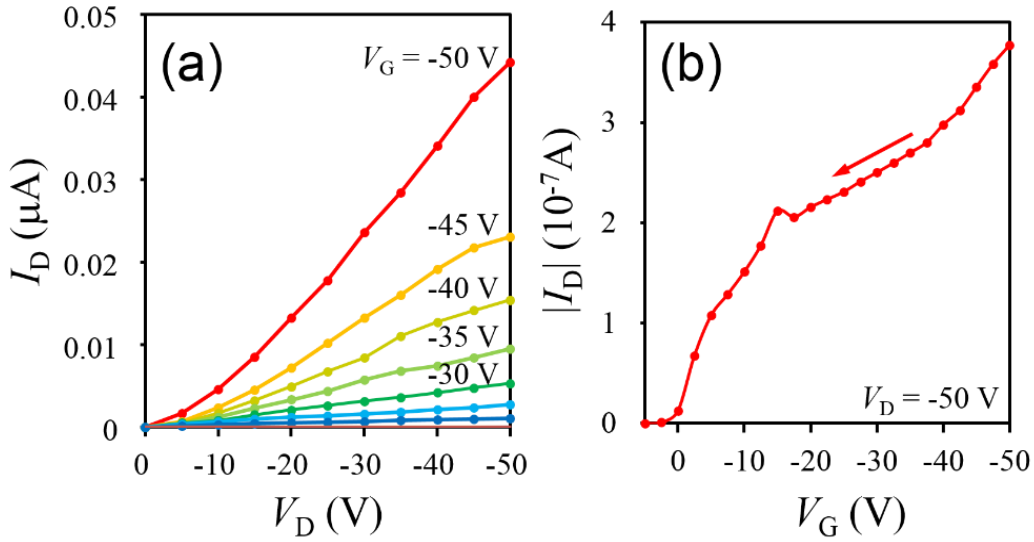

Figure 3.9 Output (a) and transfer (b) characteristics of C8-BTBT single-crystal FET formed on PMMA-on-Au configuration (*W*/*L* is about 3.5).

3.3.3 Application of electric field on Au-on-PMMA configuration

In a PMMA-on-Au configuration, the remaining PMMA layer between C8-BTBT crystals and Au electrodes caused poor charge injection and poor field-effect mobility. To improve the contact between C8-BTBT crystals and Au electrodes, I investigated on another configuration: Au-on-PMMA configuration as shown in Figure 3.10a. In this process, a C8-BTBT layer and a PMMA layer were fabricated separately. PMMA solution in chlorobenzene was firstly spin-coated on an SiO_2/Si substrate. Then, Au electrodes with 35 nm thickness were deposited on it through vacuum deposition. Subsequently, C8-BTBT solution in toluene was spin-coated. Finally, this substrate was exposed to the chloroform vapor at room temperature in the SVA procedure.

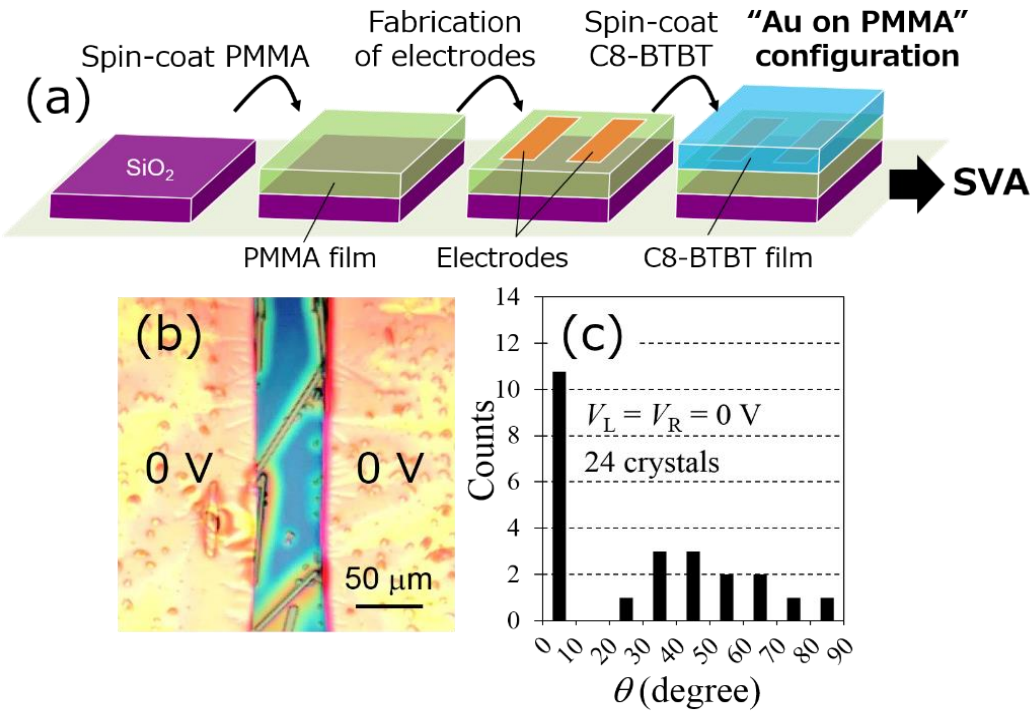

Figure 3.10 (a) Schematic illustration of the Au-on-PMMA configuration process. (b) Optical microscope images of C8-BTBT single crystals after 60 min SVA under no electric field. (c) Distribution of crystal-alignment as a function of θ after 60 min SVA under no electric field.

Figure 3.10b shows an optical image of C8-BTBT crystals in the channel after 60 min SVA under no electric field. Rod-like C8-BTBT crystals were formed only in the channel region, the surface of which was covered with PMMA. On the Au electrodes, on the other hand, nuclei with length of several micrometers once appeared and did not grow further due to the absence of PMMA which could assist the C8-BTBT molecules' self-assembly. The rod-like crystals in the channel tended to grow along the electrode edge. As shown in the histogram in Figure 3.10c, 45% of crystals aligned in the range of θ less than 10°. These results contradict the previous PMMA-on-Au configuration, where the crystals were randomly oriented (Figure 3.5). This difference might be caused by the wettability difference of C8-BTBT between the channel (PMMA) and the electrodes (Au).[48] Besides, the Au electrodes deposited on the PMMA surface worked as a topographical barrier for the growing crystal to ride on. Thus, C8-BTBT crystals longer than the channel length rotated parallel to the electrode edge on the Au-on-PMMA configuration.

Figure 3.11a shows an optical image after 60 min SVA under 1.2×10^6 V/m dc electric field. Under electric field, the growing crystals tended to align along the electric field like those observed on the PMMA-on-Au configuration. The crystals

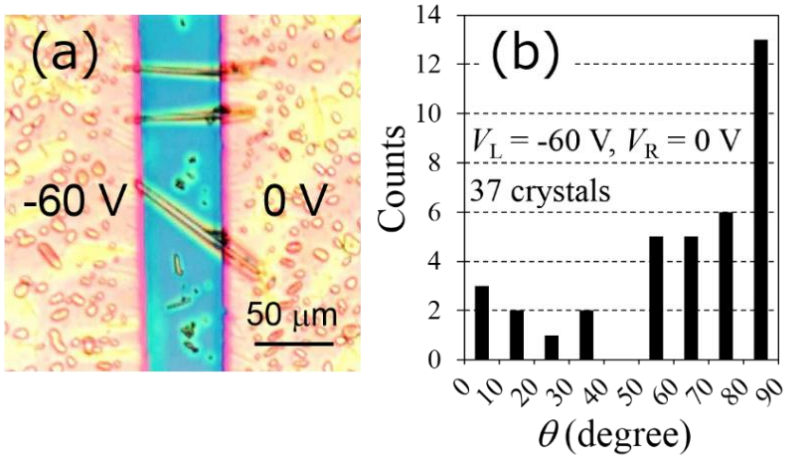

Figure 3.11 (a) Optical microscope images of C8-BTBT single crystals after 60 min SVA under 1.2×10^6 V/m dc electric field. (b) Distribution of crystal-alignment as a function of θ after 60 min SVA under 1.2×10^6 V/m dc electric field.

firstly moved from the cathode to the anode and rotated toward the direction of the field. As shown in the histogram (Figure 3.11b), 35% of crystals were aligned in the region of 80-90°. The degree of alignment was smaller than that on the PMMA-on-Au configuration. As mentioned above, there was a wettability difference and a topographical step at the electrode/channel interface, which prevented some of the crystals from rotating further. Nevertheless, most of crystals successfully rode on the Au electrodes and formed a single-crystal FET structure.

Under the ac electric field on the Au-on-PMMA configuration, however, such FET structure could not be formed. This is because the vibration of crystals between the two electrodes moved the crystals away from the electrode and prevented themselves from riding on the steps at the channel/electrode interface.

Figure 3.12 summarizes FET measurement after the electric-field-assisted SVA on the Au-on-PMMA configuration. As the optical images of three devices in Figure 3.12a-c, C8-BTBT single crystals directly rode on the two Au electrodes and bridged them. FET measurement was performed on each as-grown crystal. In output curves in Figure 3.12 d-f, a good saturated behavior was observed unlike the previous PMMA-on-Au configuration. The calculated values of field-effect mobility and threshold voltage were described in Figure 3.12a-c. The mobility ranged from 0.85 to 1.9 cm^2/Vs and the threshold voltage ranged from -17 to -32 V.

The calculated mobility was as high as around 1 cm^2/Vs, but it was smaller than that reported for the SVA-grown C8-BTBT FETs (average 3.0 cm^2/Vs).[114] In that study, the top-contact Au electrodes were used, which realized good charge injection. In addition, a MoO_3 layer was inserted between C8-BTBT and electrodes to decrease the contact resistance further. In the present study, on the other hand, FET measurement was performed on as-grown crystals and the remaining impurities and PMMA were likely to deteriorate the performance. Indeed, the devices 2 and 3 in Figure 3.12 showed the inferior output characteristics suggesting a large contact resistance. Further study on the modification of the contact might improve the mobility. The key issue of the present study is, however, that the electric-field-assisted SVA process

automatically aligned the C8-BTBT crystal between two electrodes and its mobility exceeded 1 cm^2/Vs without any treatment after the growth process.

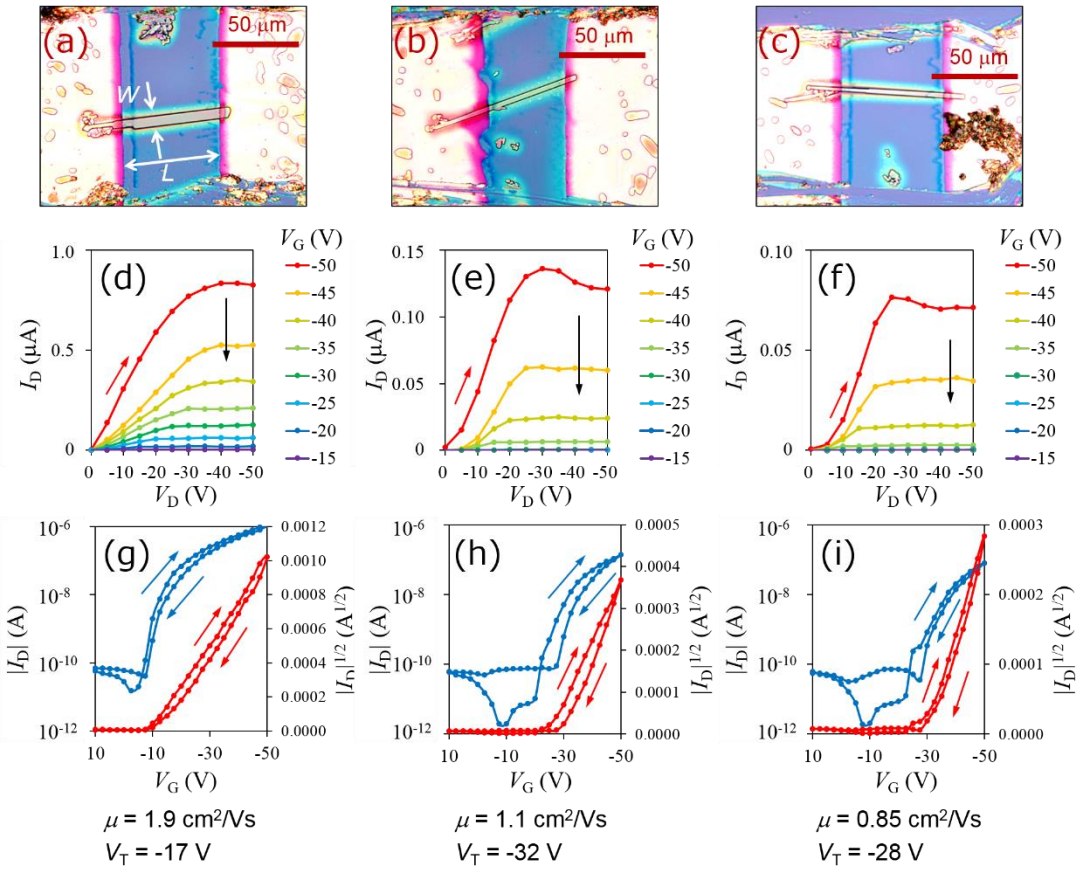

Figure 3.12 FET characteristics of C8-BTBT single-crystal FETs formed on Au-on-PMMA configuration. Optical images (a-c), output curves (d-f) and transfer curves (g-i) of device 1 (a.d.g), device 2 (b,e,h), and device 3 (c,f,i).

3.4 Conclusion

In this chapter, I achieved to control the placement and orientation of C8-BTBT single crystals with the use of an external electric field during SVA. Throughout this study, the SVA-growing crystals responded to the field and behaved like a negatively charged substance. Adjusting the intensity of electric field could place the rod-like crystals just bridging over the two electrodes. On the PMMA-on-Au configuration, the C8-BTBT crystals could be highly aligned according to the electric field, although there remained a PMMA layer between a C8-BTBT crystal and Au electrodes. The large contact resistance could be improved by modification of the configuration as the Au-on-PMMA configuration. On this configuration, the as-grown crystals showed a good FET performance. Application of electric field to SVA thus proved a promising way for facile fabrication of high-mobility C8-BTBT FETs and its array.

Chapter 4. Light Irradiation on C8-BTBT FETs

4.1 Introduction

In Chapter 4, I investigated on an effect of light irradiation as an external field on the performance of dioctyl-benzothienobenzothiophene (C8-BTBT) FETs after fabrication. As compared with other external fields like electro-magnetic field, light irradiation is a simply controllable method, because it can be applied with fine spatial and energetic resolution. So far, the light irradiation was used in various ways for OFET fabrication. For example, morphological change of organic films was observed through photo-excited migration or polymerization of molecules.[121–123] Ichikawa *et al.* observed a uniaxial crystal growth along the desired direction using polarized laser light.[64] Uchida *et al.* observed light-induced crystal crawling by combining two light sources for *cis*/*trans* and *trans*/*cis* isomerizations.[124] In addition, Pithan *et al.* achieved selection of crystal polymorphs by light-induced control of cohesive energy of a certain crystal phase.[65]

In addition to the above methods, light-induced modulation of FET performance after fabrication was also found effective in OFETs. The well-known modulation was based on photochromism, where photo-responsive molecules changed their chemical structure under exposure to light.[125] For example, azobenzene has *cis*/*trans* isomerization, spiropyran has non-ionic/ionic isomerization, and diarylene has open/closed-ring isomerization.[125] In those schemes, the modulation of current was achieved by photo-induced doping, improvement of charge-injection efficiency, and change of dielectric capacitance.[71–79] On the other hand, the modulation of current without such photochromic molecules was also reported by several groups.[80–88] In those studies, the modulation was achieved by excitation of charge-carriers or excitation of semiconductor/dielectric interfacial traps, which resulted in a threshold-voltage shift or an off-current increase.

So far, however, the modulation of intrinsic field-effect mobility has not been

achieved by light irradiation. As the field-effect mobility is a key parameter for its performance, enhancement of mobility would make a great improvement of OFET application. In this study, I investigated on the post-fabrication light-induced mobility enhancement of C8-BTBT FETs. The light was irradiated on FETs on various device configurations in various conditions. Then, the mobility enhancement was observed on the pre-annealed C8-BTBT/PMMA double-layered FETs in the ambient or oxygen atmosphere. Throughout this study, light irradiation was found effective to induce mobility enhancement of OFETs.

4.2 Experimental

The process was schematically illustrated in Figure 4.1. Firstly, the SiO_2/Si substrate (*n*-type, the oxide layer has 300 nm thickness) was cleaned by ozone gas at 50 °C for 10 min in a UV/ozonizer (UV-1, Samco). Then, a double layer of dioctyl-benzothienobenzothiophene (C8-BTBT) (Figure 4.1a) and PMMA (poly-(methyl methacrylate)) was formed in a similar way with Chapter 3. C8-BTBT powder was purchased from Sigma-Aldrich and PMMA powder was purchased from Tokyo Chemical Industry (M0088; M_w = 13500-14000), and they were dissolved in chlorobenzene. The concentration of C8-BTBT was 0.5 wt.% and that of PMMA was 1.0 wt.%. The double layer was automatically formed by spin-coating of this mixed solution at 2000 rpm for 40 s.[117] After that, this substrate was placed on a hotplate which was pre-heated at 130 °C, and it was cooled down by -2 °C/min. During this pre-annealing process, the C8-BTBT film (melting point is about 127 °C) once melted and recrystallized into a thin-film form with large domains of several hundreds of micrometers. Then, Au electrodes with 20 nm thickness was deposited through a shadow mask in vacuum. Finally, a light irradiation process was performed under the ambient atmosphere in a chamber using a metal-halide lamp (LA-80MT, Hayashi Watch-Works Co.,Ltd.). The wavelength of this metal-halide lamp has broad distribution ranging from 380 to 760 nm and sharp strong peaks at 410, 440, 550 and 580 nm (Figure 4.1c). During the irradiation, FET measurement on transfer characteristic was performed at a given interval.

FET measurement of all fabricated devices was performed at room temperature using a couple of picoammeter/voltage sources (model 6487, Keithley). Source and drain terminals were connected to Au electrodes, and a gate terminal was connected to the silicon substrate. Field-effect mobility and threshold voltage were evaluated in the saturation region in the similar way as Chapter 2, where gate insulator capacitance was evaluated as 8.59 nF/cm^2 by combining SiO_2 capacitance (ε_{SiO2} = 3.9, d = 300 nm) and PMMA capacitance (ε_{PMMA} = 2.3[118], d = 60 nm (AFM)). As there appeared large

hysteresis during the forward/backward scan, the mobility and threshold voltage were calculated by taking an average of values which were measured in each scan.

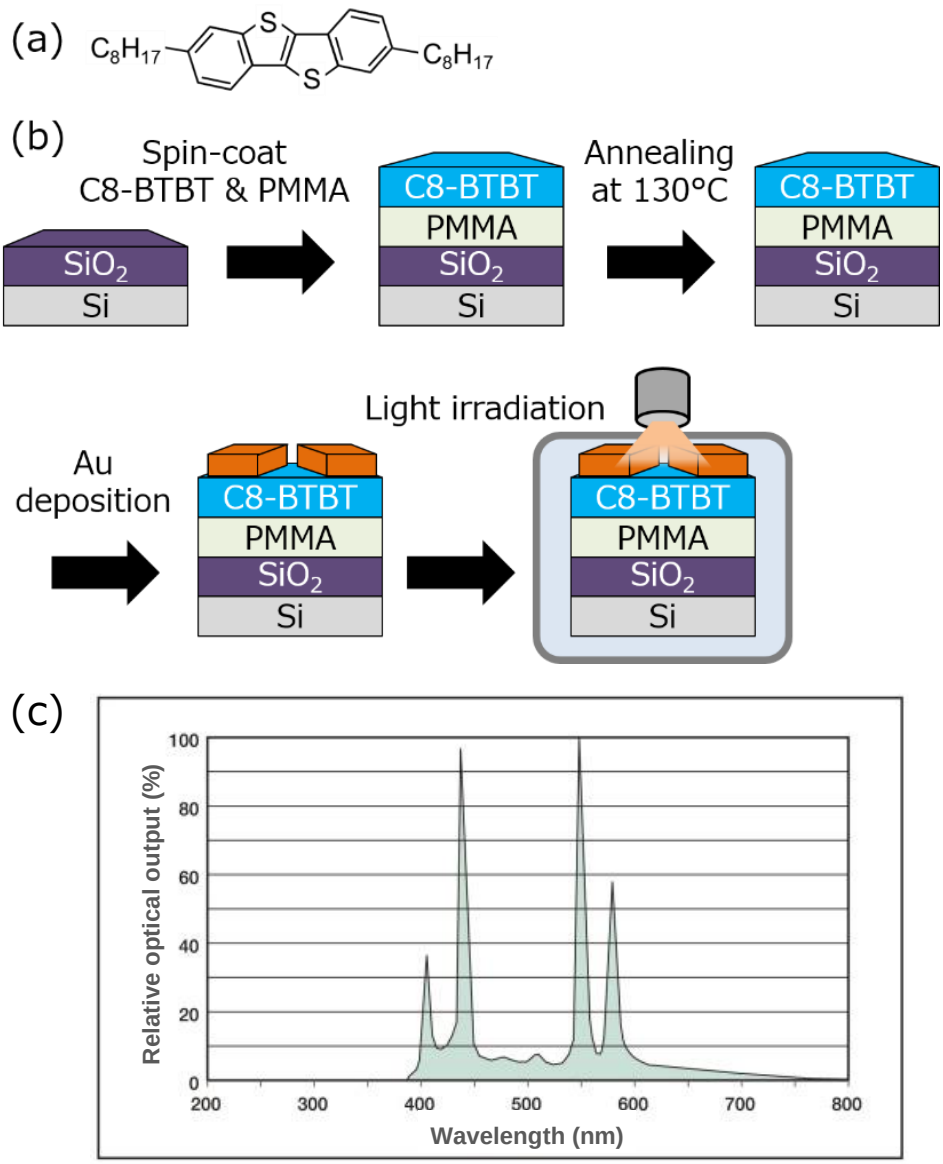

Figure 4.1 (a) Chemical structure of C8-BTBT. (b) Schematic illustration of the process. (c) Optical output spectrum of metal-halide lamp (LA-80MT, Hayashi Watch-Works Co.,Ltd.), reprinted by permission from Hayashi Watch-Works Co.,Ltd.

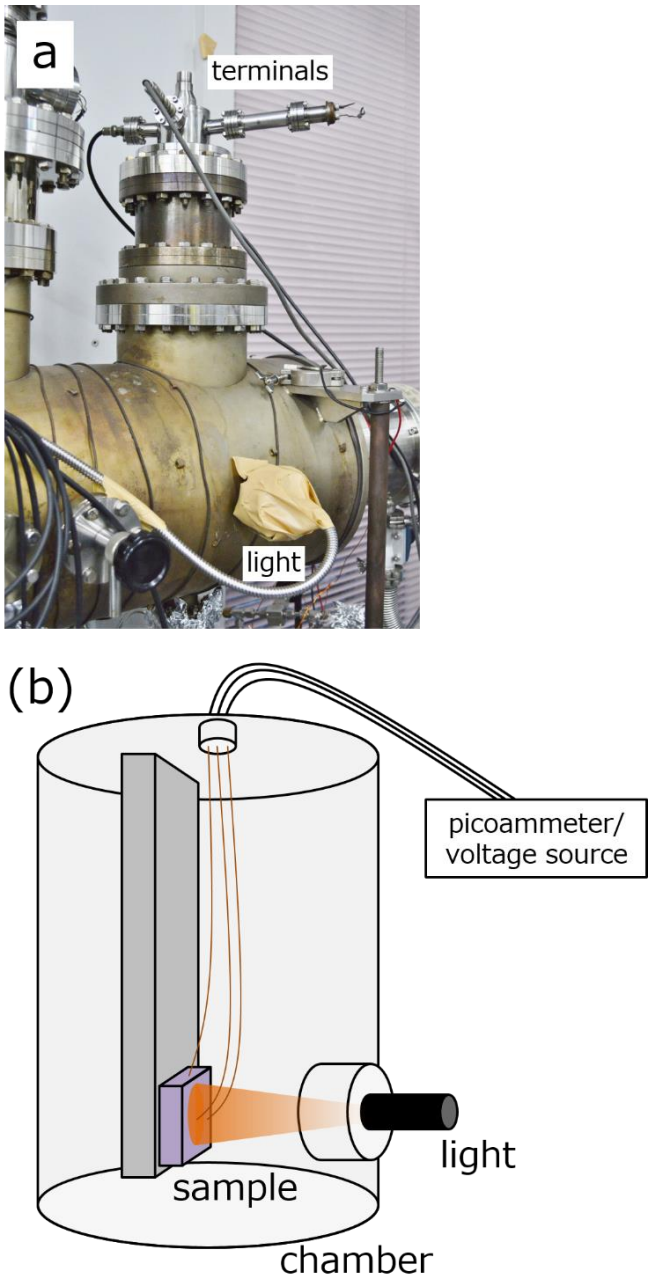

Figure 4.2 (a,b) Photograph (a) and corresponding schematic illustration (b) of light-irradiation system.

4.3 Results and discussion

4.3.1 Effects of pre-annealing

Firstly, effects of pre-annealing of a C8-BTBT/PMMA double layer will be discussed. Figure 4.3 summarizes the polarized optical microscope (POM) images before/after pre-annealing. Before the pre-annealing process, an as-spin-coated film had a polycrystalline structure, where the film was composed of randomly oriented small domains with about ten micrometers (Figure 4.3a). Liu *et al.* found that the difference of surface tensions of C8-BTBT and PMMA induced the formation of double-layered structure where a C8-BTBT layer rode on a PMMA layer.[117] During the formation of this double layer, homogenous nucleation of C8-BTBT occurred everywhere on the surface, resulting in many small grains with random orientations.

When the pre-annealing procedure was performed on this double-layered film, C8-BTBT formed large domains with several hundreds of micrometers. In the pre-annealing process, the C8-BTBT film (melting point is about 127 °C) was annealed at 130 °C. Then, the film once melted in an isotropic liquid phase and recrystallized. During the recrystallization, C8-BTBT molecules were solidified from the edge of the substrate at which the surface temperature is lower than that at the center of the substrate. So far, similar recrystallization processes of C8-BTBT have been performed by several groups.[27,126,127] Especially, intentional control of the solidification direction

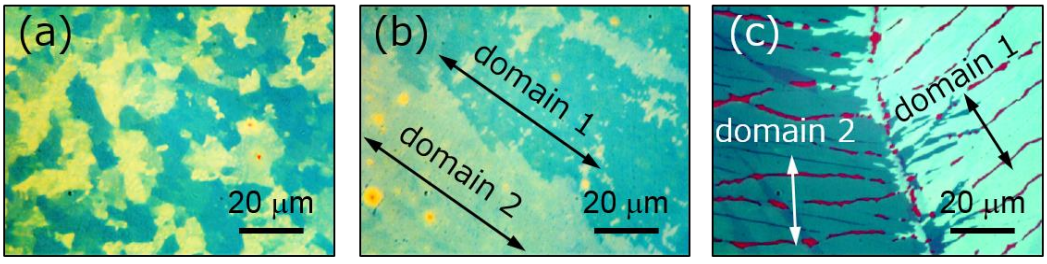

Figure 4.3 Polarized optical images of before (a) and after (b,c) pre-annealing of C8-BTBT/PMMA double layer (a,b) and only C8-BTBT layer (c). Concentrations of C8-BTBT and PMMA in (a,b) are 0.5 wt.% and 1 wt.% respectively, and that of C8-BTBT in (c) is 0.5 wt.%.

was achieved using a temperature gradient on the substrate.[126,127] In those conventional studies, however, the solidification was performed on an SiO_2 substrate without a PMMA layer. As there was a large difference of thermal contraction between C8-BTBT and SiO_2, many cracks were formed during the cooling procedure (Figure 4.3c). These cracks were so deep that they reached the surface of SiO_2 substrate and the calculated field-effect mobility perpendicular to the cracks were very poor. Thus, such cracks should be reduced for practical application.

In this study, to prevent the crack formation in a C8-BTBT film, a PMMA layer was used as a buffer layer to relax the thermal contraction between C8-BTBT and SiO_2. As a result, the size and depth of cracks were drastically reduced after pre-annealing (Figure 4.3b). Figure 4.4 summarizes the effects of pre-annealing on the double layer which was formed by spin-coating of mixed solution of C8-BTBT and PMMA of various concentrations. As shown in this figure, too low concentration of C8-BTBT or

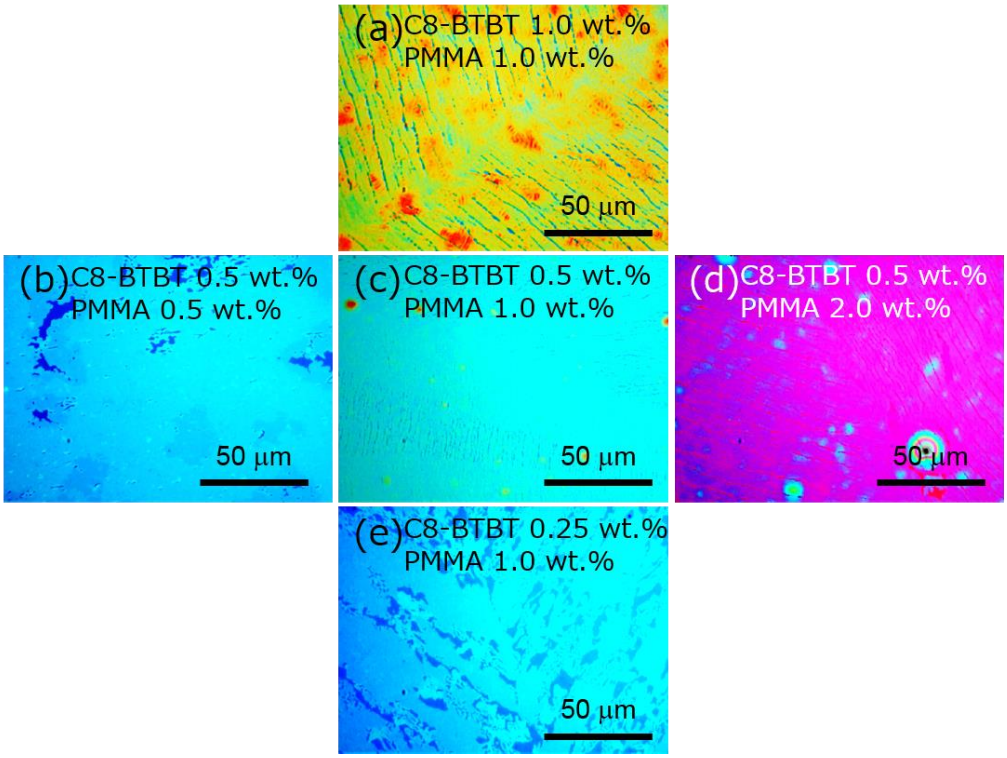

Figure 4.4 Optical images after pre-annealing of C8-BTBT/PMMA double layer which was formed by spin-coating of mixed solution of various concentrations.

PMMA caused aggregation of C8-BTBT film. When the C8-BTBT concentration was decreased to 0.25 wt.%, quantity of C8-BTBT molecules was insufficient for keeping a thin film structure (Figure 4.4e). When the concentration of PMMA was decreased to 0.5 wt.%, C8-BTBT molecules' movement was insufficiently assisted by the PMMA layer during solidification (Figure 4.4b). On the other hand, too much concentration of C8-BTBT or PMMA caused cracks in the pre-annealed C8-BTBT film. In both cases, the relaxation effects of the PMMA layer did not balance with the thermal contraction in the C8-BTBT film. Thus, concentrations of C8-BTBT and PMMA were optimized as 0.5 wt.% and 1.0 wt.% respectively.

Figure 4.5b-d show the results of FET measurement of pre-annealed C8-BTBT/PMMA double-layered film with top-contact Au electrodes. Typical output and transfer characteristics were shown in Figure 4.5b,c and the plots of mobility as a function of threshold mobility were shown in Figure 4.5d. Average field-effect mobility and threshold voltage were calculated as 2.1 ± 0.6 cm^2/Vs and -46 ± 3 V, and maximum mobility was calculated as 3.2 cm^2/Vs. As compared with the case of as-spin-coated film which had mobility of 0.2-0.8 cm^2/Vs, the present mobility was enhanced about four times by pre-annealing. Such mobility enhancement was caused by the expansion of crystalline domains after pre-annealing. The mobility values were almost equal to the conventional case where an only C8-BTBT film without a PMMA layer was annealed on the SiO_2/Si substrate. In my case, however, the values of mobility had small variation compared with the conventional case thanks to the drastic reduction of crack formation in the C8-BTBT film. With respect to the threshold voltage, on the other hand, the calculated values were large. Since the values of threshold voltage were almost equal to that of the as-spin-coated film, these large values were supposed to be caused by charge-traps at the C8-BTBT/PMMA interface.

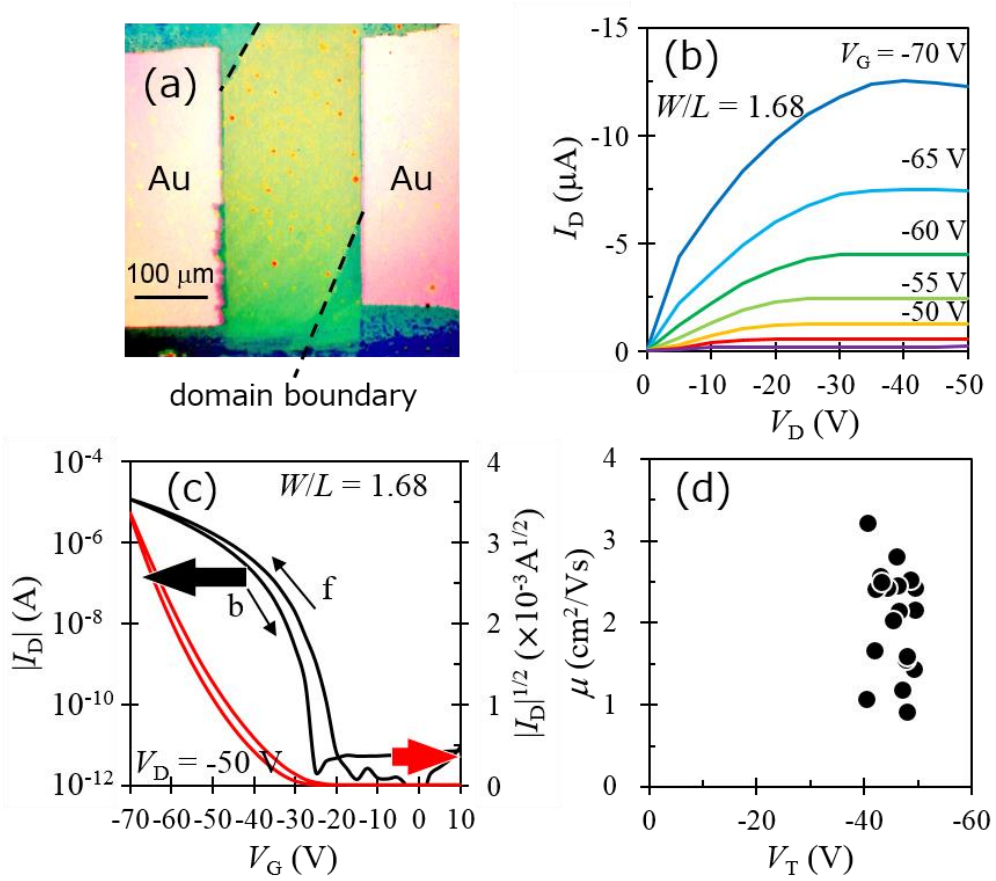

Figure 4.5 (a) Typical polarized optical image of FET with large crystalline domains after pre-annealing. Typical output (b) and transfer (c) characteristics, and plots of field-effect mobility as a function of threshold voltage (d) after pre-annealing of C8-BTBT/PMMA double layer.

4.3.2 Effects of light irradiation

Next, effects of light irradiation on the C8-BTBT/PMMA double layer will be discussed. In this process, the double-layered FETs with top-contact Au electrodes (20 nm) were irradiated by a metal-halide lamp in the ambient atmosphere in a chamber, where illuminance was about 1700 lx (1700 lm/m^2). During the irradiation, transfer characteristics at V_D = -50 V were measured per 1 h.

Figure 4.6 shows the typical results of the transfer characteristic measurement during the series of the irradiating process. The transfer curves in all cases, especially under light irradiation, showed hysteresis during the forward/backward scan. Thus, the mobility and threshold voltage were calculated by taking an average of values which were measured in the forward/backward scan. Firstly, the transfer measurement was performed in the dark in vacuum beforehand (Figure 4.6a). Then, the vacuum atmosphere was converted to the ambient atmosphere and light irradiation began. When the light was irradiated in the ambient atmosphere, there appeared large hysteresis on the characteristic curve (Figure 4.6b). According to the occurrence of the hysteresis, threshold voltage was reduced (-46 V to -39 V). Field-effect mobility, on the other hand, was almost consistent (2.5 cm^2/Vs to 2.5 cm^2/Vs). Then, light irradiation continued for 66 h. Figure 4.6c shows a transfer characteristic measured at t = 66 h. During the irradiation, the maximum amount of the current at V_G = -70 V increased further, and mobility was also drastically improved (2.5 cm^2/Vs to 8.6 cm^2/Vs). At this time, threshold voltage was also shifted further (-39 V to -27 V). After that, the ambient atmosphere was converted to vacuum again, and transfer measurement was performed in the dark in vacuum (Figure 4.6d). Under the vacuum atmosphere, the hysteresis was vanished and threshold voltage was also restored (-27 V to -41 V). In contrast to the threshold voltage restoration, high mobility was maintained in vacuum (8.6 cm^2/Vs to 9.6 cm^2/Vs). The series of the above experiment indicate that the observed mobility enhancement was not a temporal phenomenon but an intrinsic one.

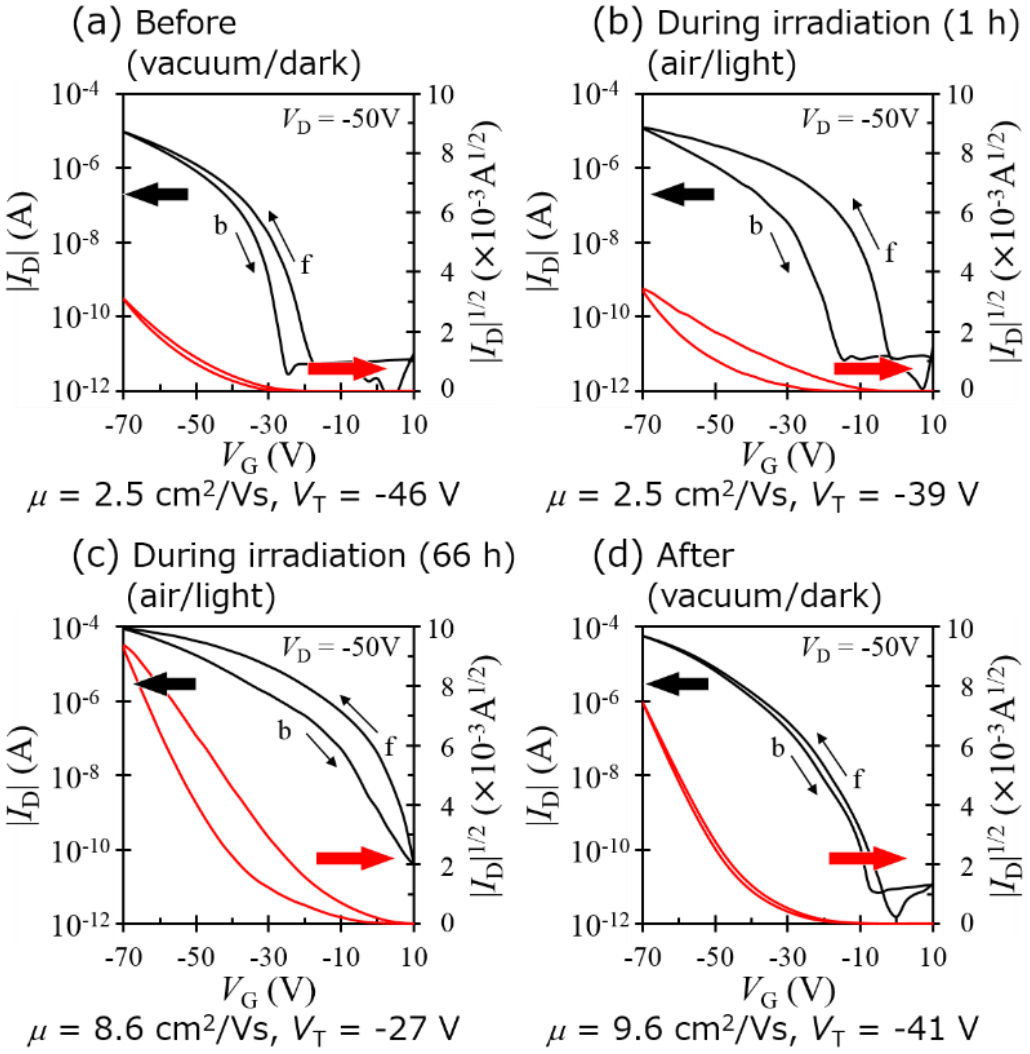

Figure 4.6 Transfer characteristics measured during the series of light irradiation process. (a,d) Characteristics measured in the dark in vacuum before (a) and after (d) for 66 h. (b,c) Characteristics measured in the ambient atmosphere during irradiation at t = 1 h (b) and 66 h (c). W/L of the device was 1.65.

Output characteristic was also measured before and after the irradiation in vacuum as shown in Figure 4.7. In both cases, a good saturation behavior was observed and the amount of the current was drastically improved after light irradiation (Figure 4.7a,b). In addition to the increase of the current, a different behavior was also observed in a small V_D region in output curves (Figure 4.7c,d). In these figures, the offset drain voltages were indicated by extrapolation of the red dashed lines. This non-linear feature comes from charge-injection limiting at the semiconductor/electrodes interface.[128] Therefore, a transition of the offset value from a plus region to a minus one suggested a change of the energetic barrier at the C8-BTBT/electrode interface.

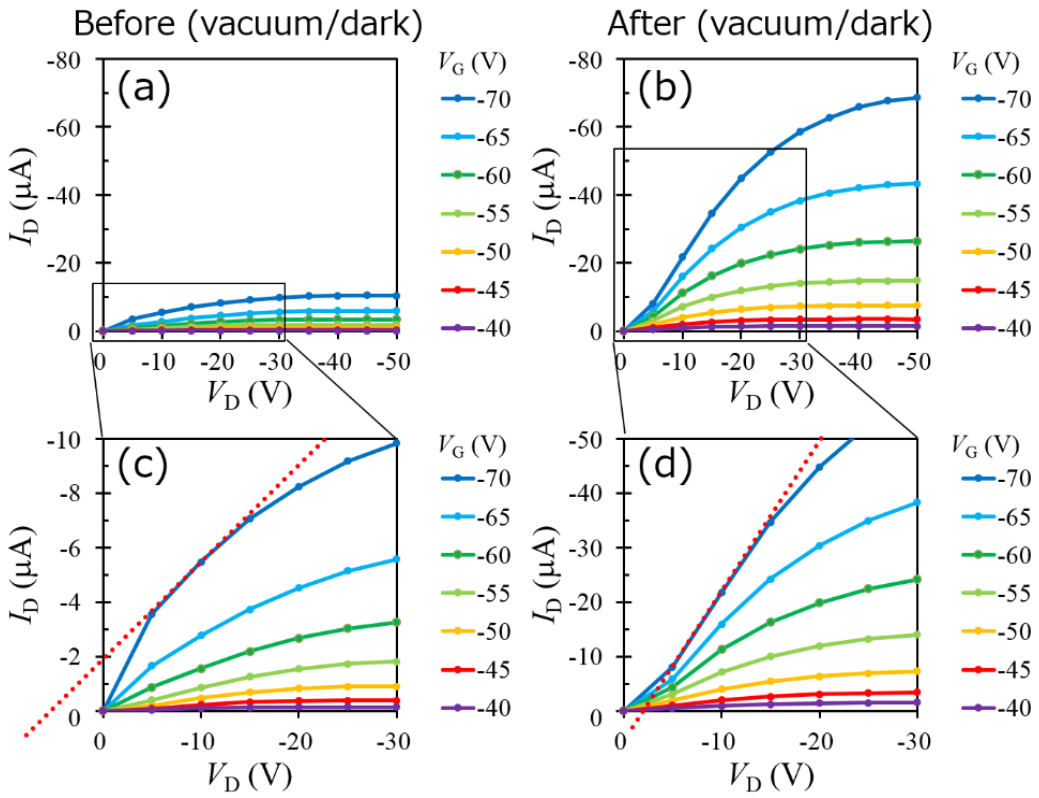

Figure 4.7 Output characteristics measured in the dark in vacuum before (a,c) and after (b,d) the light irradiation. These were the same device with the case in Figure 4.6 (W/L was 1.65). (c) and (d) shows small V_D regions in (a) and (b) respectively. Red dashed lines in (c) and (d) indicate extrapolation of offset drain voltage.

Figure 4.8 shows time dependences of four devices under light irradiation on three parameters: mobility as raw data, mobility standardized by an initial value, and threshold voltage as raw data. As shown in Figure 4.8a, mobility was enhanced and saturated up to as high as 8-12 cm^2/Vs in tens of hours. The standardized values indicate the mobility of each device was enhanced by four times from its initial value (Figure 4.8b). Although the enhancement ratio was roughly constant, the saturation time of each device was different. With respect to threshold voltage, the voltage value was firstly dropped in the initial several hours and was gradually decreased in the subsequent tens of hours (Figure 4.8c). The behavior of decreasing of threshold voltage was supposed to be caused by the inducement of traps by light irradiation.

In this study, I also used room light (fluorescent lamp; 700 lx) for irradiation instead of the metal-halide lamp. In that case, similar behaviors of mobility enhancement and threshold-voltage shift were observed. Such change in FET performance seems to occur in various kinds of lamps other than the metal-halide lamp.

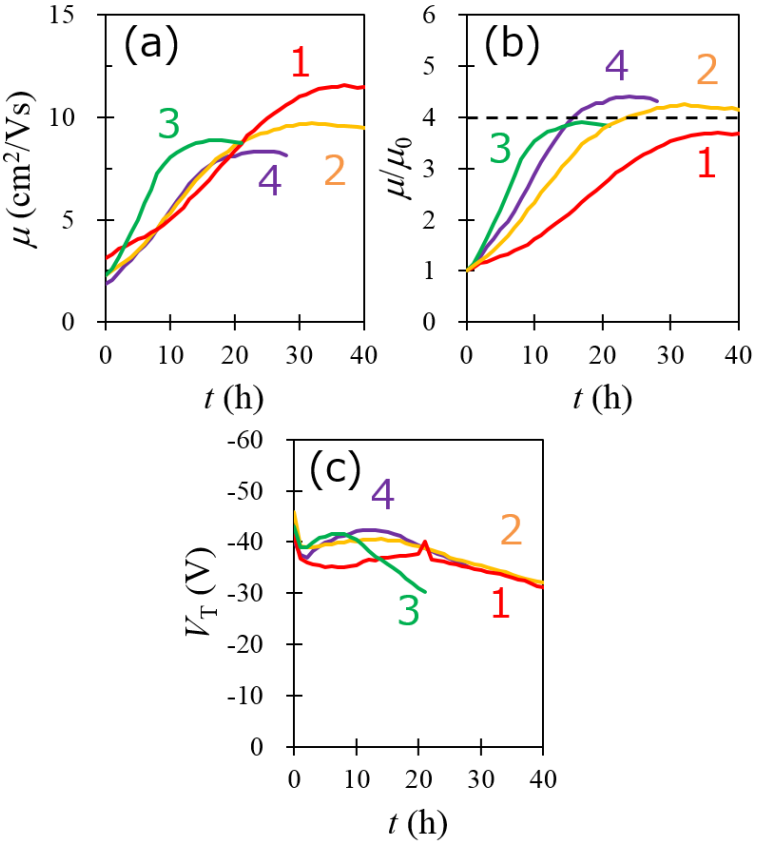

Figure 4.8 Time dependence during light irradiation of mobility (a), standardized mobility (b) and threshold voltage (c) of four devices.

4.3.3 Conditions to induce mobility enhancement

To understand conditions for mobility enhancement, detailed investigations were performed. At first, light was irradiated on various kinds of devices. Figure 4.9a,b show the results of time dependence of mobility under light irradiation on an as-spin-coated C8-BTBT/PMMA double-layered FET and as-spin-coated C8-BTBT FET. In both cases, mobility was not enhanced by light irradiation. I also investigated the time dependence on a pre-annealed C8-BTBT FET. In that case, there appeared a too large hysteresis to estimate mobility during the irradiation. After the irradiation, FET measurement on that device was performed in vacuum but no significant change was observed. Thus, both of the underlying PMMA layer and pre-annealing procedure seemed essential for mobility enhancement.

Here, the above results gave rise to another assumption that the dielectric

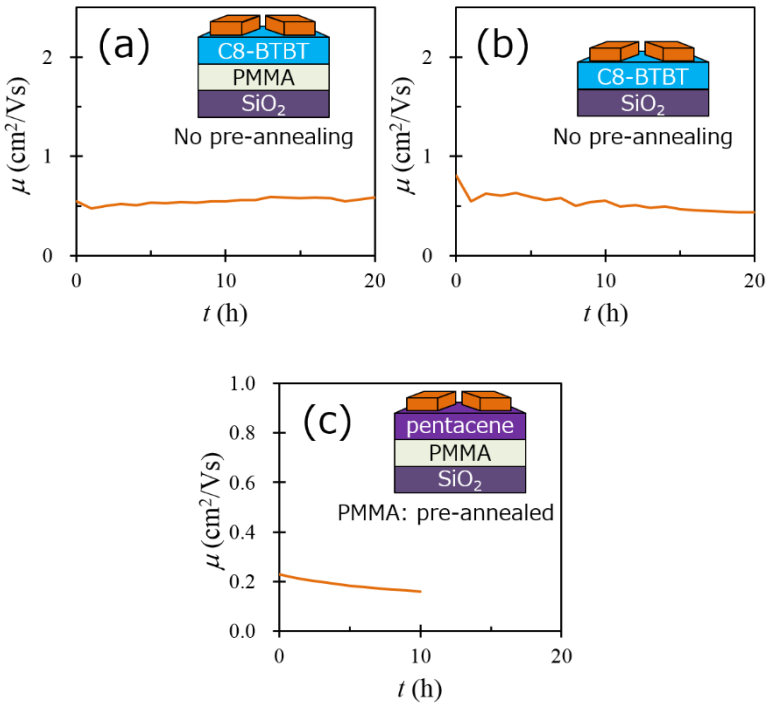

Figure 4.9 Time dependence of mobility under light irradiation on as-spin-coated C8-BTBT/PMMA double-layered FET (a), as-spin-coated C8-BTBT FET (b), and deposited-pentacene/pre-annealed-PMMA double-layered FET (c).

capacitance of the pre-annealed PMMA layer had changed during the light irradiation. To investigate this assumption, I also measured time dependence of a pentacene/PMMA FET where a pentacene layer was deposited on a pre-annealed PMMA layer. However, no current enhancement was observed (Figure 4.9c). This result means that the dielectric capacitance of the PMMA layer did not change during the irradiation. Thus, mobility enhancement was observed only in the case of a pre-annealed C8-BTBT/PMMA double layer. In the following, the environments for mobility enhancement were investigated on this device structure.

Figure 4.10 summarizes the time dependences of field-effect mobility of four FETs in various environments. Firstly, the pre-annealed C8-BTBT/PMMA double-layered FET was put into the dark/air environment. In that case, the mobility was

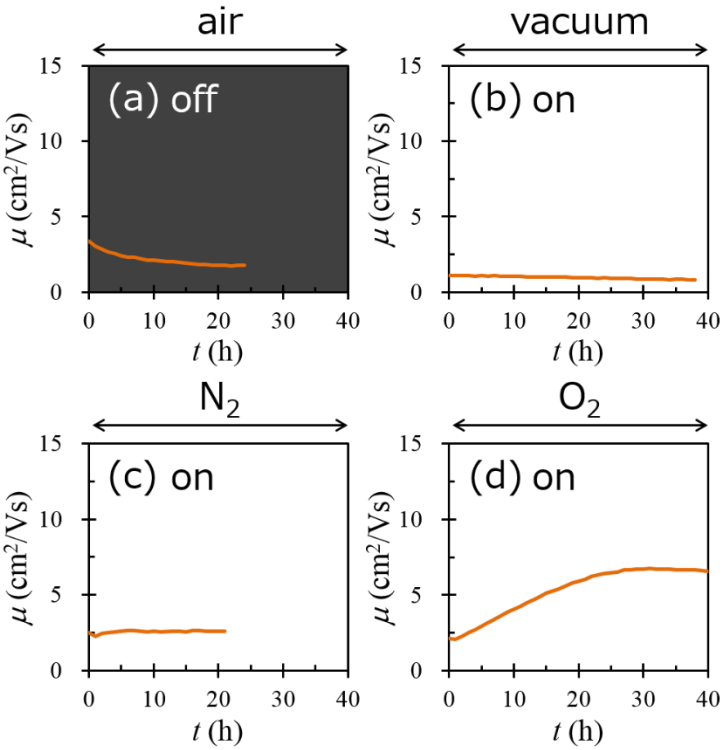

Figure 4.10 Time dependences of field-effect mobility on four FETs (pre-annealed C8-BTBT/PMMA double-layered). Each FET was measured in the dark in air (a), under light irradiation in vacuum (b), under irradiation in nitrogen atmosphere (c), and under irradiation in oxygen atmosphere (d).

constantly decreased (Figure 4.10a). This result indicated that the light irradiation was essential for the mobility enhancement. The light irradiation was performed on other three FETs in various atmospheres: vacuum, nitrogen gas (1 atm) and oxygen gas (1 atm). As shown in Figure 4.10b-d, mobility had no significant change in vacuum and the nitrogen atmosphere, while it was improved in the oxygen atmosphere. These results suggested the interaction between light and oxygen was a key factor for the mobility enhancement.

The mobility durability after enhancement was also investigated. Figure 4.11 shows time dependences of four FETs after the saturation of mobility enhancement in the ambient (a), vacuum (b), nitrogen (c), and oxygen (d) atmospheres. In all cases, mobility was once rapidly enhanced in several hours after the lamp was turned off. This enhancement was caused by cancellation of hysterisis during measurement. After that, in the case of the ambient atmosphere, the mobility was rapidly decreased in tens of hours (Figure 4.11a). When the lamp was turned on again after the decrease of mobility, the mobility was immediately restored. On the other hand, the mobility was not decreased after turning off the lamp in vacuum, nitrogen, and oxygen atmospheres (Figure 4.11b-d). The decrease of mobility in the ambient atmosphere was supposed to be caused by impurities in air such as water molecules, which would be removed by excitation under subsequent light irradiation. Thus, the enhanced mobility was revealed to be maintained in the proper atmosphere.

Throughout the all investigations, the mobility enhancement occurred on pre-annealed C8-BTBT/PMMA double-layered FETs, where both of pre-annealing procedure and a C8-BTBT/PMMA double-layered structure were key factors for the device preparation. In this scheme, the light irradiation or the oxygen atmosphere were also found essential for the enhancement. In addition, the mobility value after the enhancement was found to be maintained in the proper atmospheres. This result suggests the improved FETs will be applied for practical devices with a protective coat against the ambient atmosphere.

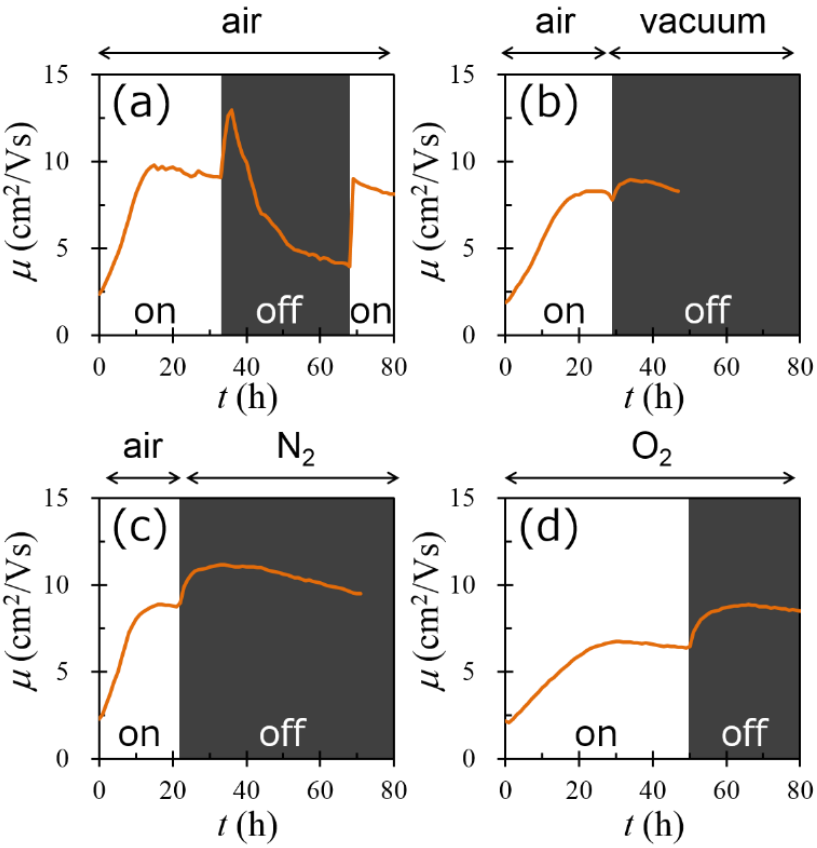

Figure 4.11 Time dependences of mobility on pre-annealed C8-BTBT/PMMA double-layered FETs. These FETs were exposed to various atmospheres after the saturation of mobility enhancement. Each device was exposed to air (a), vacuum (b), nitrogen (c), and oxygen (d) atmospheres, respectively.

4.3.4 Characterization of film before/after irradiation

To investigate a mechanism of mobility enhancement, various film characterizations were performed. Firstly, out-of-plane and in-plane X-ray difraction (XRD) measurement were carried out to elucidate the influence of irradiation on the crystallinity of C8-BTBT film (Figure 4.12). In the out-of-plane measurement (Figure 4.12a), there appeared three peaks around 3°, 6° and 9° in all cases of as-spin-coated (1), as-pre-annealed (2) and light-irradiated (3) films. These peaks were ascribed to the diffractions from (001) plane, (002) plane and (003) plane of C8-BTBT crystal lattice respectively.[90,129] In the in-plane measurement, there also appeared three peaks at 18°, 22° and 27° which were ascribed to the diffractions from (110) plane, (020) plane and (120) plane of C8-BTBT crystal lattice.[90,129] The difference of intensity ratio was due to the uniaxially directional recrystallization during the pre-annealing procedure. Another peak at 38° in the in-plane pattern was ascribed to the diffraction from (111) plane of Au electrodes. Throughout these measurement, all the observed peaks suggested that C8-BTBT molecules were "standing" (*c*-axis was perpendicular to the substrate) on the substrate, and no peak was observed suggesting molecules were "lying" (*c*-axis was parallel to the substrate). Table 4.1 summarizes the measured peak positions of (003) plane, (020) plane and (120) plane of C8-BTBT crystal lattice, and calculated crystallographic parameters of *a* axis, *b* axis and interlayer distance *d*. Here, as the (120) peak had small intensity, the values of (120) peak position and *a* axis distance had small significant figures. As shown in this table, there was no significant change in crystallographic parameters during the series of procedures of spin-coating, pre-annealing and light irradiation.

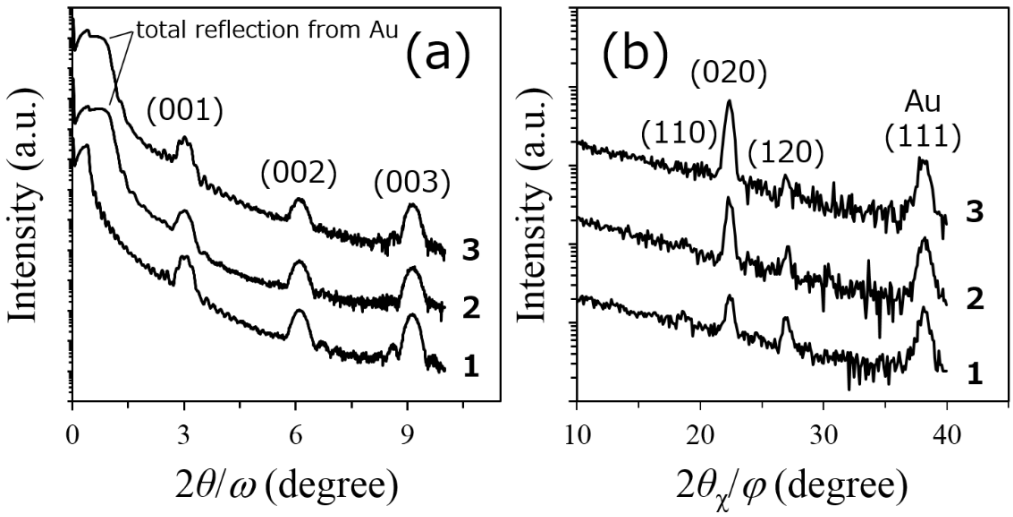

Figure 4.12 Out-of-plane (a) and in-plane (b) X-ray diffraction (XRD) pattern of as-spin-coated (1), as-pre-annealed (2), and light-irradiated (3) C8-BTBT/PMMA double-layered films. All films except for (a-1) had Au electrodes on their surface. Film in (a-1) had no Au electrodes on its surface.

Table 4.1 Crystallographic parameters calculated from XRD measurement.

	as-spin-coated	as-annealed	light-irradiated
(003) peak [°]	9.129(1)	9.138(2)	9.137(1)
(020) peak [°]	22.37(1)	22.344(9)	22.334(5)
(120) peak [°]	26.96(2)	27.07(4)	26.94(4)
a [nm]	0.596(5)	0.587(7)	0.595(9)
b [nm]	0.7941(5)	0.7951(3)	0.7954(2)
d [nm]	2.9036(4)	2.9010(6)	2.9011(5)

Next, Raman scattering spectra of C8-BTBT/PMMA double layer were obtained. Figure 4.13 shows the Raman spectra of as-spin-coated (1), as-pre-annealed (2) and light-irradiated (3) films in addition to the spectra of drop-cast C8-BTBT film (a) and as-spin-coated PMMA film (b) as reference. In the spectra of (1)-(3), scattering from both of C8-BTBT molecules and PMMA molecules was observed, which is consistent with the previous study on Raman spectroscopy on the C8-BTBT/PMMA double-layered film.[130] Although the mobility enhancement occurred only in the ambient or oxygen atmospheres, the evidence of oxidization of C8-BTBT molecules could not be observed in these Raman spectra. However, only in the case of (2) and (3), there appeared a strong peak at 1600 cm^{-1}. In the case of a pentacene thin film, it is well-known that a peak around 1600 cm^{-1} is a B_{3g} mode, which is sensitive to molecular angle.[131–133] In the B_{3g} mode, when the incident laser light enters

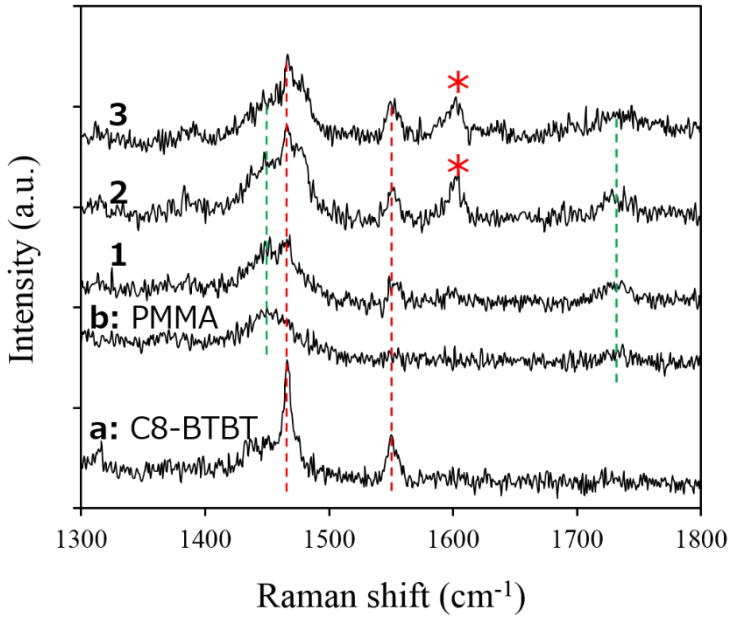

Figure 4.13 Raman spectra of drop-cast C8-BTBT film (a), as-spin-coated PMMA film (b), as-spin-coated double-layered film (1), as-pre-annealed double-layered film (2) and light-irradiated double-layered film (3). C8-BTBT molecules' scatterings were indicated as red dashed lines and PMMA molecules' scatterings were as green lines. Especially C8-BTBT molecules' scatterings at 1600 cm^{-1} were indicated as asterisks. Wavelength of incident laser light was 532 nm.

perpendicular to the substrate, "lying" molecules on the substrate have stronger intensity of B_{3g} mode, while "standing" molecules have weaker intensity. In the case of C8-BTBT, the vibration mode at 1600 cm^{-1} was similar to the pentacene B_{3g} mode by density functional theory (DFT) calculation (RB3LYP, 6-31G(*d*,*p*)). The "lying" C8-BTBT molecules which caused the B_{3g}-mode scattering seemed to be formed through the pre-annealing procedure and they did not change through the light irradiation.

To elucidate further the film morphology, atomic force microscope (AFM) measurement was performed (Figure 4.14). This measurement was aimed to reveal the interfacial structure of C8-BTBT molecules on the underlying PMMA layer. Firstly, a several-mono-layered C8-BTBT/PMMA film was fabricated by spin-coating of mixed solution of 0.05 wt.% C8-BTBT and 1 wt.% PMMA (only C8-BTBT was diluted by 10 times). Figure 4.14a and 4.14b are the AFM images of as-pre-annealed and light-irradiated film. As shown in these images, the interfacial layers had 1.5 nm height. With respect that a single C8-BTBT molecule's length is 3 nm (along with the long axis), this result suggested the interfacial molecules in at least two mono-layers were not "standing" but "lying". This suggestion was also supported by the corresponding Raman spectra of each film, where the strong peak at 1600 cm^{-1} was observed in both cases (insets in Figure 4.14a,b). Since such "lying" structure was composed of as thin as several mono-layers, that structure seemed not to be observed by the previous XRD measurement. Next, AFM measurement was carried out on an as-pre-annealed film which was fabricated by spin-coating of mixed solution of 0.08 wt.% C8-BTBT and 1 wt.% PMMA (Figure 4.14c). In this case, the amount of C8-BTBT molecules was increased and there partly appeared very flat table-like structures with 6 nm height. Such flat table-like layers were known to be composed of "standing" molecules and their height could be ascribed to two "standing" mono-layers. Thus, the AFM image of Figure 4.14c showed the coexistence of "standing" and "lying" molecules. In addition, I also investigated on the case of as-pre-annealed PMMA film. In that case, there appeared no significant structure with larger than 1.5 nm thickness (Figure 4.14d).

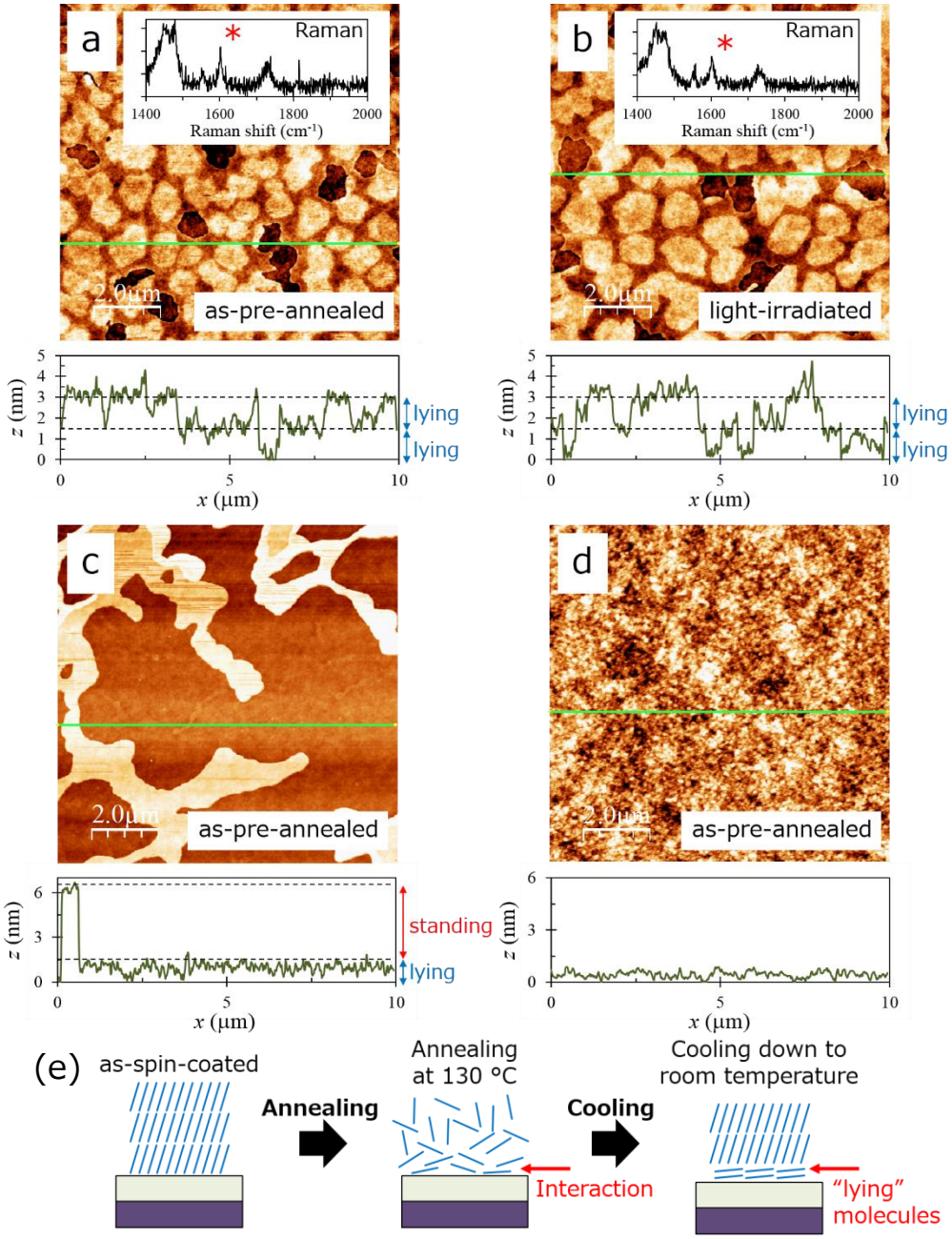

Figure 4.14 (a-d) AFM images and corresponding line profiles of as-pre-annealed double-layered film (a,c), light-irradiated double-layered film (b), and as-pre-annealed PMMA film (d). Double layers were fabricated by spin-coating of mixed solution of 0.05 wt.% C8-BTBT and 1 wt.% PMMA (a,b) or 0.08 wt.% C8-BTBT and 1 wt.% PMMA (c). PMMA layer was fabricated using 1 wt.% solution. Insets in (a) and (b) are Raman spectra of each film, where peaks at 1600 cm^{-1} is indicated as red asterisks. (e) Schematic illustration of possible mechanism of formation of "lying" layers.

In this way, C8-BTBT molecules were revealed to have “lying” structure at the interface. This structure was supposed to be caused by the interaction between C8-BTBT and PMMA during the pre-annealing procedure (Figure 4.14e).

As a result, there observed no obvious change before/after the light irradiation in XRD, Raman and AFM measurement. The morphological change could be observed during the pre-annealing procedure in Raman and AFM measurement, although the relation between the morphology and mobility enhancement was still unknown. As field-effect mobility relates to the electronic states of conducting materials, the electronic states of the C8-BTBT layer seemed to be changed during the irradiation. Indeed, in output characterization in FET measurement, a unique non-linear behavior was observed in a small-drain-voltage region after pre-annealing. This non-linear behavior indicated the charge-carrier limiting at the semiconductor/electrode interface. Thus, there seems to remain room for further investigation on the change of electronic states of the C8-BTBT layer before/after the irradiation. However, the electronic states of C8-BTBT molecules could not be characterized by conventional ultraviolet-photoelectron spectroscopy (UPS) because of an underlying thick PMMA layer, which caused charge-up during UPS measurement. To understand the mechanism further, it will be necessary to investigate the electronic states by other than photoelectron spectroscopy, such as Kelvin-prove force microscopy (KFM).

4.4 Conclusion

In this chapter, I achieved post-processing modulation of field-effect mobility of C8-BTBT FETs assisted by light irradiation. In the irradiating process, mobility was increased by four times from 1-3 cm^2/Vs to as high as 8-12 cm^2/Vs in tens of hours. When the irradiating lamp was turned off in vacuum, the threshold-voltage shift was restored, while the enhancement of mobility was maintained. The investigation on the device configuration and enhancement condition revealed that such phenomenon occurred only in the case of pre-annealed C8-BTBT/PMMA double-layered FETs in the ambient or oxygen atmosphere. Characterizations on the C8-BTBT film during the series of the procedures were carried out by XRD, Raman and AFM measurement. In XRD measurement, crystallinity of C8-BTBT was found consistent before/after the irradiation. In Raman spectroscopy, there was no obvious evidence of oxidization of C8-BTBT molecules during the irradiation. In addition, Raman and AFM measurement revealed the morphological change during the pre-annealing, showing the formation of “lying” C8-BTBT molecules at the C8-BTBT/PMMA interface. However, the mechanism of the mobility enhancement has yet to be determined. Since the field-effect mobility seemed to relate to the electronic states of the C8-BTBT layer, further investigation on its electronic states is expected to elucidate the mechanism of the mobility enhancement. The post-processing light irradiation itself is so facile that the elucidation of the mechanism will promote further the practical fabrication of high-mobility OFET.

Chapter 5. Concluding Remarks

In this dissertation, I developed novel external-field-assisted fabrication processes of OFETs in three kinds of studies as follows.

Application of Electric Field after Drop-Casting (Chapter 2)

In Chapter 2, electric field was applied after drop-casting of pentacene solution. Pentacene single crystals were grown just after drop-casting via rapid cooling and subsequently the electric field was applied. To observe the crystal movement, I developed a real-time optical microscopy. In the observation, pentacene crystals were revealed to respond to the dc electric field as if they were positively charged. I discussed that the contact electrification occurred between the pentacene crystals and surrounding solvent according to the Coehn's rule. In the case of application of ac electric field, the charged crystals swung between electrodes. These crystals could be placed on the channel under the optimized ac electric field. The grown crystals were characterized with respect to the crystals orientation and FET performance. In the orientation characterization, the crystals with larger aspect ratio were found more likely to align the $[\bar{1}10]$ crystallographic axis parallel to the applied electric field. In the FET characterization the crystals whose $[\bar{1}10]$ crystallographic axis parallel to the channel length showed higher mobility, which was consistent with the recent first principle calculation. This result suggested the pentacene crystals with large aspect ratio could be aligned by the electric field along the certain direction which was suitable from a viewpoint of the mobility anisotropy. The maximum mobility was calculated as 0.49 cm^2/Vs, showing that as-deposited crystals from solution could work as a field-effect transistor. Application of electric field in solution was found effective for placement and orientation control of organic single crystals.

Application of Electric Field during Solvent Vapor Annealing (Chapter 3)

In Chapter 3, electric field was applied during solvent vapor annealing (SVA). C8-BTBT nucleated and grew further near the substrate during the SVA process. Thus, electric field worked on the *growing* crystals unlike the case on the *grown* crystals in Chapter 2. This scheme lead to the self-assembly of single crystals with uniform size and orientation. I developed a real-time optical microscopy and observed the crystal movement under electric field. When electric field was applied, the SVA-growing crystals behaved like a negatively charged substance. In addition, the crystals were automatically rotated their directions parallel to the field just bridging over the two electrodes. I investigated this electric-field-assisted SVA on the two kinds of configurations: PMMA-on-Au configuration and Au-on-PMMA configuration. On the first PMMA-on-Au configuration, the C8-BTBT crystals could be highly aligned according to the electric field. However, the fabricated FETs had poor FET performance because of a remaining PMMA layer between C8-BTBT crystals and Au electrodes. On the second Au-on-PMMA configuration, on the other hand, the crystals and electrodes could contact directly and the grown crystals showed a good FET performance of as large as 1.9 cm^2/Vs. Application of electric field during SVA was proved effective for placement and orientation control of organic crystals and also effective for fabrication of high-mobility OFETs.

Light Irradiation on C8-BTBT FETs (Chapter 4)

In Chapter 4, light was irradiated on the C8-BTBT FETs after fabrication. The light was irradiated on the pre-annealed C8-BTBT/PMMA double-layered FETs and the mobility was increased by 4 times from 1-3 cm^2/Vs to as high as 8-12 cm^2/Vs in tens of hours. The investigation on the device configuration and enhancement condition revealed that this phenomenon occurred only in the case of a pre-annealed C8-BTBT/PMMA double-layered FET in the ambient or oxygen atmospheres. In XRD and Raman measurement, it could be observed

neither changes of crystallinity of the C8-BTBT layer nor evidence of oxidization of C8-BTBT molecules. With respect to the electronic states of the C8-BTBT layer, further investigation is expected to elucidate the present mechanism. The elucidation of the mechanism will realize practical application of the present facile post-processing light irradiation.

Throughout this dissertation, I found external electric field was effective to align various organic crystals and light irradiation could modulate FET performance even after fabrication. In the current OFET research, design and synthesis of organic semiconductor molecule are more enthusiastically integrated than process-engineering. To push OFETs closer to practical applications, however, compatibility of integrated molecules and fabrication process is essential. In this respect, I proposed novel but facile fabrication techniques which is applicable for various kinds of molecules. I believe that these fundamental findings will provide new insights for practical fabrication of the current integrated molecules and open a way for the further improvement of OFET fabrication.

References

Own works

(A) Kotsuki, K.; Tanaka, H.; Obata, S.; Stauss, S.; Terashima, K.; Saiki, K. The Importance of Spinning Speed in Fabrication of Spin-Coated Organic Thin Film Transistors: Film Morphology and Field Effect Mobility. *Appl. Phys. Lett.* **2014**, *104*, 233306.

(B) Kotsuki, K.; Obata, S.; Saiki, K. Electric-Field-Assisted Position and Orientation Control of Organic Single Crystals. *Langmuir* **2014**, *30*, 14286–14291.

(C) Kotsuki, K.; Obata, S.; Saiki, K. Self-Aligned Growth of Organic Semiconductor Single Crystals by Electric Field. *Langmuir* **2016**, *32*, 644–649.

Other works

(1) Ebisawa, F.; Kurokawa, T.; Nara, S. Electrical Properties of Polyacetylene/polysiloxane Interface. *J. Appl. Phys.* **1983**, *54*, 3255.

(2) Kudo, K.; Yamashina, M.; Moriizumi, T. Field Effect Measurement of Organic Dye Films. *Jpn. J. Appl. Phys.* **1984**, *23*, 130.

(3) Tsumura, A.; Koezuka, H.; Ando, T. Macromolecular Electronic Device: Field-Effect Transistor with a Polythiophene Thin Film. *Appl. Phys. Lett.* **1986**, *49*, 1210–1212.

(4) Assadi, A.; Svensson, C.; Willander, M.; Inganäs, O. Field-Effect Mobility of poly(3-Hexylthiophene). *Appl. Phys. Lett.* **1988**, *53*, 195.

(5) Horowitz, G.; Fichou, D.; Peng, X.; Xu, Z.; Garnier, F. A Field-Effect Transistor Based on Conjugated Alpha-Sexithienyl. *Solid State Commun.* **1989**, *72*, 381–384.

(6) Liu, S.; Wang, W. M.; Briseno, A. L.; Mannsfeld, S. C. B.; Bao, Z. Controlled Deposition of Crystalline Organic Semiconductors for Field-Effect-Transistor Applications. *Adv. Mater.* **2009**, *21*, 1217–1232.

(7) Wen, Y. G.; Liu, Y. Q.; Guo, Y. L.; Yu, G.; Hu, W. P. Experimental Techniques for the Fabrication and Characterization of Organic Thin Films for Field-Effect Transistors. *Chem. Rev.* **2011**, *111*, 3358–3406.

(8) Wang, C.; Dong, H.; Hu, W.; Liu, Y.; Zhu, D. Semiconducting π-Conjugated Systems in Field-Effect Transistors: A Material Odyssey of Organic Electronics. *Chem. Rev.* **2012**, *112*, 2208–2267.

(9) Sirringhaus, H. 25th Anniversary Article: Organic Field-Effect Transistors: The Path Beyond Amorphous Silicon. *Adv. Mater.* **2014**, *26*, 1319–1335.

(10) Diao, Y.; Shaw, L.; Bao, Z.; Mannsfeld, S. C. B. Morphology Control Strategies for Solution-Processed Organic Semiconductor Thin Films. *Energy Environ. Sci.* **2014**, *7*, 2145–2159.

(11) Li, Y.; Sun, H.; Shi, Y.; Tsukagoshi, K. Patterning Technology for Solution-Processed Organic Crystal Field-Effect Transistors. *Sci. Technol. Adv. Mater.* **2014**, *15*, 24203.

(12) Shaw, L.; Bao, Z. The Large-Area, Solution-Based Deposition of Single-Crystal Organic Semiconductors. *Isr. J. Chem.* **2014**, *54*, 496–512.

(13) Menard, E.; Podzorov, V.; Hur, S. H.; Gaur, A.; Gershenson, M. E.; Rogers, J. A. High-Performance *n*- and *p*-Type Single-Crystal Organic Transistors with Free-Space Gate Dielectrics. *Adv. Mater.* **2004**, *16*, 2097–2101.

(14) Sundar, V. C.; Zaumseil, J.; Podzorov, V.; Menard, E.; Willett, R. L.; Someya, T.; Gershenson, M. E.; Rogers, J. A. Elastomeric Transistor Stamps : Transport in Organic Crystals. *Science (80-.).* **2004**, *303*, 1644–1646.

(15) Reese, C.; Bao, Z. High-Resolution Measurement of the Anisotropy of Charge Transport in Single Crystals. *Adv. Mater.* **2007**, *19*, 4535–4538.

(16) Jurchescu, O. D.; Popinciuc, M.; van Wees, B. J.; Palstra, T. T. M. Interface-Controlled, High-Mobility Organic Transistors. *Adv. Mater.* **2007**, *19*, 688–692.

(17) Nakayama, K.; Hirose, Y.; Soeda, J.; Yoshizumi, M.; Uemura, T.; Uno, M.; Li, W.; Kang, M. J.; Yamagishi, M.; Okada, Y.; *et al.* Patternable Solution-Crystallized Organic Transistors with High Charge Carrier Mobility. *Adv. Mater.* **2011**, *23*, 1626.

(18) Minemawari, H.; Yamada, T.; Matsui, H.; Tsutsumi, J.; Haas, S.; Chiba, R.;

Kumai, R.; Hasegawa, T. Inkjet Printing of Single-Crystal Films. *Nature* **2011**, *475*, 364–367.

(19) Li, J.; Zhao, Y.; Tan, H. S.; Guo, Y.; Di, C.-A.; Yu, G.; Liu, Y.; Lin, M.; Lim, S. H.; Zhou, Y.; *et al.* A Stable Solution-Processed Polymer Semiconductor with Record High-Mobility for Printed Transistors. *Sci. Rep.* **2012**, *2*, 754.

(20) Li, H.; Tee, B. C. K.; Cha, J. J.; Cui, Y.; Chung, J. W.; Lee, S. Y.; Bao, Z. High-Mobility Field-Effect Transistors from Large-Area Solution-Grown Aligned C_{60} Single Crystals. *J. Am. Chem. Soc.* **2012**, *134*, 2760–2765.

(21) Amin, A. Y.; Khassanov, A.; Reuter, K.; Meyer-Friedrichsen, T.; Halik, M. Low-Voltage Organic Field Effect Transistors with a 2-Tridecyl[1]benzothieno[3,2-b][1]benzothiophene Semiconductor Layer. *J. Am. Chem. Soc.* **2012**, *134*, 16548–16550.

(22) Soeda, J.; Uemura, T.; Okamoto, T.; Mitsui, C.; Yamagishi, M.; Takeya, J. Inch-Size Solution-Processed Single-Crystalline Films of High-Mobility Organic Semiconductors. *Appl. Phys. Express* **2013**, *6*, 76503.

(23) Diao, Y.; Tee, B. C.-K.; Giri, G.; Xu, J.; Kim, D. H.; Becerril, H. A.; Stoltenberg, R. M.; Lee, T. H.; Xue, G.; Mannsfeld, S. C. B.; *et al.* Solution Coating of Large-Area Organic Semiconductor Thin Films with Aligned Single-Crystalline Domains. *Nat. Mater.* **2013**, *12*, 665–671.

(24) Mitsui, C.; Okamoto, T.; Yamagishi, M.; Tsurumi, J.; Yoshimoto, K.; Nakahara, K.; Soeda, J.; Hirose, Y.; Sato, H.; Yamano, A.; *et al.* High-Performance Solution-Processable N-Shaped Organic Semiconducting Materials with Stabilized Crystal Phase. *Adv. Mater.* **2014**, *26*, 4546.

(25) Okamoto, H.; Hamao, S.; Goto, H.; Sakai, Y.; Izumi, M.; Gohda, S.; Kubozono, Y.; Eguchi, R. Transistor Application of Alkyl-Substituted Picene. *Sci. Rep.* **2014**, *4*, 5048.

(26) Yuan, Y.; Giri, G.; Ayzner, A. L.; Zoombelt, A. P.; Mannsfeld, S. C. B.; Chen, J.; Nordlund, D.; Toney, M. F.; Huang, J.; Bao, Z. Ultra-High Mobility Transparent Organic Thin Film Transistors Grown by an off-Centre Spin-Coating Method. *Nat. Commun.* **2014**, *5*, 3005.

(27) Kwon, S.; Kim, J.; Kim, G.; Yu, K.; Jo, Y.-R.; Kim, B.-J.; Kim, J.; Kang, H.; Park, B.; Lee, K. Organic Single-Crystal Semiconductor Films on a Millimeter

Domain Scale. *Adv. Mater.* **2015**, *27*, 6870–6877.

(28) Iino, H.; Usui, T.; Hanna, J. Liquid Crystals for Organic Thin-Film Transistors. *Nat. Commun.* **2015**, *6*, 6828.

(29) Sumimoto, T.; Shiratori, Y.; Iizuka, M.; Kuniyoshi, S.; Kudo, K.; Tanaka, K. Fabrication and Characterization of Field Effect Transistors of Layered Structure Consisting of TMTSF and TCNQ. *Synth. Met.* **1997**, *86*, 2259–2260.

(30) Hasegawa, T.; Mattenberger, K.; Takeya, J.; Batlogg, B. Ambipolar Field-Effect Carrier Injections in Organic Mott Insulators. *Phys. Rev. B* **2004**, *69*, 245115.

(31) Sakai, M.; Sakuma, H.; Ito, Y.; Saito, A.; Nakamura, M.; Kudo, K. Ambipolar Field-Effect Transistor Characteristics of (BEDT-TTF)(TCNQ) Crystals and Metal-like Conduction Induced by a Gate Electric Field. *Phys. Rev. B* **2007**, *76*, 45111.

(32) Kawasugi, Y.; Yamamoto, H. M.; Tajima, N.; Fukunaga, T.; Tsukagoshi, K.; Kato, R. Field-Induced Carrier Delocalization in the Strain-Induced Mott Insulating State of an Organic Superconductor. *Phys. Rev. Lett.* **2009**, *103*, 116801.

(33) Kawasugi, Y.; Yamamoto, H. M.; Tajima, N.; Fukunaga, T.; Tsukagoshi, K.; Kato, R. Electric-Field-Induced Mott Transition in an Organic Molecular Crystal. *Phys. Rev. B* **2011**, *84*, 125129.

(34) Yamamoto, H. M.; Nakano, M.; Suda, M.; Iwasa, Y.; Kawasaki, M.; Kato, R. A Strained Organic Field-Effect Transistor with a Gate-Tunable Superconducting Channel. *Nat. Commun.* **2013**, *4*, 2379.

(35) Sekitani, T.; Iba, S.; Kato, Y.; Noguchi, Y.; Someya, T.; Sakurai, T. Ultraflexible Organic Field-Effect Transistors Embedded at a Neutral Strain Position. *Appl. Phys. Lett.* **2005**, *87*, 173502.

(36) Someya, T.; Kato, Y.; Sekitani, T.; Iba, S.; Noguchi, Y.; Murase, Y.; Kawaguchi, H.; Sakurai, T. Conformable, Flexible, Large-Area Networks of Pressure and Thermal Sensors with Organic Transistor Active Matrixes. *Proc. Natl. Acad. Sci. U. S. A.* **2005**, *102*, 12321–12325.

(37) Mabeck, J. T.; Malliaras, G. G. Chemical and Biological Sensors Based on Organic Thin-Film Transistors. *Anal. Bioanal. Chem.* **2006**, *384*, 343–353.

(38) Roberts, M. E.; Mannsfeld, S. C. B.; Queraltó, N.; Reese, C.; Locklin, J.; Knoll, W.; Bao, Z. Water-Stable Organic Transistors and Their Application in Chemical and Biological Sensors. *Proc. Natl. Acad. Sci. U. S. A.* **2008**, *105*, 12134–12139.

(39) Sekitani, T.; Zschieschang, U.; Klauk, H.; Someya, T. Flexible Organic Transistors and Circuits with Extreme Bending Stability. *Nat. Mater.* **2010**, *9*, 1015–1022.

(40) Myny, K.; Steudel, S.; Smout, S.; Vicca, P.; Furthner, F.; van der Putten, B.; Tripathi, A. K.; Gelinck, G. H.; Genoe, J.; Dehaene, W. Organic RFID Transponder Chip with Data Rate Compatible with Electronic Product Coding. *Org. Electron.* **2010**, *11*, 1176–1179.

(41) Hammock, M. L.; Sokolov, A. N.; Stoltenberg, R. M.; Naab, B. D.; Bao, Z. Organic Transistors with Ordered Nanoparticle Arrays as a Tailorable Platform for Selective, in Situ Detection. *ACS Nano* **2012**, *6*, 3100–3108.

(42) Tien, N. T.; Jeon, S.; Kim, D.-I.; Trung, T. Q.; Jang, M.; Hwang, B.-U.; Byun, K.-E.; Bae, J.; Lee, E.; Tok, J. B.-H.; *et al.* A Flexible Bimodal Sensor Array for Simultaneous Sensing of Pressure and Temperature. *Adv. Mater.* **2014**, *26*, 796–804.

(43) Fukuda, K.; Takeda, Y.; Yoshimura, Y.; Shiwaku, R.; Tran, L. T.; Sekine, T.; Mizukami, M.; Kumaki, D.; Tokito, S. Fully-Printed High-Performance Organic Thin-Film Transistors and Circuitry on One-Micron-Thick Polymer Films. *Nat. Commun.* **2014**, *5*, 4147.

(44) Matsuhisa, N.; Kaltenbrunner, M.; Yokota, T.; Jinno, H.; Kuribara, K.; Sekitani, T.; Someya, T. Printable Elastic Conductors with a High Conductivity for Electronic Textile Applications. *Nat. Commun.* **2015**, *6*, 7461.

(45) Yoshida, H.; Sato, N. Crystallographic and Electronic Structures of Three Different Polymorphs of Pentacene. *Phys. Rev. B - Condens. Matter Mater. Phys.* **2008**, *77*, 235205.

(46) Lee, J. Y.; Roth, S.; Park, Y. W. Anisotropic Field Effect Mobility in Single Crystal Pentacene. *Applied Physics Letters*, 2006, *88*, 252106.

(47) Minari, T.; Kano, M.; Miyadera, T.; Wang, S.-D.; Aoyagi, Y.; Seto, M.;

Nemoto, T.; Isoda, S.; Tsukagoshi, K. Selective Organization of Solution-Processed Organic Field-Effect Transistors. *Applied Physics Letters*, 2008, *92*, 173301.

(48) Kumatani, A.; Liu, C.; Li, Y.; Darmawan, P.; Takimiya, K.; Minari, T.; Tsukagoshi, K. Solution-Processed, Self-Organized Organic Single Crystal Arrays with Controlled Crystal Orientation. *Sci. Rep.* **2012**, *2*, 393.

(49) Li, Y.; Liu, C.; Kumatani, A.; Darmawan, P.; Minari, T.; Tsukagoshi, K. Large Plate-like Organic Crystals from Direct Spin-Coating for Solution-Processed Field-Effect Transistor Arrays with High Uniformity. *Org. Electron. physics, Mater. Appl.* **2012**, *13*, 264.

(50) Lee, W. H.; Kim, D. H.; Jang, Y.; Cho, J. H.; Hwang, M.; Park, Y. D.; Kim, Y. H.; Han, J. I.; Cho, K. Solution-Processable Pentacene Microcrystal Arrays for High Performance Organic Field-Effect Transistors. *Appl. Phys. Lett.* **2007**, *90*, 132106.

(51) Uemura, T.; Hirose, Y.; Uno, M.; Takimiya, K.; Takeya, J. Very High Mobility in Solution-Processed Organic Thin-Film Transistors of Highly Ordered [1]Benzothieno[3,2-B]benzothiophene Derivatives. *Appl. Phys. Express* **2009**, *2*, 111501.

(52) Oh, J. H.; Lee, H. W.; Mannsfeld, S.; Stoltenberg, R. M.; Jung, E.; Jin, Y. W.; Kim, J. M.; Yoo, J.-B.; Bao, Z. Solution-Processed, High-Performance *n*-Channel Organic Microwire Transistors. *Proc. Natl. Acad. Sci. U. S. A.* **2009**, *106*, 6065–6070.

(53) Giri, G.; Verploegen, E.; Mannsfeld, S. C. B.; Atahan-Evrenk, S.; Kim, D. H.; Lee, S. Y.; Becerril, H. A.; Aspuru-Guzik, A.; Toney, M. F.; Bao, Z. Tuning Charge Transport in Solution-Sheared Organic Semiconductors Using Lattice Strain. *Nature* **2011**, *480*, 504–508.

(54) Goto, O.; Tomiya, S.; Murakami, Y.; Shinozaki, A.; Toda, A.; Kasahara, J.; Hobara, D. Organic Single-Crystal Arrays from Solution-Phase Growth Using Micropattern with Nucleation Control Region. *Adv. Mater.* **2012**, *24*, 1117–1122.

(55) Wo, S.; Headrick, R. L.; Anthony, J. E. Fabrication and Characterization of Controllable Grain Boundary Arrays in Solution-Processed Small Molecule

Organic Semiconductor Films. *J. Appl. Phys.* **2012**, *111*, 73716.

(56) Giri, G.; Park, S.; Vosgueritchian, M.; Shulaker, M. M.; Bao, Z. High-Mobility, Aligned Crystalline Domains of Tips-Pentacene with Metastable Polymorphs through Lateral Confinement of Crystal Growth. *Adv. Mater.* **2014**, *26*, 487–493.

(57) Ji, Z. G.; Wong, K. W.; Tse, P. K.; Kwok, R. W. M.; Lau, W. M. Copper Phthalocyanine Film Grown by Vacuum Deposition under Magnetic Field. *Thin Solid Films* **2002**, *402*, 79–82.

(58) Tabata, K.; Sasaki, T.; Yamamoto, Y. Magnetic-Field-Induced Enhancement of Crystallinity and Field-Effect Mobilities in Phthalocyanine Thin Films. *Appl. Phys. Lett.* **2013**, *103*, 43301.

(59) Sakai, M.; Nakamura, M.; Kudo, K. Organic Nanochannel Field-Effect Transistor with Organic Conductive Wires. *Appl. Phys. Lett.* **2007**, *90*, 62101.

(60) Fischer, F. S. U.; Tremel, K.; Sommer, M.; Crossland, E. J. W.; Ludwigs, S. Directed Crystallization of poly(3-Hexylthiophene) in Micrometre Channels under Confinement and in Electric Fields. *Nanoscale* **2012**, *4*, 2138–2144.

(61) Mandal, T.; Garg, A.; Deepak. Thin Film Transistors Fabricated by Evaporating Pentacene under Electric Field. *J. Appl. Phys.* **2013**, *114*, 154517.

(62) Matsukawa, T.; Kobayashi, S.; Onodera, T.; Oikawa, H.; Itaya, K. Electric-Field-Induced Orientation Control of Organic Semiconductor Rubrene Crystals. *Mater. Chem. Phys.* **2013**, *137*, 947–950.

(63) Komino, T.; Kuwabara, H.; Ikeda, M.; Yahiro, M.; Takimiya, K.; Adachi, C. Droplet Manipulation by an External Electric Field for Crystalline Film Growth. *Langmuir* **2013**, *29*, 9592–9597.

(64) Ichikawa, H.; Saiki, K.; Suzuki, T.; Hasegawa, T.; Shimada, T. Uniaxial Alignment of Alq_3 by Laser-Assisted Molecular Beam Epitaxy. *Jpn. J. Appl. Phys.* **2005**, *44*, L1469–L1471.

(65) Pithan, L.; Cocchi, C.; Zschiesche, H.; Weber, C.; Zykov, A.; Bommel, S.; Leake, S. J.; Schäfer, P.; Draxl, C.; Kowarik, S. Light Controls Polymorphism in Thin Films of Sexithiophene. *Cryst. Growth Des.* **2015**, *15*, 1319–1324.

(66) Diemer, P. J.; Lyle, C. R.; Mei, Y.; Sutton, C.; Payne, M. M.; Anthony, J. E.; Coropceanu, V.; Brédas, J. L.; Jurchescu, O. D. Vibration-Assisted

Crystallization Improves Organic/dielectric Interface in Organic Thin-Film Transistors. *Adv. Mater.* **2013**, *25*, 6956–6962.

(67) Pohl, H. A. *Dielectrophoresis: The Behavior of Neutral Matter in Nonuniform Electric Fields*; Cambridge; New York: Cambridge University Press, 1978.

(68) Jones, T. B. *Electromechanics of Particles*; Cambridge; New York: Cambridge University Press, 1995.

(69) Liu, Y.; Chung, J. H.; Liu, W. K.; Ruoff, R. S. Dielectrophoretic Assembly of Nanowires. *J. Phys. Chem. B* **2006**, *110*, 14098–14106.

(70) Freer, E. M.; Grachev, O.; Duan, X.; Martin, S.; Stumbo, D. P. High-Yield Self-Limiting Single-Nanowire Assembly with Dielectrophoresis. *Nat. Nanotechnol.* **2010**, *5*, 525–530.

(71) Yoshida, M.; Suemori, K.; Uemura, S.; Hoshino, S.; Takada, N.; Kodzasa, T.; Kamata, T. Development of Field-Effect Transistor-Type Photorewritable Memory Using Photochromic Interface Layer. *Jpn. J. Appl. Phys.* **2010**, *49*, 04DK09.

(72) Shen, Q.; Wang, L.; Liu, S.; Cao, Y.; Gan, L.; Guo, X.; Steigerwald, M. L.; Shuai, Z.; Liu, Z.; Nuckolls, C. Photoactive Gate Dielectrics. *Adv. Mater.* **2010**, *22*, 3282–3287.

(73) Crivillers, N.; Orgiu, E.; Reinders, F.; Mayor, M.; Samorì, P. Optical Modulation of the Charge Injection in an Organic Field-Effect Transistor Based on Photochromic Self-Assembled-Monolayer-Functionalized Electrodes. *Adv. Mater.* **2011**, *23*, 1447–1452.

(74) Zhang, H.; Guo, X.; Hui, J.; Hu, S.; Xu, W.; Zhu, D. Interface Engineering of Semiconductor/Dielectric Heterojunctions toward Functional Organic Thin-Film Transistors. *Nano Lett.* **2011**, *11*, 4939–4946.

(75) Li, Y.; Zhang, H.; Qi, C.; Guo, X. Light-Driven Photochromism-Induced Reversible Switching in P3HT–spiropyran Hybrid Transistors. *J. Mater. Chem.* **2012**, *22*, 4261.

(76) Kim, M.; Safron, N. S.; Huang, C.; Arnold, M. S.; Gopalan, P. Light-Driven Reversible Modulation of Doping in Graphene. *Nano Lett.* **2012**, *12*, 182–187.

(77) Hayakawa, R.; Higashiguchi, K.; Matsuda, K.; Chikyow, T.; Wakayama, Y. Optically and Electrically Driven Organic Thin Film Transistors with

Diarylethene Photochromic Channel Layers. *ACS Appl. Mater. Interfaces* **2013**, *5*, 3625–3630.

(78) Gemayel, M. El; Börjesson, K.; Herder, M.; Duong, D. T.; Hutchison, J. A.; Ruzié, C.; Schweicher, G.; Salleo, A.; Geerts, Y.; Hecht, S.; *et al.* Optically Switchable Transistors by Simple Incorporation of Photochromic Systems into Small-Molecule Semiconducting Matrices. *Nat. Commun.* **2015**, *6*, 6330.

(79) Suda, M.; Kato, R.; Yamamoto, H. M. Light-Induced Superconductivity Using a Photoactive Electric Double Layer. *Science (80-.).* **2015**, *347*, 743.

(80) Salleo, A.; Street, R. A. Light-Induced Bias Stress Reversal in Polyfluorene Thin-Film Transistors. *J. Appl. Phys.* **2003**, *94*, 471.

(81) Hamilton, M. C.; Martin, S.; Kanicki, J. Thin-Film Organic Polymer Phototransistors. *IEEE Trans. Electron Devices* **2004**, *51*, 877–885.

(82) Ogawa, S.; Naijo, T.; Kimura, Y.; Ishii, H.; Niwano, M. Photoinduced Doping Effect of Pentacene Field Effect Transistor in Oxygen Atmosphere Studied by Displacement Current Measurement. *Appl. Phys. Lett.* **2005**, *86*, 252104.

(83) Ogawa, S.; Nauo, T.; Ktmura, Y.; Ishii, H.; Niwano, M. Photoinduced Doping of Organic Field Effect Transistors Studied by Displacement Current Measurement and Infrared Absorption Spectroscopy in Multiple Internal Reflection Geometry. *Jpn. J. Appl. Phys.* **2006**, *45*, 530–533.

(84) Park, C. B.; Yokoyama, T.; Nishimura, T.; Kita, K.; Toriumi, A. Threshold-Voltage-Shift Mechanism in Pentacene Field Effect Transistors Caused by Photoirradiation. *Jpn. J. Appl. Phys.* **2008**, *47*, 3189–3192.

(85) Bum Park, C. Investigation of the Device Instability Feature Caused by Electron Trapping in Pentacene Field Effect Transistors. *Appl. Phys. Lett.* **2012**, *100*, 063306.

(86) Lin, Y.-J.; Huang, B.-C. Influence of Illumination on the Output Characteristics in Pentacene Thin Film Transistors. *Mater. Chem. Phys.* **2013**, *142*, 428.

(87) Yang, Y.; da Costa, R. C.; Fuchter, M. J.; Campbell, A. J. Circularly Polarized Light Detection by a Chiral Organic Semiconductor Transistor. *Nat. Photonics* **2013**, *7*, 634–638.

(88) Ding, Z.; Abbas, G.; Assender, H. E.; Morrison, J. J.; Yeates, S. G.; Patchett,

E. R.; Taylor, D. M. Effect of Oxygen, Moisture and Illumination on the Stability and Reliability of dinaphtho[2,3-b:2',3'-f]thieno[3,2-B]thiophene (DNTT) OTFTs during Operation and Storage. *ACS Appl. Mater. Interfaces* **2014**, *6*, 15224.

(89) Kitamura, M.; Arakawa, Y. Pentacene-Based Organic Field-Effect Transistors. *J. Phys. Condens. Matter* **2008**, *20*, 184011.

(90) Ebata, H.; Izawa, T.; Miyazaki, E.; Takimiya, K.; Ikeda, M.; Kuwabara, H.; Yui, T. Highly Soluble [1]benzothieno[3,2-B]benzothiophene (BTBT) Derivatives for High-Performance, Solution-Processed Organic Field-Effect Transistors. *J. Am. Chem. Soc.* **2007**, *129*, 15732–15733.

(91) Raychaudhuri, S.; Dayeh, S. A.; Wang, D.; Yu, E. T. Precise Semiconductor Nanowire Placement through Dielectrophoresis. *Nano Lett.* **2009**, *9*, 2260–2266.

(92) Shekhar, S.; Stokes, P.; Khondaker, S. I. Ultrahigh Density Alignment of Carbon Nanotube Arrays by Dielectrophoresis. *ACS Nano* **2011**, *5*, 1739–1746.

(93) Hirata, M.; Gotou, T.; Horiuchi, S.; Fujiwara, M.; Ohba, M. Thin-Film Particles of Graphite Oxide 1: High-Yield Synthesis and Flexibility of the Particles. *Carbon*, 2004, *42*, 2929–2937.

(94) Obata, S.; Tanaka, H.; Saiki, K. Electrical and Spectroscopic Investigations on the Reduction Mechanism of Graphene Oxide. *Carbon N. Y.* **2013**, *55*, 126–132.

(95) Campbell, R. B.; Robertson, J. M.; Trotter, J. The Crystal and Molecular Structure of Pentacene. *Acta Crystallogr.* **1961**, *14*, 705–711.

(96) Minakata, T.; Natsume, Y. Direct Formation of Pentacene Thin Films by Solution Process. *Synth. Met.* **2005**, *153*, 1–4.

(97) Natsume, Y.; Minakata, T.; Aoyagi, T. Pentacene Thin Film Transistors Fabricated by Solution Process with Directional Crystal Growth. *Org. Electron.* **2009**, *10*, 107–114.

(98) Siegrist, T.; Besnard, C.; Haas, S.; Schiltz, M.; Pattison, P.; Chernyshov, D.; Batlogg, B.; Kloc, C. A Polymorph Lost and Found: The High-Temperature Crystal Structure of Pentacene. *Adv. Mater.* **2007**, *19*, 2079–2082.

(99) Lindley, K. S.; Rowson, N. A. Charging Mechanisms for Particles Prior to Electrostatic Separation. *Magn. Electr. Sep.* **1997**, *8*, 101–113.

(100) Li, T.; Balk, J. W.; Ruden, P. P.; Campbell, I. H.; Smith, D. L. Channel Formation in Organic Field-Effect Transistors. *J. Appl. Phys.* **2002**, *91*, 4312–4318.

(101) R. S. Ruoff; Tse, D. S.; Malhotra, R.; Lorents, D. C. Solubility of C_{60} in a Variety of Solvents. *J. Phys. Chem.* **1993**, *97*, 3379–3383.

(102) Sai, N.; Tiago, M. L.; Chelikowsky, J. R.; Reboredo, F. A. Optical Spectra and Exchange-Correlation Effects in Molecular Crystals. *Phys. Rev. B* **2008**, *77*, 161306.

(103) *CRC Handbook of Chemistry and Physics*; 90th ed.; CRC Press: Boca Raton, FL, 2009.

(104) Lee, S.; Jo, G.; Kang, S.-J.; Wang, G.; Choe, M.; Park, W.; Kim, D.-Y.; Kahng, Y. H.; Lee, T. Enhanced Charge Injection in Pentacene Field-Effect Transistors with Graphene Electrodes. *Adv. Mater.* **2011**, *23*, 100–105.

(105) Soeda, J.; Okamoto, T.; Hamaguchi, A.; Ikeda, Y.; Sato, H.; Yamano, A.; Takeya, J. Two-Dimensional Crystal Growth of Thermally Converted Organic Semiconductors at the Surface of Ionic Liquid and High-Mobility Organic Field-Effect Transistors. *Org. Electron. physics, Mater. Appl.* **2013**, *14*, 1211–1217.

(106) Stehr, V.; Pfister, J.; Fink, R. F.; Engels, B.; Deibel, C. First-Principles Calculations of Anisotropic Charge-Carrier Mobilities in Organic Semiconductor Crystals. *Phys. Rev. B* **2011**, *83*, 155208.

(107) Takeyama, Y.; Ono, S.; Matsumoto, Y. Organic Single Crystal Transistor Characteristics of Single-Crystal Phase Pentacene Grown by Ionic Liquid-Assisted Vacuum Deposition. *Appl. Phys. Lett.* **2012**, *101*, 083303.

(108) Kimura, Y.; Niwano, M.; Ikuma, N.; Goushi, K.; Itaya, K. Organic Field Effect Transistor Using Pentacene Single Crystals Grown by a Liquid-Phase Crystallization Process. *Langmuir* **2009**, *25*, 4861–4863.

(109) Toffolo, F.; Brinkmann, M.; Greco, O.; Biscarini, F.; Taliani, C.; Gomes, H. L.; Aiello, I.; Ghedini, M. Influence of the Metal Center on the Morphology of Coordination Compounds Thin Films. *Synth. Met.* **1999**, *101*, 140–141.

(110) Mascaro, D.; Thompson, M.; Smith, H.; Bulovic, V. Forming Oriented Organic Crystals from Amorphous Thin Films on Patterned Substrates via Solvent-Vapor Annealing. *Org. Electron.* **2005**, *6*, 211–220.

(111) De Luca, G.; Liscio, A.; Nolde, F.; Scolaro, L. M.; Palermo, V.; Müllen, K.; Samorì, P. Self-Assembly of Discotic Molecules into Mesoscopic Crystals by Solvent-Vapour Annealing. *Soft Matter* **2008**, *4*, 2064.

(112) Treossi, E.; Liscio, A.; Feng, X.; Palermo, V.; Müllen, K.; Samorì, P. Temperature-Enhanced Solvent Vapor Annealing of a C_3 Symmetric Hexa-Peri-Hexabenzocoronene: Controlling the Self-Assembly from Nano- to Macroscale. *Small* **2009**, *5*, 112–119.

(113) Tisserant, J.; Wicht, G.; Göbel, O. F.; Bocek, E.; Bona, G.; Geiger, T.; Hany, R.; Mezzenga, R.; Partel, S.; Schmid, P.; *et al.* Growth and Alignment of Thin Film Organic Single Crystals from Dewetting Patterns. *ACS Nano* **2013**, *7*, 5506–5513.

(114) Liu, C.; Minari, T.; Lu, X.; Kumatani, A.; Takimiya, K.; Tsukagoshi, K. Solution-Processable Organic Single Crystals with Bandlike Transport in Field-Effect Transistors. *Adv. Mater.* **2011**, *23*, 523–526.

(115) Liu, C.; Minari, T.; Li, Y.; Kumatani, A.; Lee, M. V.; Athena Pan, S. H.; Takimiya, K.; Tsukagoshi, K. Direct Formation of Organic Semiconducting Single Crystals by Solvent Vapor Annealing on a Polymer Base Film. *J. Mater. Chem.* **2012**, *22*, 8462.

(116) Yang, Y.; Liu, C.; Gao, S.; Li, Y.; Wang, X.; Wang, Y.; Minari, T.; Xu, Y.; Wang, P.; Zhao, Y.; *et al.* Large [6,6]-Phenyl C_{61} Butyric Acid Methyl (PCBM) Hexagonal Crystals Grown by Solvent-Vapor Annealing. *Mater. Chem. Phys.* **2014**, *145*, 327–333.

(117) Liu, C.; Li, Y.; Minari, T.; Takimiya, K.; Tsukagoshi, K. Forming Semiconductor/dielectric Double Layers by One-Step Spin-Coating for Enhancing the Performance of Organic Field-Effect Transistors. *Org. Electron.* **2012**, *13*, 1146–1151.

(118) Huang, T.; Su, Y.; Wang, P. Poly(methyl Methacrylate) Dielectric Material Applied in Organic Thin Film Transistors. *Jpn. J. Appl. Phys.* **2008**, *47*, 3185–3188.

(119) Hebard, A. F.; Haddon, R. C.; Fleming, R. M.; Kortan, A. R. Deposition and Characterization of Fullerene Films. *Appl. Phys. Lett.* **1991**, *59*, 2109–2111.

(120) Kaneko, Y.; Onodera, T.; Kasai, H.; Okada, S.; Oikawa, H.; Nakanishi, H.; Fukuda, T.; Matsuda, H. Reversible and Efficient Anisotropic Orientation of Dispersed Aromatic Hydrocarbon Nanocrystals in a Magnetic Field. *J. Mater. Chem.* **2005**, *15*, 253.

(121) Balzer, F.; Rubahn, H. G. Laser-Controlled Growth of Needle-Shaped Organic Nanoaggregates. *Nano Lett.* **2002**, *2*, 747–750.

(122) Yamamoto, Y.; Ichikawa, H.; Ueno, K.; Koma, A.; Saiki, K.; Shimada, T. Morphological Change of C_{60} Monolayer Epitaxial Films under Photoexcitation. *Phys. Rev. B* **2004**, *70*, 155415.

(123) Sander, A.; Hammer, R.; Duncker, K.; Förster, S.; Widdra, W. Thermally and Photoinduced Polymerization of Ultrathin Sexithiophene Films. *J. Chem. Phys.* **2014**, *141*, 104704.

(124) Uchida, E.; Azumi, R.; Norikane, Y. Light-Induced Crawling of Crystals on a Glass Surface. *Nat. Commun.* **2015**, *6*, 7310.

(125) Wakayama, Y.; Hayakawa, R.; Seo, H.-S. Recent Progress in Photoactive Organic Field-Effect Transistors. *Sci. Technol. Adv. Mater.* **2014**, *15*, 24202.

(126) Hoshino, T.; Ito, H.; Fujieda, I.; Hanasaki, T. Lateral Solidification of a Liquid Crystalline Semiconductor Film Induced by Temperature Gradient. *Proc. SPIE* **2013**, *8831*, 883115.

(127) Fujieda, I.; Iizuka, N.; Onishi, Y. Directional Solidification of C_8-BTBT Films Induced by Temperature Gradients and Its Application for Transistors. *Proc. SPIE* **2015**, *9360*, 936012.

(128) Hamadani, B. H.; Natelson, D. Nonlinear Charge Injection in Organic Field-Effect Transistors. *J. Appl. Phys.* **2005**, *97*, 64508.

(129) Izawa, T.; Miyazaki, E.; Takimiya, K. Molecular Ordering of High-Performance Soluble Molecular Semiconductors and Re-Evaluation of Their Field-Effect Transistor Characteristics. *Adv. Mater.* **2008**, *20*, 3388–3392.

(130) Li, Y.; Liu, C.; Lee, M. V.; Xu, Y.; Wang, X.; Shi, Y.; Tsukagoshi, K. In Situ Purification to Eliminate the Influence of Impurities in Solution-Processed Organic Crystals for Transistor Arrays. *J. Mater. Chem. C* **2013**, *1*, 1352.

(131) Hosoi, Y.; Deyra, D. M.; Nakajima, K.; Furukawa, Y. Micro-Raman Spectroscopy on Pentacene Thin-Film Transistors. *Mol. Cryst. Liq. Cryst.* **2008**, *491*, 317–323.

(132) Seto, K.; Furukawa, Y. Study on Solid Structure of Pentacene Thin Films Using Raman Imaging. *J. Raman Spectrosc.* **2012**, *43*, 2015–2019.

(133) Mino, T.; Saito, Y.; Yoshida, H.; Kawata, S.; Verma, P. Molecular Orientation Analysis of Organic Thin Films by *z*-Polarization Raman Microscope. *J. Raman Spectrosc.* **2012**, *43*, 2029–2034.

Acknowledgements

I would like to thank to all those who gave me support for this dissertation.

First of all, I would like to express my sincere gratitude to Prof. Saiki, who instructed the whole of my research. His encouragement for six years enabled me to study molecular electronics further and further.

I am also indebted to Prof. Sasaki for good comments and suggestions in the weekly seminar.

I have had the sincere support and encouragement of Dr. Obata on my research and laboratory life.

For the experimental measurement in this dissertation, I thank to the following:

Prof. Terashima and Dr. Sven in the Univ. of Tokyo for XRD measurement.

Prof. Ikeda and Mr. Saito in Tohoku Univ. for XRD measurements.

Prof. Ueno and Mr. Kawai in Saitama Univ. for Kelvin-probe force microscopy.

For the supply of materials in this dissertation, I thank to the following:

Nippon Graphite Industries and SEC Carbon for graphite powder.

Nippon Kayaku Co. for C8-BTBT powder.

I owe an important debt to the present/former members in Saiki laboratory. Especially, I would like to express my gratitude to the following members:

Ms. Orihara, who is a secretary of the laboratory and kindly supported my laboratory life.

Dr. Imamura, Dr. Tanaka and Dr. Terasawa, who are graduates of the laboratory and gave me a lot of comments and suggestions on my research.

Mr. Akada and Mr. Katoh, who belong in the doctoral course with me and supported my laboratory life.

Finally, I would like to express my sincere gratitude to my family.